FIRST-PRINCIPLES STUDY OF DISLOCATIONS IN $Cu(In,Ga)Se_2$ SOLAR CELL ABSORBERS

DANIEL ANTONIO BARRAGAN-YANI

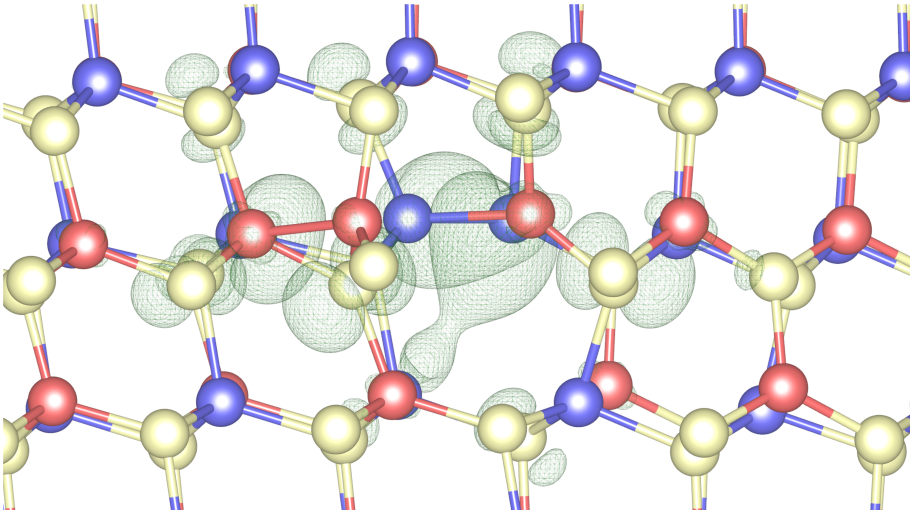

Dissertation

2018

FIRST-PRINCIPLES STUDY OF DISLOCATIONS IN $Cu(In,Ga)Se_2$ SOLAR CELL ABSORBERS

Zur Erlangung des akademisches Grades eines Doktors der Naturwissenschaften (Dr. rer. nat.) genehmigte Dissertation von M.Sc. Daniel Antonio Barragan-Yani geboren in Barranquilla, Kolumbien

Fachgebiet Materialmodellierung
Fachbereich Material- und Geowissenschaften
Technische Universität Darmstadt

Referent: Prof. Dr. Karsten Albe
Korreferent: Apl. Prof. Dr. Andreas Klein
1. Prüfer: Prof. Dr. Roland Scheer
2. Prüfer: Prof. Dr. Ralph Krupke

Tag der Einreichung: 04. June 2018
Tag der Prüfung: 03. September 2018

Darmstadt 2018
D17

On the cover: Charge density isosurface of a defect state induced by homopolar bonds in the core of a dislocation in $CuInSe_2$. The isosurfaces are displayed using VESTA and at 10% of their maximum value.

Please cite this document as:
URN: urn:nbn:de:tuda-tuprints-81954
URL: http://tuprints.ulb.tu-darmstadt.de/8195/

Dieses Dokument wird bereitgestellt von tuprints,
E-Publishing-Service der TU Darmstadt
http://tuprints.ulb.tu-darmstadt.de
tuprints@ulb.tu-darmstadt.de

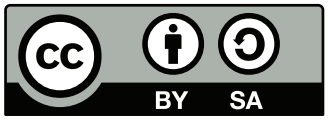

CONTENTS

LIST OF FIGURES

LIST OF TABLES

ABBREVIATIONS AND SYMBOLS

Abreviations

AOT	Atomic orbital theory
APT	Atom probe tomography
CB	Conduction band
CBM	Conduction band minimum
CFEG	Cold field emission gun
DBS_a	Danglind bond state (acceptor)
DBS_d	Danglind bond state (donor)
DFT	Density functional theory
DLTS	Deep-level transient spectroscopy
DOS	Density of states
EDT	Elastic dipole tensor
EELS	Electron energy-loss spectroscopy
FF	Fill factor of a solar cell
FIB	Focused ion beam
FNV	Freysoldt-Neugebauer-Van de Walle correction scheme
GGA	Generalized gradient approximation
GGA+U	GGA plus orbital-dependent on-site repulsion interaction
GPA	Geometrical phase analysis
HAADF	High-angle annular dark field
HF	Hartree-Fock method
HR-STEM	High resolution - scanning transmission electron microscopy
HSE06	Heyd-Scuseria-Ernzerhof screened-exchange hybrid functional
LDA	Local density approximation
LDA+U	LDA plus orbital-dependent on-site repulsion interactio
LDOS	Local density of states
LZ	Lany-Zunger correction scheme
MP	Makov-Payne correction scheme
OVITO	Open visualization tool
PAW	Projector augmented wave method
PBE	GGA parameterization of Perdew, Burke and Ernzerhof
PDs	Planar defects
PPs	Pseudopotentials
RGB	Red-green-blue
SRH	Shockley-Read-Hall recombination process
TEM	Transmission electron microscopy
VASP	Vienna ab-initio simulation package

VB	Valence band
VBM	Valence band maximum
VESTA	Visualization of electronic and structural analysis
WBS	Wrong bond state

Nomenclature for defects

α-core	Cation-rich core of a perfect 60°-mixed dislocation
β-core	Anion-rich core of a perfect 60°-mixed dislocation
Cu_i	Interstitial defects: Copper interstitial
In_{Cu}	Antisite defects: Indium atom on a copper site
V_{Cu}	Vacancies: Copper vacancy

Physical constants

$\hbar$	Reduced Planck constant
e	Elementary electric charge
h	Planck constant
k_B	Boltzmann constant
m_e	Electron rest mass

Symbols

$\boldsymbol{\sigma}$	Stress tensor
ΔE	Change in energy as a point defect segregates into the cores
$\Delta V[D^q]$	Potential alignment
$\epsilon(q/q')$	Charge transition level
$\eta(V)$	Efficiency of the solar cell
$\mu_i(P,T)$	Chemical potential of species i
Ω	Volume of the unit cell, volume of the supercell
ω	Phonon frequency
ω_{scr}	Screening factor in hybrid functionals
$\phi(\mathbf{r})$	Single-particle orbitals
$\phi_{KS}(\mathbf{r})$	Kohn-Sham orbitals
$\Psi(\mathbf{r},t)$	Many-electron wave function
$\Psi[n(\mathbf{r})]$	Electronic wave function as functional of the electronic density
Ψ_0	Ground-state wave function
Ψ_{KS}	Electronic wave function in the Kohn-Sham system
$\sigma_{\eta\zeta}$	Stress tensor components
$\mathbf{A}$	Area vector
$\mathbf{B}$	Lattice vector in reciprocal space
$\mathbf{b}$	Burgers vector
$\mathbf{F}$	Force
$\mathbf{G}[D^q]$	Elastic dipole tensor of defect D in charge state q
$\mathbf{k}$	Vector in the first Brillouin zone
$\mathbf{l}$	Dislocation line direction
$\mathbf{r}$	Spatial coordinate
$\mathbf{u}$	Strain tensor
$\mathbf{u}^{el}$	Elastic strain

$\mathbf{u}^p$	Plastic strain
ε	Macroscopic dielectric constant
ε_i	Energy of Kohn-Sham orbital i
a, c	Lattice constants of the chalcopyrite structure
B	Bulk modulus
b	Interatomic bond
$C_{\eta\zeta\iota\chi}$	Components of the elastic stiffness tensor
D^q	Defect D in charge state q
E	Energy
$E(n_\mathrm{D}, \mathbf{u})$	Supercell energy in terms of strain and number of defects
$E[n(\mathbf{r})]$	Energy as functional of the electronic density
$E^\mathrm{tot}_\mathrm{corr}$	Correction of finite-size effects
$E^f[D^q]$	Formation energy of defect D in charge state q
$E^f_\mathrm{dip}[D^q]$	Formation energy of a dislocation dipole D in charge state q
E^q_corr	Correction for interaction with periodic images
E_0	Ground-state energy
E_F	Fermi level
E_G	Band-gap of the absorber
$E_\mathrm{RFE}[\mathrm{D}^q]$	Relative formation energy of defect D in charge state q
E_Total	Total energy of the system
$E_\mathrm{Tot}[\mathrm{bulk}]$	Total energy of non-defective supercell
$E_\mathrm{Tot}[D^q]$	Total energy of supercell containing defect D in charge state q
E_VBM	VBM energy
E_{far}	Supercell energy when a point defect is far from the cores
$E_{KS}[n(\mathbf{r})]$	Energy fo the Kohn-Sham system
E_{near}	Supercell energy when a point defect is near the cores
$E_{xc}[n(\mathbf{r})]$	Exchange-correlation energy
$G^f[D^q]$	Gibbs energy of formation of defect D in charge state q
H	Hamiltonian of a solid
$H^f[D^q]$	Enthalpy of formation of defect D in charge state q
H_{el}	Hamiltonian of the electronic system
H_{KS}	Hamiltonian of the Kohn-Sham auxiliary system
J_{sc}	Short-circuit current
L	Linear dimension of the supercell
N	Number of electrons
$n(\mathbf{r})$	Electronic density
$n_0(\mathbf{r})$	Ground-state electronic density
P	Pressure
q	Charge of the defect
S	Shear modulus
$S^f[D^q]$	Formation entropy of defect D in charge state q
T	Temperature of the solar cell, temperature of the solid

t	Time
U	Orbital-dependent on-site repulsion in LDA+U
u	Internal displacement in the chalcopyrite structure
$u_{\eta\zeta}$	Strain tensor components
V	Photogenerated voltage
$V^f[D^q]$	Formation volume of defect D in charge state q
V_{oc}	Open-circuit voltage
$V_{xc}[n(\mathbf{r})]$	Exchange-correlation potential

ABSTRACT

Among the thin-film solar cells, the maximum efficiencies are achieved by devices that use Cu(In,Ga)Se_2 as absorber [1]. However, this fact should not mask that there is room for improvement, if we could mitigate the main sources of efficiency loss in this solar cell type, which are induced by lattice defects [2]. Therefore, a more complete picture of the nature of defects in Cu(In,Ga)Se_2-based solar cells would help to improve the growth process in such way that detrimental defects are avoided and the efficiency increased. In order to achieve this goal, first-principles calculations provide valuable insights that complement experimental studies and can also be used as predictive tools. These calculations have been and continue to be succesfully used for the case of point and planar defects in Cu(In,Ga)Se_2-based solar cells [3–10].

However, a defect type that has been studied to a lesser extent are lattice dislocations. The aim of this thesis is to carry out a complete study of the structural and electronic properties of Frank partials and perfect dislocations in $CuInSe_2$ and $CuGaSe_2$. Results from this study allow us to solve, at least partially, the puzzle of Cu(In,Ga)Se_2-based solar cells which exhibit decent efficiencies and at the same time have a very high dislocation density [9, 11–13]. Specifically, in the case of Frank partials our results suggest that these cores prefer to be non-stoichiometric and, as a consequence, are expected to be highly detrimental. Therefore, this defect type should not be present in a fully grown and highly efficient device. Furthermore, we relate the beneficial effect of the Cu-rich stage of the three-stage co-evaporation process used to deposit the absorber in high-efficiency devices with the disappearance of these loops. In the case of stoichiometric perfect dislocations, our results show that their electrical activity is related to the presence of cation-cation or anion-anion "wrong" bonds in the cores. Moreover, we found that cation-rich α-cores are active in the Cu(In,Ga)Se_2 semiconductor alloy, whereas the anion-rich β-cores are not. These results, along with the study of sodium segregation tendency into the electrically active cores, are put in perspective with respect to the experimental findings and structural models available in literature.

ZUSAMMENFASSUNG

Bei Dünnschichtsolarzellen werden die maximalen Effizienzwerte von Geräten erreicht, die Cu(In,Ga)Se_2 als Absorber verwenden [1]. Diese Tatsache sollte jedoch nicht darüber hinwegtäuschen, dass es hier immer noch Verbesserungspotential gibt. Die Hauptquellen für Effizienzverluste in diesem Solarzellentyp werden durch Gitterdefekte erzeugt. Daher würde ein vollständigeres Verständnis dieser Defektart in Cu(In,Ga)Se_2-basierten Solarzellen helfen, den Wachstumsprozess so zu verbessern, dass schädliche Defekte vermieden und die Effizienz gesteigert wird. Um dieses Ziel zu erreichen, liefern First-Principles-Berechnungen wertvolle Erkenntnisse, die experimentelle Studien ergänzen und auch als prädiktive Werkzeuge genutzt werden können. Diese Berechnungen wurden und werden erfolgreich für den Fall von Punkt- und Planardefekten in Cu(In,Ga)Se_2-basierten Solarzellen durchgeführt [3–10].

Ein Defekttyp, der bis jetzt in geringerem Maße untersucht wurde, sind jedoch Gitterversetzungen. Das Ziel dieser Arbeit ist es, eine vollständige Studie über die strukturellen und elektronischen Eigenschaften von Frank Partialversetzungen und perfekten Versetzungen in $CuInSe_2$ und $CuGaSe_2$ durchzuführen. Die Ergebnisse dieser Studie erlauben es uns, zumindest teilweise, das Rätsel zu lösen, warum Cu(In,Ga)Se_2-basierten Solarzellen mit einer sehr hohen Versetungsdichte trotzdem einen guten Wirkungsgrad aufweisen können [9, 11–13]. Insbesondere im Falle von Frank Partialversetzungen deuten unsere Ergebnisse darauf hin, dass diese Kerne eine nicht-stöchiometrische Konfiguration bevorzugen und daher hochgradig schädlich sind. Deshalb sollte dieser Fehlertyp am Ende des Herstellungsprozesses nicht vorhanden sein um ein hocheffizienten Solarzelle zu erzeugen. Wir konnten den positiven Effekt der Cu-reichen Stufe des dreistufigen Co-Verdampfungsprozesses, mit dem der Absorber in hocheffizienten Geräten abgeschieden wird, mit dem Verschwinden dieser Partialversetzungen verknüpfen. Im Falle von stöchiometrischen perfekten Versetzungen zeigen unsere Resultate, dass deren elektrische Aktivität mit dem Vorhandensein von Kationen-Kationen oder Anionen-Anionen "falschen" Bindungen in den Kernen zusammenhängt. Außerdem haben wir herausgefunden, dass kationenreiche α-Kerne in Cu(In,Ga)Se_2 Halbleitern elektrisch aktiv sind, während die anionreichen β-Kerne es nicht sind. Diese Ergebnisse, zusammen mit unserer Untersuchung der Tendenz zur Natriumanreicherung in den elektrisch aktiven Kernen, werden in Bezug zu experimentellen Befunden und Strukturmodelle in der Literatur gesetzt.

MOTIVATION

Supported by the majority of countries, the Paris agreement targets to cut greenhouse gas emissions in a way that keep us from the 2°C temperature rise limit [14, 15]. In order to achieve this goal, our economy and energy production technologies must become low-carbon ones. Renewable energy sources are the natural answer to this challenge. However, they should not be used naively as pointed out by Axel Kleidon in his excellent treatise on the thermodynamics of the earth [16]. He remarks that although the raw energy delivered by the sun at the upper atmosphere of the earth is 10^4 times the global energy needs (approximately 17 TW), this ratio is very different when we analyze the energy component available to do useful work, refered to as *usable energy*. For example, when analyzing the raw energy consumption, the metabolism of all mankind is usually regarded as minimal. Nevertheless, when analyzed in terms of usable energies, human metabolism and oceanic circulation dissipate a comparable amount of energy [16]. This fact reveals the real size of the global energy needs, which are 10-100 times larger than our metabolic needs. As Kleidon points out, if we were to obtain such huge amount of energy from wind turbines, we would take away more or less half the of the energy available in winds [16]. Such hypothetical situation would imply a danger analogous to the one created by our careless use of fossil fuels.

Having this in mind and based on the thermodynamic limits of the different renewable energy sources available, it has been concluded that direct conversion of solar radiation is by far the greatest and most secure alternative to achieve a low-carbon economy [16–18]. Such direct conversion can be achieved by means of solar cells, which in the case of single junction devices can reach a theoretical maximum efficiency of around 33%, as predicted by Shockley and Queisser based on a detailed balance analysis [19]. Nevertheless, due to imperfections in their constitutive materials and flaws in their design, efficiencies of real solar cells are always below this value. Furthermore, despite the progress that has been made in the development of these devices, transferring record efficiencies achieved in laboratories into mass production at a cost competitive to fossil fuels remains a challenge.

One approach to reduce the production cost of solar cell production is to use thin-films, which imply a large reduction in the amount of material and energy needed for device fabrication [20, 21]. In this thesis, we focus on the specific case of thin-film solar cells with $Cu(In,Ga)Se_2$ as absorber layer, which currently exhibit a maximum efficiency of 22.6% [1]. This value is still far from the Shockley-Queisser limit but represents the highest among thin-film solar cells [22]. When

compared with other semiconductor materials used as absorbers in solar cells, $Cu(In,Ga)Se_2$ stands out due to its great tolerance to variations in stoichiometry [20], very high optical absorption coefficient [23] and due to the fact that the polycrystalline $Cu(In,Ga)Se_2$ tends to outperform its single crystalline counterpart [24]. Nevertheless, despite all these remarkable traits, there is room for performance improvement. Any futher increment in the efficiency of $Cu(In,Ga)Se_2$ based solar cells would lower its cost and consequently help to establish photovoltaics as a real challenger to fossil fuels.

The main sources of efficiency loss in this solar cell type are non-radiative recombination and fluctuations in the electrostatic potential, both induced by the presence of defects like point defects, dislocations and grain boundaries in the absorber layer [2, 9, 10]. Therefore, avoiding detrimental defects when fabricating the device should improve the maximum efficiency possible. However, whether a specific defect is harmful or not (there can even be beneficial ones) in a given material cannot be known a priori. Naturally, experiments can shed light on the subject, but defect identification and characterization is usually difficult and frequently complex setups are needed. For $Cu(In,Ga)Se_2$ based absorbers these drawbacks in the experimental studies of defects are enhanced due to the intrinsic complexity of a quaternary semiconductor. However, during the last decades first-principles calculations have reached the power and accuracy needed to complement experimental studies and are now reliable enough to be used as predictive tools [25–27]. In the case of $Cu(In,Ga)Se_2$, both experiments and simulations have been extensively used to reveal the properties of point defects and grain boundaries present in this material (a more detailed description of the knowledge gain with respect with these two defect types will be presented in section 1.3 of this thesis). However, despite their intriguing properties, very little is known about dislocations in $Cu(In,Ga)Se_2$. In contrast to what has been reported for other semiconductor materials, such as GaN, dislocations in $Cu(In,Ga)Se_2$ appear to be harmless. Transmission electron microscopy experiments have shown significant dislocation densities up to 10^{11} cm^{-2} in $Cu(In,Ga)Se_2$ based devices, which at the same time show power-conversion efficiencies of more than 15% [13, 28]. This experimental result suggests that lattice dislocations in CIGSe-based absorbers are intrinsically inactive or passivated by the segregation of point defects. It is the aim of the present thesis to reveal the physical origin of these observations by means of first-principles calculations of the structural and electronic properties of dislocations in $Cu(In,Ga)Se_2$ and to fill a gap in our current understanding of the physical properties of defects in $Cu(In,Ga)Se_2$ absorbers. Since, as mentioned before, defect related issues represent the biggest efficiency loss in $Cu(In,Ga)Se_2$ based devices, we hope that a more complete picture of their nature will help to improve the growth process in such way that detrimental defects are avoided and the efficiency is increased.

Part I

INTRODUCTION

The following part introduces the basics of Cu(In,Ga)Se_2 solar cells. It includes a brief review of the role of point and planar defects in this material and finishes with a detailed and up-to-date account of the available knowledge on the topic of this thesis, the characteristics of lattice dislocations in Cu(In,Ga)Se_2.

1

$Cu(In,Ga)Se_2$ BASED THIN-FILM SOLAR CELLS

1.1 INTRODUCTION

Semiconductor solar cells are solid-state devices with the ability to transform light into electricity by means of a quantum process, namely the photovoltaic effect [17, 18, 29, 30]. In this chapter, we present a brief introduction to the structure, properties and limitations of one of the most succesful types of photovoltaic devices available today: $Cu(In,Ga)Se_2$ thin-film solar cells. We start by discussing the stacking sequence and growth method of such highly efficient devices, followed by a section focused on the properties of point defects and planar defects in this material. Finally, we present a review of the current understanding of dislocations in the chalcopyrite structure of $Cu(In,Ga)Se_2$ and its parent compounds. At the end of the chapter, the open questions addressed by this thesis are presented.

By no means this short chapter attempts to be a comprehensive treatise on a complex topic like the physics of $Cu(In,Ga)Se_2$ based solar cells. For detailed discussions on the matter we recommend the books by Scheer and Schock [23] and by Kodigala [24]. A complete overview of the development status of the currently available commercial technologies and a short discussion on third-generation concepts can be found in the book edited by Conibeer and Willoughby [31].

Readers unfamiliar with the basic theory of solar cells and dislocations are referred to Appendix A and B, respectively. In the former, we present a brief introduction to the working principle of semiconductor solar cells along with the physical origin of their efficiency limits. In the latter, we review the concept of crystal dislocations in materials, with special attention to the case of semiconductors, and we introduce the different types of dislocations.

1.2 BASICS AND LIMITATIONS OF $Cu(In,Ga)Se_2$ BASED THIN-FILM SOLAR CELLS

Thin-film solar cells with Cu-based absorber materials have been investigated since the 1950s. Back then Cu_2S and not $CuInSe_2$ or $Cu(In,Ga)Se_2$ was used as absorber [32, 33]. In the beginning of the 1970s, S. Wagner and collegues used

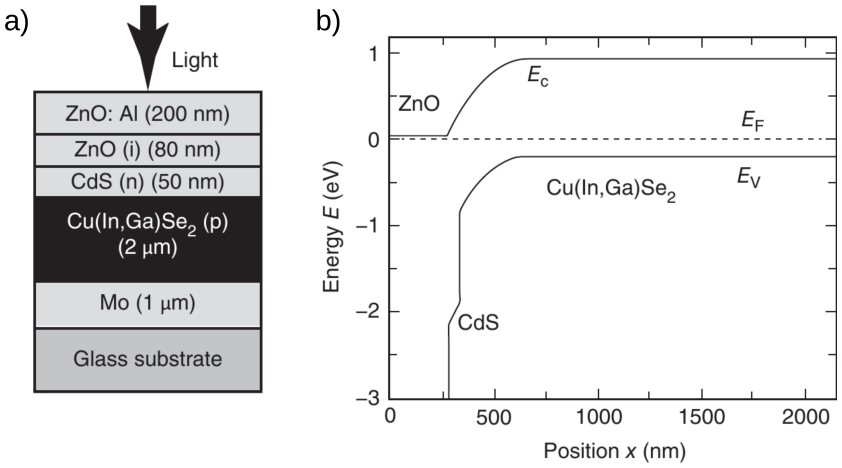

Figure 1.: Typical structure of a Cu(In,Ga)Se_2 based thin-film solar cell (a) and band diagram of such a device (b) (From Ref. [38], *©WILEY-VCH Verlag GmbH & Co. KGaA*)

p-type $CuInSe_2$ in a photodetector for GaAs lasers [34, 35]. Only after measuring the quantum efficiency spectrum of such device they realized that it could be used as a solar cell [36]. After a deeper characterization of the new cell and a few experiments where its voltage-current behavior was improved, conversion efficiencies of 12% were reported [37]. Based on the large tolerance to variations in stoichiometry [20] and the very high optical absorption coefficient [23] of $CuInSe_2$, it was clear that there was room for improvement. Furthermore, when Ga atoms are included such that the ratio of [Ga]/([Ga]+[In]) is around 0.2, the Cu(In,Ga)Se_2 alloy has a bandgap of 1.15eV which is very close to the optimum value (see Appendix A). These features, along with improvements in the design of the device, have allowed thin-film solar cells with Cu(In,Ga)Se_2 as absorber to reach laboratory efficiencies of 22.6% [1].

1.2.1 *Structure and band diagram of the heterojunction*

The typical structure of a Cu(In,Ga)Se_2 based thin-film solar cell is shown in Figure 1a. A soda-lime glass is used as substrate and the stacking sequence starts with a Mo layer which serves as back contact. Within this configuration, as deposition happens, sodium diffuses from the glass through the Mo layer into the growing absorber material. The presence of sodium in the absorber resulting from this process plays a primary role in the device quality, i.e. its incorporation is associated to a higher conductivity [4, 23, 39, 40]. Nevertheless, the origin of these beneficial effects is still under debate. A short survey on the most accepted explanations can be found in Chapter 6. The next layer is the Cu-poor grown Cu(In,Ga)Se_2 absorber, which is a p-type semiconductor [21, 23, 41]. Ex-

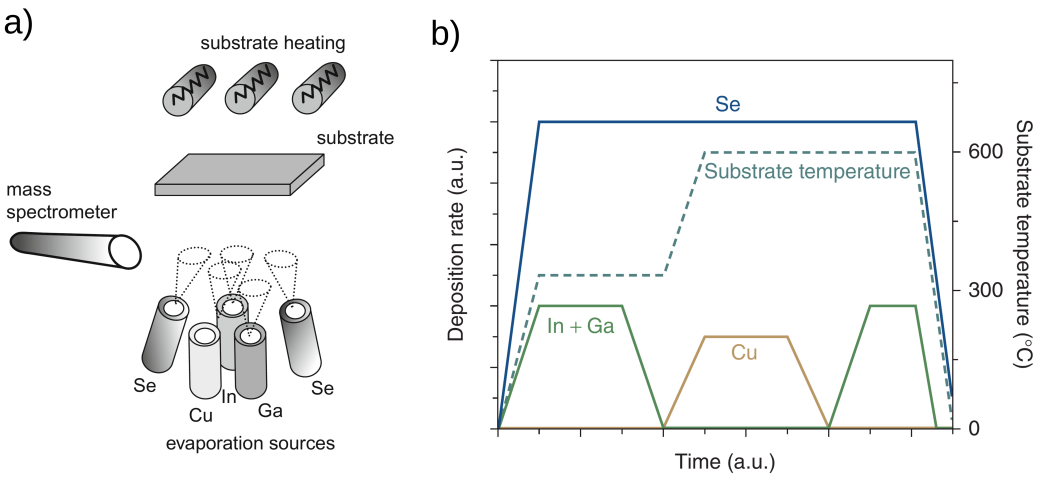

Figure 2.: Depiction of the deposition of the Cu(In,Ga)Se$_2$ absorbers by co-evaporation on a heated substrate (a) and detailed deposition rates and substrates temperatures used in the three-stage process (b). (Figure on the left was adapted from Ref. [21], ©2011 with permission from Elsevier, and the one in the right from Ref. [31], ©*2014 John Wiley & Sons, Ltd*)

periments have shown that a thin MoSe$_2$ layer is formed at the Mo/Cu(In,Ga)Se$_2$ interface [23, 42]. Such thin layer has been proposed as explanation of why the contact across the Mo/Cu(In,Ga)Se$_2$ is quasi-ohmic [43]. After the absorber, an n-type CdS buffer layer is deposited by means of a chemical bath, followed by a nominally intrinsic i-ZnO layer and a heavily doped ZnO:Al window layer. The last two layers are sputtered on top of the CdS buffer. As we can see from this stacking sequence, p-type and n-type layers in Cu(In,Ga)Se$_2$ based thin-film solar cell are not based on the same material, hence the name *heterojunction*.

In Figure 1b we show the band diagram of this device. The most relevant detail we can grasp from such diagram is the existence of band offsets and discontinuities at the different interfaces present in the device. Futhermore, from this diagram we can also get some insight on the not yet fully understood role of the CdS buffer layer and the relevance of the i-ZnO. Being only 50 nm thick, the buffer layer cannot complete the heterojunction by itself. However, the alignment of the conduction band (CB) in both the CdS/Cu(In,Ga)Se$_2$ and i-ZnO/CdS interfaces is almost flat [44, 45]. This behavior guarantees barrier-free electron transport and that interface recombination is not enhanced.

1.2.2 *Deposition method for the absorber*

Devices with highest efficiencies use Cu(In,Ga)Se$_2$ absorbers with a Ga/(Ga+In) ratio between 20-30% prepared by a state-of-the-art three-stage co-evaporation

process [21, 23]. This deposition technique was introduced in 1994 [46] and it is based on the previously used "Boeing" two-stage process [47]. In Figure 3(a) we can see a simplified depiction of the co-evaporation process used to grow the Cu(In,Ga)Se_2 absorbers. As shown there, Cu, In, Ga and Se are evaporated from elemental sources into a high-vacuum chamber where they are deposited onto a heated substrate. Specifically, the three-stage co-evaporation process starts with the deposition of In, Ga and Se at relative low temperature of about 300°C. Then, the substrate temperature is increased and Cu is evaporated together with Se until a Cu-rich compound is reached. This second stage is needed to achieve good crystallization with resulting larger and less defective grains [21, 31, 48–50]. Such beneficial effect has been associated to the presence of a Cu_xSe phase, which forms a quasi-liquid surface layer that enhances mass transport and thus grain growth as it induces a liquid-solid growth mechanism [23]. In the third and final stage of the process, In, Ga and Se are deposited to ensure an overall In-rich composition. Such evaporation sequence combines large grains associated to the Cu-rich stage with the advantageous electronic properties of the In-rich (Cu-poor) structure [21, 31].

One drawback of this method is that the evaporation rates from each source are difficult to control and reproducibility issues are to be expected [21, 51]. At the industrial scale, an in-line process like the one depicted in Figure 3 is preferred [21, 51]. As we can see there, the substrate is exposed to elemental fluxes of various compositions while it moves. The process is designed such that the absorber is Cu-rich in the first part and Cu-poor at the end.

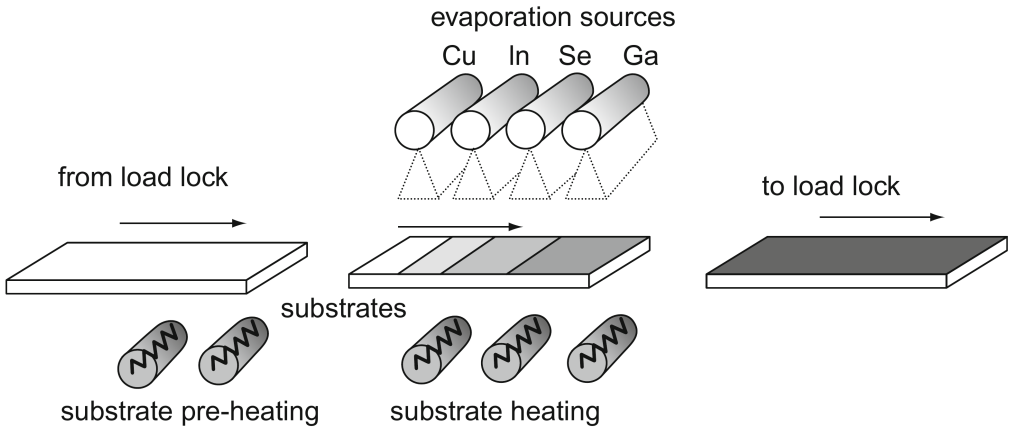

Figure 3.: Illustration of the in-line deposition process for co-evaporated Cu(In,Ga)Se_2 absorbers from line sources. (From Ref. [21], ©2011 with permission from Elsevier)

1.2.3 *Origin of dislocations in Cu(In,Ga)Se_2*

As we will see in the next section, defect related issues represent a large portion of the efficiency losses in Cu(In,Ga)Se_2-based thin-film solar cell. Naturally, the presence of defects in the absorber is associated to the history of a given sample and, as a consequence, its growth process. For example, the thermal equilibrium concentration of point defects can be determined by their formation energies, which depend on the availability of the atomic species during the growth process [27]. In the case of dislocations, which are the subject of this thesis, such approach is not valid since their formation energy diverges at zero stress, i.e. they are nucleated at finite mechanical load [52]. Due to the diamond-type structure of the Cu(In,Ga)Se_2 absorber, dislocation nucleation in this material should occur in an analogous process as it occurs in Si and Ge, where dislocations are known to be nucleated due to agglomeration of point defects, forming dislocation loops, and thermal stresses [53, 54]. The latter is usually cited as the main reason why dislocations occur. It certainly drives the multiplication of dislocations but does not explain the nucleation of the first existing dislocations from which other multiply [52, 53]. Based on atomistic simulations, it has been proposed that dislocations in silicon could nucleate from surface steps or corners in samples under stress [55–59], due to the far-field stress concentration and the weakening of the image effect at such locations [58]. In the specific case of Cu(In,Ga)Se_2 absorbers, Dietrich *et al.* [11, 12] found that the observed gallium gradients [21, 23, 48, 60] are strongly correlated with dislocation densities in the absorber. Furthermore, they found that a gallium gradient exists within the grain which result in intra-grain stresses. Therefore, analogously to the case of silicon, steps or corners on the grain boundaries of polycrystalline Cu(In,Ga)Se_2 under this intra-grain stress could be the nucleation centers for the perfect dislocations described in Section 1.3.2. On the other hand, the dislocation loops observed in experiments and described in Section 1.3.2, are likely to be originated by agglomeration of point defects or by growth accidents due to the low stacking fault energy in Cu(In,Ga)Se_2 [61].

1.2.4 *Efficiency loss sources*

Before considering the different loss mechanisms present in a Cu(In,Ga)Se_2-based thin-film solar cell, it is useful to introduce a pair of measures of quality of solar cells. We start with the fill factor FF which is given by

$$FF = \frac{V_m J_m}{V_{oc} J_{sc}}, \tag{1.1}$$

where V_m and J_m are the voltage and current for which the solar cell reaches its maximum power, respectively, and V_{oc} and J_{sc} are the open-circuit voltage and

short-circuit currents of the same solar cell. The second measure is the efficiency of the device, $\eta(V)$, which is a function of the photogenerated voltage at the terminals of the solar cell, V, and is defined as

$$\eta(V) = \frac{V_{oc} J_{sc} FF}{P_{in}}, \tag{1.2}$$

where P_{in} is the input power defined in Equation A.5. It is clear that the sub-optimal performance of a given solar cell is related to V_{oc}, J_{sc} and FF being lower than their corresponding maximum values predicted by the Shockley-Queisser limit. Actually, loss mechanisms can be classified depending on which of these values they affect the most. With this in mind, let us now focus on the specific case of Cu(In,Ga)Se_2 as discussed by Siebentritt [2], where the following loss mechanisms are relevant:

1. **Optical and collection losses** affect the photocurrent as defined in Equation A.1 due to a reduction in the quantum efficiency of the device. As a consequence, J_{sc} is also reduced. Both V_{oc} and FF are basically unaffected. A detailed account of all the optical and collection losses is shown in Figure 4. The photons reflected by the metallic grid used for collection at the front of the cell represent a loss between 2% to 4%, the latter being the typical value [2]. A larger loss comes from the reflection on the surface of the ZnO window layer, which amounts to 9% of the incident light. Fortunately, a MgF_2 antireflex coating can be used to avoid such issue [23]. In addition to reflection, photons are also absorbed in the ZnO layer, typically representing an extra 4% loss. Partial solution to this problem can be achieved by decreasing the infrared free carrier absorption in this material [63]. Further absorption preventing photons from arriving to the absorber occurs in the CdS buffer layer. In this case, the loss amounts to 2% and in principle, can be tackled by means of buffer materials with larger bandgaps [64]. Nevertheless, it should be said that finding new buffer layers that maintain or improve the efficiencies achieved with CdS buffer is a quite difficult task [65]. Losses within the Cu(In,Ga)Se_2 layer itself amount to a 5% reduction in the conversion efficiency. Specifically, two mechanisms can be identified in this layer, namely the weak absorption of photons with energies near the band-gap energy, E_G, of Cu(In,Ga)Se_2 and failures in the collection of photogenerated carriers due to a collection length shorter than the absorber thickness [23]. The former can be solved by using a thicker absorber layer and the latter issue can be overcome by a lower doping (which would increase the width of the *space-charge* region) and by reducing the degree of doping compensation (which would decrease the scattering of carriers due to charged defects) [2]. Both measures proposed to improve collection losses require a deep understanding of the properties of defects in Cu(In,Ga)Se_2. According to Siebentritt [2], if losses were only optical or

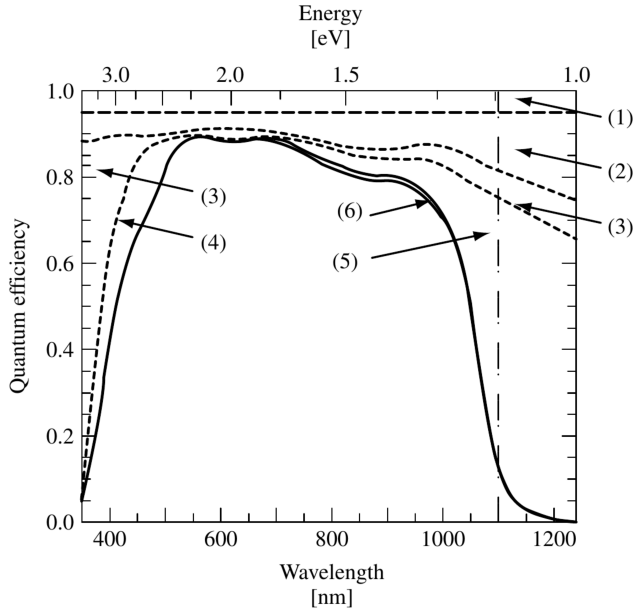

Region	Optical loss mechanism	ΔJ [mA/cm^2]
(1)	Shading from grid with 4% area coverage	1.7
(2)	Reflection from Cu(InGa)Se_2/CdS/ZnO	3.8
(3)	Absorption in ZnO	1.8
(4)	Absorption in CdS	0.8
(5)	Incomplete generation in Cu(InGa)Se_2	1.9
(6)	Incomplete collection in Cu(InGa)Se_2	0.4

Figure 4.: Quantum efficiency vs wavelength for a typical Cu(In,Ga)Se_2 solar cell. Areas or regions related to optical and collections losses in these devices are pointed out by numbers. In the table below it is possible to see a description of each of these regions. (From Ref. [62], *©2011 John Wiley & Sons, Ltd*)

coming from collection issues, the efficiency of solar cells would be around 28%. Furthermore, she reports that around 1-2% efficiency gain could be achieved by using a better material for the window layer or by enhancing the collection length.

2. **Shockley-Queisser radiative-only recombination is not realistic** since in high-efficiency Cu(In,Ga)Se_2 devices experimental findings point out that the dominant recombination mechanism appears to be non-radiative and is located in the *space-charge* region [2, 66]. Specifically, in Cu(In,Ga)Se_2 with rather low net doping, between 10^{15} and 10^{16}cm^{-3}, the contribution of Auger recombination is negligible compared to the one from the Shockley-Read-Hall (SRH) recombination [38]. SRH recombination is stronger if the

defect level is close to the middle of the gap (*deep defect*). Due to this non-ideal behavior, both V_{oc} and FF are reduced compared to their Shockley-Queisser limit values.

3. **Bandgap variations due to compositional changes and electrostatic fluctuations** are the two types of inhomogeneities considered for a polycrystalline material. Both reduce mainly the V_{oc} of the solar cell. In the first case, bandgap variations are caused by local changes of the composition and they can create recombination paths for energies smaller than the average bandgap. In the case of state-of-the-art Cu(In,Ga)Se_2 absorbers, the demostrated composition-related bandgap variations are below 10 meV [67, 68]. Rau and Werner [69] proved that bandgap variations smaller than 25 meV do not affect the efficiency of the device. Therefore, the effect of bandgap variations caused by local changes of the composition is considered negligible in this thin-film technology. On the other hand, when fluctuations of the electrostatic potential are present, the bandgap is everywhere the same. However, these fluctuations change the position of the valence band maximum (VBM) and conduction band minimum (CBM) and as a consequence, smaller effective bandgaps would be induced. These fluctuations are caused by the presence of defects and, contrary to the case of bandgap variations due to compositional changes, their effect is not negligible. For example, in the case of grain boundaries electrostatic potential changes of about 100 meV have been reported (see Ref. [70] and references therein).

4. **Series and shunt resistances** mostly affect the FF. However, based on the values reported in literature, it can be concluded that their effect is negligible [71, 72].

As pointed out by Siebentritt [2], a 7% gain in efficiency could be achieved by improving V_{oc}. Therefore, lifting the losses associated with non-radiative recombination and with fluctuations of the electrostatic potential would represent an efficiency boost larger than the one attainable by dealing with the optical and collection losses. Since both mechanisms affecting the V_{oc} in Cu(In,Ga)Se_2 based thin-film solar cells are caused by the presence of defects, their study is essential in order to achive higher efficiencies and, consequently, make these solar cells more competitive.

1.3 DEFECT RELATED EFFICIENCY LOSSES IN CU(IN,GA)SE_2 BASED SOLAR CELLS

Based on the previous discussion, it is clear that defect-related V_{oc} reduction is the largest source of efficiency losses in Cu(In,Ga)Se_2 based thin-film solar cells.

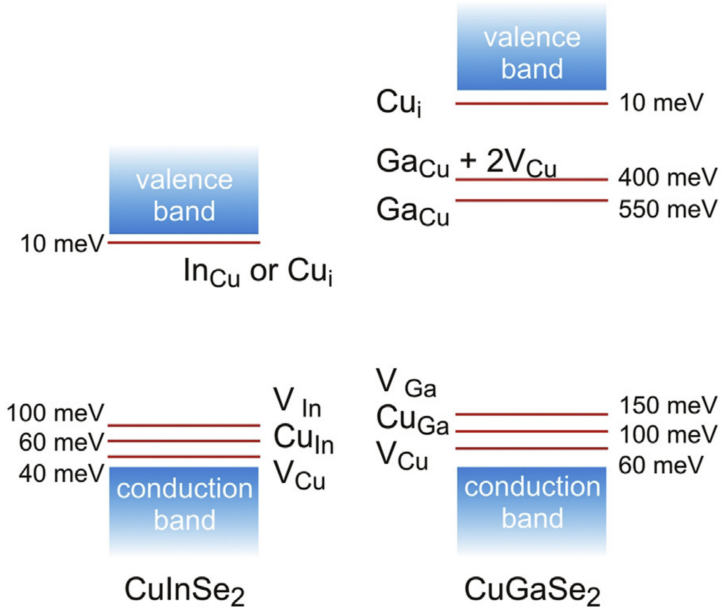

Figure 5.: Energy levels within the bandgap associated with the intrinsic point defects in CuInSe$_2$ and CuGaSe$_2$ based on currently available data from experiments and simulations. (From Ref. [10])

Consequently, a great deal of research effort, both theoretical and experimental, is related to the question of which defects cause such losses and by means of which mechanisms. However, a definitive answer is not yet available and this is an ongoing debate.

1.3.1 *Point and planar defects*

In this section we provide a short overview of the properties of point and planar defects. More comprehensive overviews about point defects in Cu(In,Ga)Se$_2$ and its parents compounds, CuInSe$_2$ and CuGaSe$_2$, have been provided by Burgelman *et al.* [73], Rau and Schock [66], Rockett [74], Siebentritt *et al.* [41] and Pohl and Albe [5]. In the case of planar defects, we recommend the reviews by Rau *et al.* [70], Abou-Ras *et al.* [9] and the habilitation monograph of Abou-Ras [75].

Regarding point defects, positron annihilation spectroscopy showed that in CuInSe$_2$ the Cu-Se double vacancy $V_{Cu} - V_{Se}$ is dominant for Cu-poor material while in the case of the Cu-rich material this role is played by the single Cu vacancy V_{Cu} [76]. The same study showed that the $V_{Cu} - V_{Se}$ is dominant in CuGaSe$_2$. Furthermore, In$_{Cu}$ and Cu$_{In}$ cation antisites in CuInSe$_2$ and Ga interstitials, Ga$_i$, in CuGaSe$_2$ have been detected by means of neutron diffraction [77, 78]. In agreement with experiments, recent state-of-the-art first-principles calcula-

tions using hybrid functionals have reported that V_{Cu}, In/Ga_{Cu}, $Cu_{In/Ga}$ and Cu_i have low formation energies in $CuInSe_2$ and $CuGaSe_2$ [5, 79, 80].

A further issue addressed by both, experiments and simulations, has been whether intrinsic point defects induce *deep levels* (see Section 3.3.3) and, therefore, represent a source of non-radiative recombination. Based on the currently available data from experiments and simulations, Siebentritt [10] recently suggested a scheme of energy levels within the bandgap associated with intrinsic point defects in $CuInSe_2$ and $CuGaSe_2$ (shown in Figure 5). As we can see there, deep defect levels in $CuGaSe_2$ are induced by the presence of Ga_{Cu} antisites. Furthermore, although not included in Figure 5, photocapacitance measurements have provided evidence of the existence of a deep level at 0.8 eV above the VBM in $Cu(In,Ga)Se_2$ independent of the gallium content [81, 82]. This observation is in line with the findings of Pohl and Albe [5]. They reported that $Cu_{In/Ga}$ antisites induce deep defect levels located at 0.62 eV and 0.75 eV above the VBM for $CuInSe_2$ and $CuGaSe_2$, respectively. Thus, point defect-induced non-radiative recombination is expected to play a role in $Cu(In,Ga)Se_2$-based solar cells. On the contrary, temperature dependent photoluminescence [83, 84] confirmed that at room temperature, the electrostatic potential variations caused by the presence of charged donor and acceptor defects are screened by free carriers. Therefore, point defect-related V_{oc} reductions are not caused by potential fluctuations.

Concerning planar defects in $Cu(In,Ga)Se_2$, it has been found that stacking faults can exhibit atomic reconstructions when they are cation-cation or Se-Se terminated. For example, by means of atom-probe tomography, Abou-Ras *et al.* [9] reported Cu depletion and In enrichment for an stacking fault which appeared to be Se-Se terminated. Consistent with the coherent nature of the stacking faults, theoretical studies focusing on their electronic structure do not report the presence of stacking fault-induced deep levels [85, 86]. However, since these studies dealt only with stacking faults with cation-Se termination, a complete picture of stacking fault properties in $Cu(In,Ga)Se_2$ is still missing. In the case of grain boundaries, an intriguing feature has been observed: polycrystalline $Cu(In,Ga)Se_2$-based solar cells tend to outperform their single crystalline counterparts [23, 24]. In fact, device simulations have shown that grain boundaries must be electrically benign and the effective recombination induced by them should be lower than 10^3 cms^{-1} for highly-efficient $Cu(In,Ga)Se_2$-based solar cells to be possible [87, 88]. Until now, most of the results reported in literature refer to highly symmetric twin boundaries. Nevertheless, these studies are relevant due to the fact that highly symmetric twin boundaries represent around 50-80% of all grain boundaries in $Cu(In,Ga)Se_2$-based solar cells [75, 89]. Experiments conducted by Abou-Ras *et al.* [90] provided evidence of the presence of cation-Se and Se-Se terminated twins in $Cu(In,Ga)Se_2$ and found atomic rearrangements in the surroundings of these boundaries. Specifically, they reported Cu depletion or no compositional change in the surroundings of the cation-Se terminated boundaries and Cu depletion accompanied by In enrichment in the case of Se-

Se terminated twins. Simulations of the electronic structure of twin boundaries revealed that stoichiometric cation-Se terminated ones cause shifts in the energy bands along with band bending and Se-Se terminated ones induce deep levels in the bandgap [91, 92]. The latter can therefore represent a source of non-radiative recombination. However, atomic reconstructions in the form of Cu depletion, as observed in experiments, could induce the creation of a hole-barrier formed at the twin boundaries [6, 70]. Such barrier would block holes from reaching the boundary region, hence preventing recombination at the defect states induced by the grain boundary [70, 93]. Gloecker *et al.* [87] showed that in order to screen holes out of the grain boundaries, barriers should be higher than 300 meV. Experiments have reported that this is the case in Cu(In,Ga)Se_2-based solar cells [94]. This is in line with catholuminescence studies, which reported no evidence of radiative recombination reduction at most twin boundaries [68, 95].

In the case of low symmetry random grain boundaries, which represent the remaining 20-50% of all grain boundaries in Cu(In,Ga)Se_2, a reduced catholuminescence intensity has been reported [96]. This reduction is a sign that they are sources of non-radiative recombination. Whether they are passivated, at least partially, by atomic reconstruction like in the case of twins, is still an unanswered question. Ongoing efforts addressing this issue are hampered by the fact that general trends for atomic rearrangements in the surroundings of random grain boundaries in Cu(In,Ga)Se_2 are not easily drawn. As pointed out by Abou-Ras *et al.* [9] and references therein, even in the same Cu(In,Ga)Se_2 absorber, different random grain boundaries exhibit dissimilar changes in composition. In addition to non-radiative recombination-related efficiency losses, electrostatic potential fluctuations of about 100 meV have been reported to occur at grain boundaries [70].

As mentioned at the beginning of this section, most reported studies on the properties of defects in $CuInSe_2$, $CuGaSe_2$ and Cu(In,Ga)Se_2 are focused on point and planar defects. Unfortunately, dislocation studies on the same materials are extremely rare. This is surprising considering the fact that dislocation densities as high as 10^{11} cm^{-2} have been reported in highly efficient Cu(In,Ga)Se_2-based solar cells. Since this thesis is focused on dislocation properties and their role in these devices, in the reminder of this chapter we will review what is currently known about this defect type.

1.3.2 *Dislocations*

Cu(In,Ga)Se_2 absorbers have a chalcopyrite structure which can be seen in Figure 6. This is a diamond-like tetragonal crystal structure equivalent to the zincblende structure but twice as large in the $[001]$ direction. From the crystallographic point of view, the $\{112\}$ planes in the chalcopyrite structure have the highest packing density and therefore act as preferred slip planes for disloca-

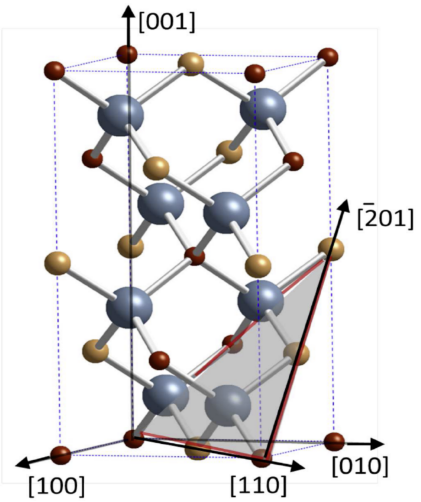

Figure 6.: Ideal $CuInSe_2$ chalcopyrite structure with a shaded area that corresponds to a {112} plane and the red lines show the directions associated with minimum lattice translations in such plane. Copper, gallium and selenium are shown as red, blue and yellow spheres, respectively. (Adapted from Ref. [97],)

tions. These planes are analogues to the {111} planes in the diamond structure. In Figure 6, the shaded area corresponds to a (112) plane and the minimum lattice translations in this plane, shown as red lines in the Figure, can be either $\frac{1}{4}\langle 201\rangle$ or $\frac{1}{2}\langle 110\rangle$. Therefore, perfect dislocations with the lowest energy in Cu(In,Ga)Se_2, occur in the {112} planes and have a Burgers vector, **b**, equal to these minimum lattice translations. Furthermore, due to the relatively deep Peierls barriers present in covalently bonded and tetrahedrally coordinated semiconductors like Cu(In,Ga)Se_2, the line direction **l** is also given, at least locally, by the minimum lattice translations in the (112) plane. Thus, energetically prefered dislocations in the chalcopyrite structure have an angle between **l** and **b** of either 0° (screw) or 60° (mixed).

Although these are the relevant perfect dislocation types, the symmetry of the Cu(In,Ga)Se_2 structure allows the cores of these dislocations to have several configurations. In the case of the 60°-mixed dislocations, these variations are defined by the termination of the inserted half-plane [98]. A general example of a 60°-mixed dislocation core is shown in Figure 7a with its inserted (112) half-plane highlighted by the shaded region and its direction marked by a red line. The possible configurations of this structure can be easily understood with the help of Figure 7b, where two dashed lines indicate the possible terminations of the inserted half-plane. If the inserted half-plane terminates on the closely spaced {112} planes, the core belongs to the glide set (indicated with the corresponding

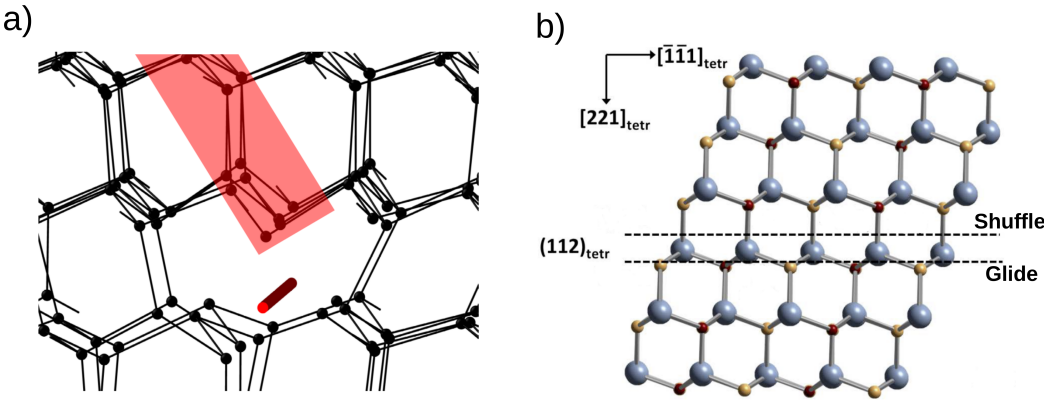

Figure 7.: General structure of a 60°-mixed dislocation with highlighted inserted (112) half-plane and line direction marked by a red bold line (a). Projection of the Cu(In,Ga)Se$_2$ structure with glide and shuffle $\{112\}$ planes pointed as dashed lines (b). Copper, gallium and selenium are shown as red, blue and yellow spheres, respectively. (Figure on the right was adapted from Ref. [97], ©2013 *by Jens Dietrich, available under the terms and conditions of the Creative Commons Attribution 2.0 License* `https://creativecommons.org/licenses/by-nc-nd/2.0/`)

dashed line). On the contrary, if this plane terminates on the widely spaced ones, we have a shuffle core [98–100]. Furthermore, in Figure 7b it is also possible to see that for both, glide and shuffle, cores the inserted half-plane can terminate either in a row of cations or a row of anions. Thus, the 60°-mixed dislocation core can be either cation- or anion-rich. The former is called α-core and the latter β-core [13, 101]. In the case of screw dislocations, since they do not introduce an inserted half-plane, the different core configurations refer to the location of the dislocation center [102]. It belongs to the glide set if its centers is located between two closely spaced $\{112\}$ planes and therefore is located on the lower dashed line in 7b. On the other hand, if the center is located between two widely spaced $\{112\}$ planes, as it is the case of the upper dashed line in the same figure, it belongs to the shuffle set. Cation- or anion-rich core configurations are non-existent for screw dislocations.

Let us now compare the conclusions of this crystallography based analysis with the reported findings on the issue. Early experimental studies on dislocations in chalcopyrite-type single crystals were provided by Pasemann and Klimanek [103] and Pasemann, Klimanek and Oettel [104]. These studies focused on the plastically deformed $ZnSiP_2$ semiconductor. Later on, also focusing on deformed samples, transmission electron microscopy (TEM) results were reported for natural chalcopyrite ($CuFeS_2$) [105–107]. It was until 1991 that the first analysis of dislocations in $CuInSe_2$ was provided by Kiely *et al.* [108]. In there, they report the results of a TEM study focusing on both single crystals and polycrys-

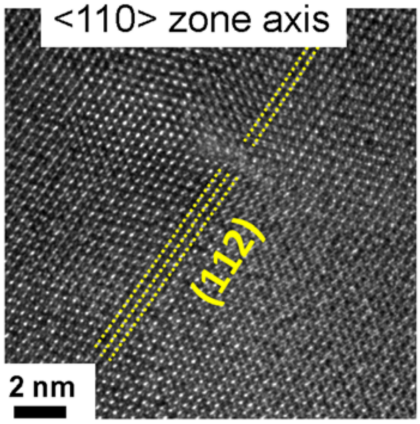

Figure 8.: High-resolution TEM measurement of a Cu(In,Ga)Se$_2$ sample containing a perfect 60°-mixed dislocation. The sample is oriented in the $[110]$ direction and the $\{112\}$ planes are pointed out by yellow lines. (Adapted and reprinted from Ref. [13] with the permission of AIP publishing)

talline samples. However, despite being an interesting and valuable effort, this study was performed on $CuInSe_2$ samples whose efficiency as absorber was far from the current records. Furthermore, their samples were grown by means of a process different to the one used for state-of-the-art-devices devices. Although they found dislocations in their single crystals, they did not report or examine dislocations in the polycrystalline samples they analyzed.

As mentioned at the beginning of this chapter, published studies on the properties of dislocations in polycrystalline Cu(In,Ga)Se$_2$ thin films in high-efficient solar cells are scarce. Nevertheless, recent efforts by Dietrich *et al.* [11–13] have provided reliable and helpful information on the matter. Based on high-resolution TEM measurements (one example is shown if Figure 8), they reported the existence of perfect 60°-mixed dislocations with an introduced $\{112\}$ plane, $\mathbf{b} = \frac{1}{4}[201]$ and $\mathbf{l} = \frac{1}{2}[110]$. These findings are in line with the crystallography analyis presented before and are analogous to the situation encountered in Si crystals [109]. However, contrary to what has been reported for Si, Dietrich *et al.* [11–13] found a rather low frequency of dissociated dislocations and stacking faults.

An interesting observation is that dislocations in fully grown Cu(In,Ga)Se$_2$ are most likely to appear in regions of the absorber with strong local variations in the [Ga]/([Ga]+[In]) compositional ratio [11, 12]. In the same studies it is concluded that dislocation densities as high as 10^{10} -10^{11} cm^{-2} are caused by the difference in lattice parameters of $CuInSe_2$ and $CuGaSe_2$. Specifically, when a threshold of 12-13%/μm in the linear In/Ga gradients is exceeded within a given grain.

Regardless of their origin, the most intriguing result is that such high dislocation densities are found in devices which at the same time show power-

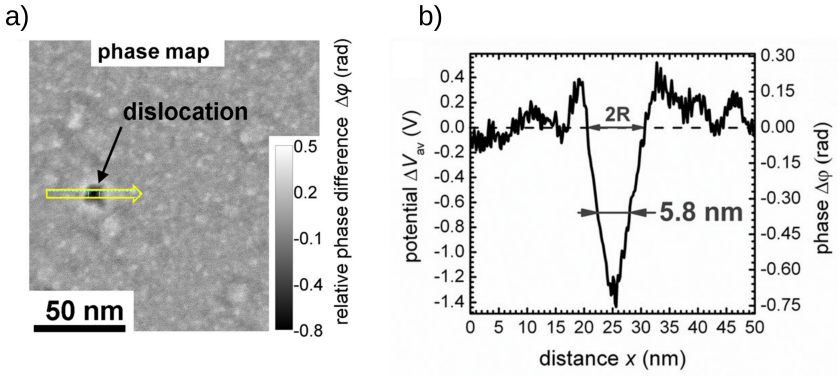

Figure 9.: Spatial variations of the phase around a dislocation in Cu(In,Ga)Se$_2$ (a). In there, a yellow arrow indicates the direction and extent of the phase and average electrostatic potential profile shown in (b). (Adapted and reprinted from Ref. [13] with the permission of AIP publishing)

conversion efficiencies of more than 15% [13]. Such behavior is in contrast to what has been reported for other semiconductor materials, e.g. in GaN the presence of dislocations strongly modifies the electrical properties of the material. [110, 111] This implies that lattice dislocations in Cu(In,Ga)Se$_2$-based absorbers are electrically inactive or passivated by point defect segregation.

Dietrich *et al.* [13] provided a first attempt to explain the apparent harmless nature of dislocations in Cu(In,Ga)Se$_2$-based solar cells. By means of inline electron holography experiments, they observed potential wells at various dislocations in Cu(In,Ga)Se$_2$ and measured the average electrostatic potential, ΔV_{av}, around these defects. An example is shown in Figure 9b, where the measurement is carried out along the path indicated by the yellow arrow in Figure 9a. In total, they studied 18 dislocations and potential wells like the one in the figure were found for ten of those defects. The remaining eight dislocations did not show evidence of an induced potential well.

Since the variation of ΔV_{av} local minima at different dislocations is quite small, they concluded that the potential wells should have similar origin. Based on simulations, they found that the influence of strain fields and charge accumulations was rather small and rule them out as plausible causes of the observed wells. Nevertheless, a third possible explanation was proposed based on atom probe tomography (APT) measurements: Na accumulation and Cu depletion in the surroundings of the dislocation cores. As we can see in the APT data cube displaying the Na distribution accross a Cu(In,Ga)Se$_2$ sample shown in Figure 10a, the Na signal is enhanced along two line features, D1 and D2, which can be related to dislocation cores. Furthermore, based on this APT data, they analyzed the elemental distributions around the line feature D1 as it is presented in Figure 10b. Besides the local maxima observed for Na and K concentrations,

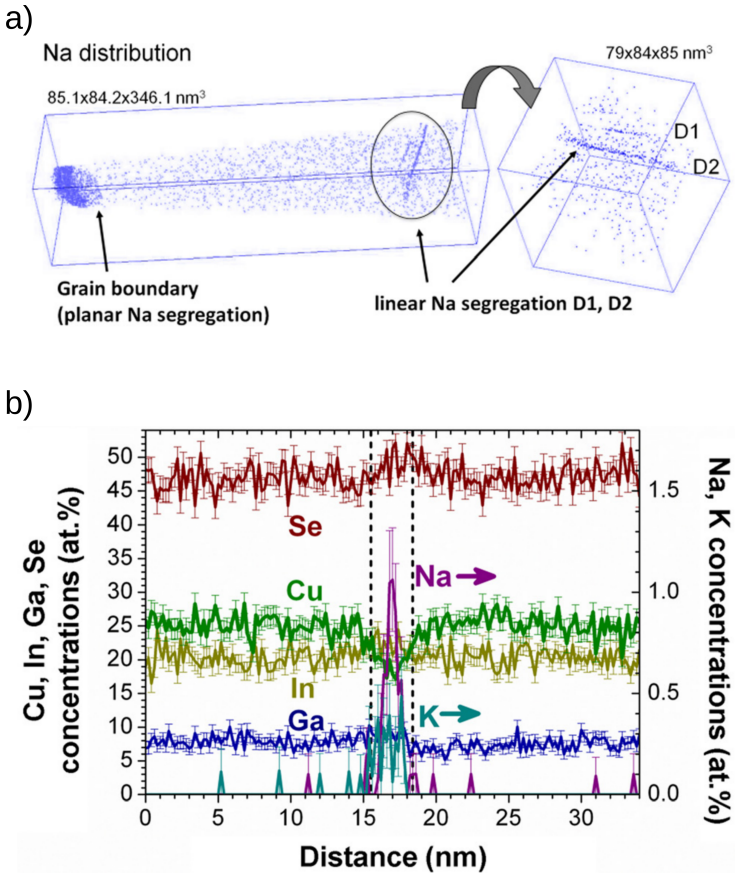

Figure 10.: APT data cube displaying the Na distribution accros the crystal with two line features, D1 and D2, showing an enhanced Na signal (a) and elemental distribution accros the defect D1 in the figure above (b). (Adapted and reprinted from Ref. [13] with the permission of AIP publishing)

they found a considerable reduction in the Cu signal. Moreover, no considerable change in the In, Ga and Se concentrations is reported. Similar trends were found for the D2 defect. The authors recognized that since only few of these datacubes exhibit line features, the statistics of their findings are very poor.

To test whether this third possible cause of the potential wells is actually correct, Dietrich *et al.* [13] feed the chemical changes they found with the help of the APT into a simulation model. In Figure 11, the comparison between the results of their calculation of the mean-inner potential and the experimental potential around the D1 dislocation is shown. Based on these findings, they concluded that changes in composition, as the ones observed in experiments, can indeed account for the potential wells around dislocations.

Afterwards, Dietrich *et al.* [13] proposed an structural model which could account for the observed Na accumulation and Cu depletion. Their idea is shown

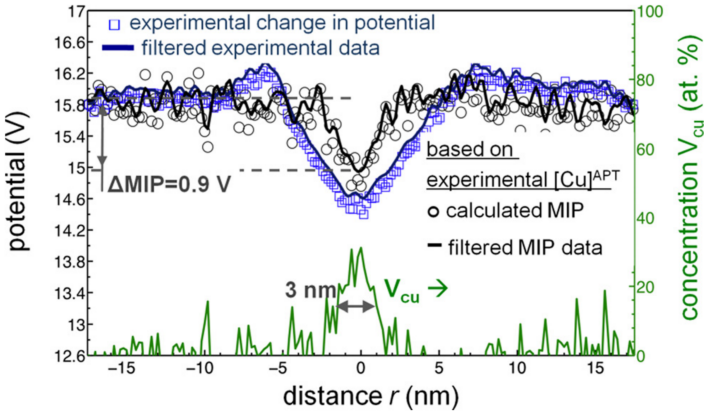

Figure 11.: Calculated mean inner potential for the elemental distributions found with the help of the APT. For comparison, the measured potential is also shown as open squares. (Adapted and reprinted from Ref. [13] with the permission of AIP publishing)

in Figure 12. They start by assuming that all atoms at the termination of the half-plane are not fully coordinated and thus exhibit unsaturated dangling bonds. This excess charge would then be compensated by segregating charged intrinsic defects like V_{Cu}^{-1} and $In_{Cu}^{+2}/Ga_{Cu}^{+2}$ for the cation- and anion-rich cores, respectively. The key ingredient of their proposal is that if Na_{Cu} segregates into the termination of the inserted half-plane, the charge compensation is no longer attained and excess charge is again located at the termination of the inserted half-plane. In the case of the cation-rich core, they propose that the remaining positive line charge after Na_{Cu} is segregated, would be compensated by a field-driven Cu depletion away from the core. Based on their data, they concluded that such depletion would occur in a region of about 3 nm around the dislocation and would create a potential well, as explained before. In the case of the anion-rich core, the Na_{Cu} segregation would only mean a field-driven depletion of $In_{Cu}^{+2}/Ga_{Cu}^{+2}$ defects. Since the ionic scattering factor of Cu and of $In_{Cu}^{+2}/Ga_{Cu}^{+2}$ do not differ considerably and the fact that only negligible changes in the atomic density are expected from substitution of Cu by In, Dietrich *et al.* [13] concluded that no potential well is expected in anion-rich cores. These conclusions are in line with the fact that they did not find potential wells for all the dislocations studied.

Regarding the effect of these dislocations on the power-conversion efficiency of a Cu(In,Ga)Se$_2$-based solar cells, Dietrich *et al.* [13] argued that the Cu depletion observed for the cation-rich cores could induce a lowering of the VBM [6]. As a consequence of the lower VBM close to the dislocation compared to its value in the surrounding bulk, a barrier for holes would be formed and recombination would be reduced. They suggest this hole-barrier could be one reason why dis-

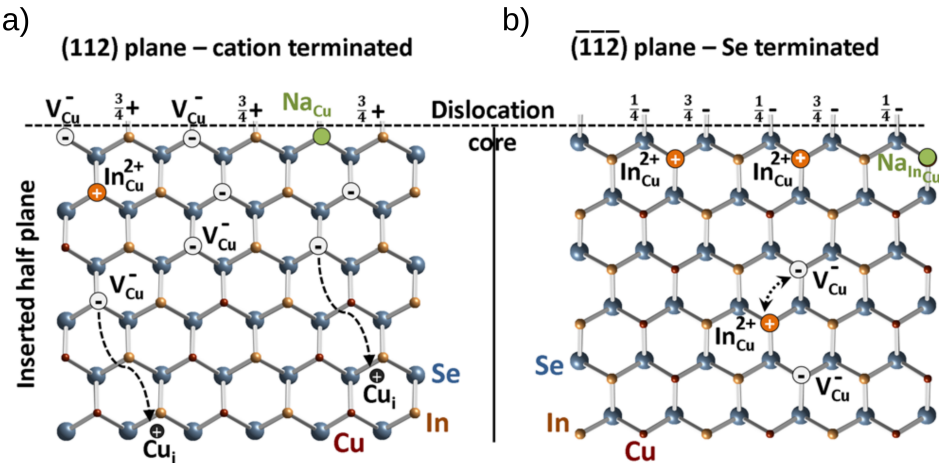

Figure 12.: Structural model for the inserted half-planes of the 60°-mixed dislocation core in $CuInSe_2$ including Na and intrinsic defects. The termination of the half-plane is at the top section of the figure. The model is proposed for both cation-rich core (a) and anion-rich core (b). Such model can be extended for the $CuInSe_2$ case. (Adapted and reprinted from Ref. [13] with the permission of AIP publishing)

locations are apparently harmless. In the case of Se-terminated {112} surfaces, corresponding to anion-rich cores, no significant band-offset or hole-barrier is induced. At the end of their study, Dietrich *et al.* [13] recognized that their model and conclusions need confirmation from first-principles calculations.

At the beginning of this section, we analyzed the possible perfect dislocations that could occur in the chalcopyrite structure. However, partial dislocations were left out of the discussion. As stated before, this was done because fully grown samples of highly-efficient Cu(In,Ga)Se_2-based solar cells exhibit a rather low frequency of dissociated dislocations and stacking faults [11–13]. Nevertheless, interstitial (extrinsic) Frank loops were observed in $CuInSe_2$ samples irradiated with 400 keV Xe ions [113]. This defect consists of a {112} extra layer inserted into

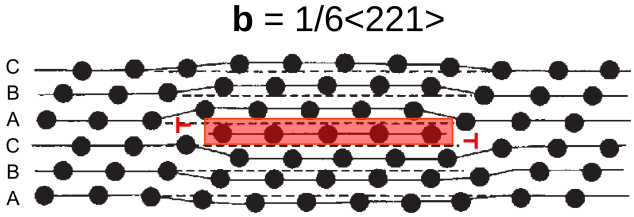

Figure 13.: Structure of an interstitial Frank loop in the chalcopyrite structure. Also shown are the two transversal section of its bounding Frank partial dislocation with $\mathbf{b} = \frac{1}{6}\langle 221 \rangle$ Burgers vector. (Adapted and reprinted from Ref. [100] with permission of Elsevier)

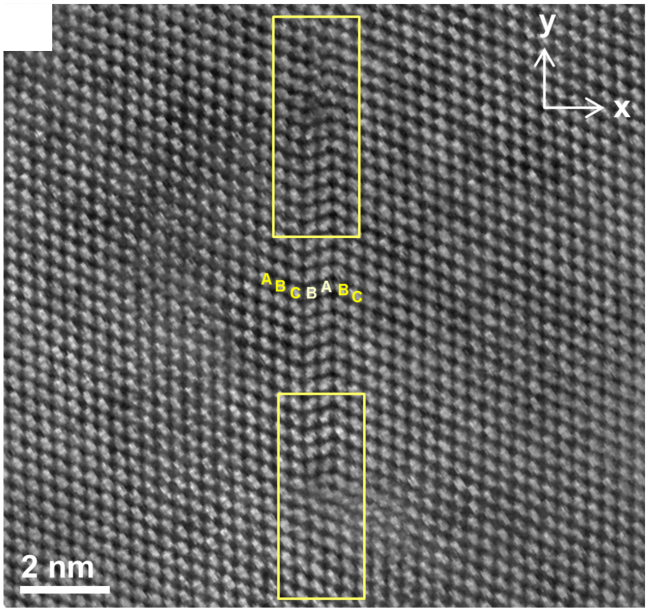

Figure 14.: TEM micrograph of a Frank loop transversal section in a Cu(In,Ga)Se_2 sample whose growth process was interrupted before reaching the efficiency boosting Cu-rich stage. (This figure was first published in Ref. [112])

the lattice, as can be seen in Figure 13. In order to understand the crystallogryphy of this defect, let us first say that three different layers can be identifed in the chalcopyrite structure and they are called A, B and C. A pristine sample would have an ABCABC... stack sequence, whereas in the presence of the loop the sequence would be ABC**B**ABC... as it is shown in the Figure 14. As mentioned before, the boundary between a stacking fault and the perfect crystal is a partial dislocation. In the case of the interstitial Frank loop in the chalcopyrite lattice, the stacking fault is bound by a Frank partial with $\mathbf{b} = \frac{1}{6}\langle 221 \rangle$.

Although not found in fully grown samples of high-efficient Cu(In,Ga)Se_2-based solar cells, new findings discussed in this thesis bring Frank loops and partials into the spotlight (see Chapter 4). Collaborators within the scientific consortium in which this thesis was carried out, performed TEM measurements on samples whose growth process was interrupted before reaching the efficiency boosting Cu-rich stage [46, 49, 114] and found evidence of the existence of Frank loops in these samples, see Figure 14. Since the Cu-rich stage promotes planar defect annhilation [50, 115], the disappearance of these loops could be related to the efficiency boost occurring in this stage of the growth process.

1.4 OPEN QUESTIONS

In Part III of this thesis, we present the first complete study of the structural and electronic properties of Frank loops and perfect dislocations in $CuInSe_2$ and $CuGaSe_2$. Furthermore, we investigate the segregation of defects and Na in the surroundings of these dislocations and compare our findings with what has been reported in literature. These results allow us to shed light on the physical mechanism behind the apparent harmless nature of dislocations in $Cu(In,Ga)Se_2$-based solar cells. Our analysis is based on state-of-the-art first principles calculations and we aim to answer the following questions:

- Are the stoichiometric Frank partials observed in not fully grown $Cu(In,Ga)Se_2$ samples electrically active?
- Do these Frank partials prefer to be non-stoichiometric by means of intrinsic point defect segregation?
- If this segregation is preferred, which is the driving force for such process?
- If segregation is prefered, which point defects are expected to occur in the Frank partial cores and their surroundings?
- Are the electronic properties of Frank partials in not fully grown $Cu(In,Ga)Se_2$ samples affected by segregation of intrinsic point defects?
- Since the Cu-rich stage is expected to annihilate the Frank loops in $Cu(In,Ga)Se_2$, can our results provide insights about the physical mechanism behind the efficiency boost observed in this stage?
- Are the stoichiometic screw and 60°-mixed dislocations in $CuInSe_2$ and $CuGaSe_2$ electrically active? What about $Cu(In,Ga)Se_2$?
- If they are active, what is the origin of such behavior?
- For stoichiometric 60°-mixed dislocation cores in $Cu(In,Ga)Se_2$, Dietrich *et al.* [13] proposed that all atoms at the termination of the inserted half-plane exhibit unsaturated dangling bonds. Is that picture correct?
- Does Na prefer to segregate into the 60°-mixed dislocation cores as proposed by Dietrich *et al.* [13]? and if it is actually prefered, which is the driving force of this process?
- If the Na segregation does occur, are the electronic properties of 60°-mixed dislocation cores in $Cu(In,Ga)Se_2$ affected?
- Is the structural model proposed by Dietrich *et al.* [13] correct?

- Based on the answers to these questions, can we explain why dislocations in Cu(In,Ga)Se_2 appear to be harmless?

Part II

METHODS

The following part introduces the basics of density functional theory (DFT), one of the most popular and succesful quantum mechanical approaches to study materials. Along with its basics, we present an overview of the application of DFT to study defects in semiconductors. Specifically, we discuss the details of dislocation simulation techniques as used in this thesis to carry out the study presented in Part III.

2

DENSITY FUNCTIONAL THEORY

2.1 INTRODUCTION

As stated before, in this thesis we aim at obtaining an accurate description of the structural and electronic properties of dislocations in Cu(In,Ga)Se_2 and its parent compounds by means of computer simulations. As depicted in Figure 15, there are different methods available to simulate materials. Each of these methods is useful for certain time-length scales. In our case, we cannot neglect the quantum nature of electrons and we need to solve the Schrödinger equation. However, the direct solution of this equation for any system of interest is an intractable problem due to what Walter Kohn called *exponential wall* [116]. An excellent example useful to understand the meaning of this concept was introduced by Kohn in his Nobel lecture [116] and later refined by Blöchl [117]. In here we present the version of the latter:

> "...imagine the wave function of a N_2 molecule, having two nuclei and fourteen electrons. For N particles, the Schrödinger equation is a partial differential equation in $3N$ dimensions. Let us express the wave function on a grid with about 110 points along each spatial direction and let us now consider two spin states for each electron. Such wave function is represented by $2^{14}100^{3*16} \sim 10^{100}$ complex numbers. A data server for this amount of data, made of current terabyte hard disks, would occupy a volume with a diameter of 10^{10} light years!"

This analysis points out the need for an affordable alternative method in order to tackle real problems. In the 1960s, Hohenberg and Kohn [118] and Kohn and Sham [118] proposed to reformulate quantum mechanics in terms of the electronic density, which depends only on the three spatial coordinates, instead of using the many-body wave function, which depends on $3N$ coordinates of N electrons. Such step forward meant the birth of density functional theory (DFT), which is the method we use throughout this thesis.

Our aim in this section is to provide a short introduction to the basic principles of DFT and the details of its application to crystalline solids. However, by no means this is a thorough treatment of this beautiful theory. For detailed

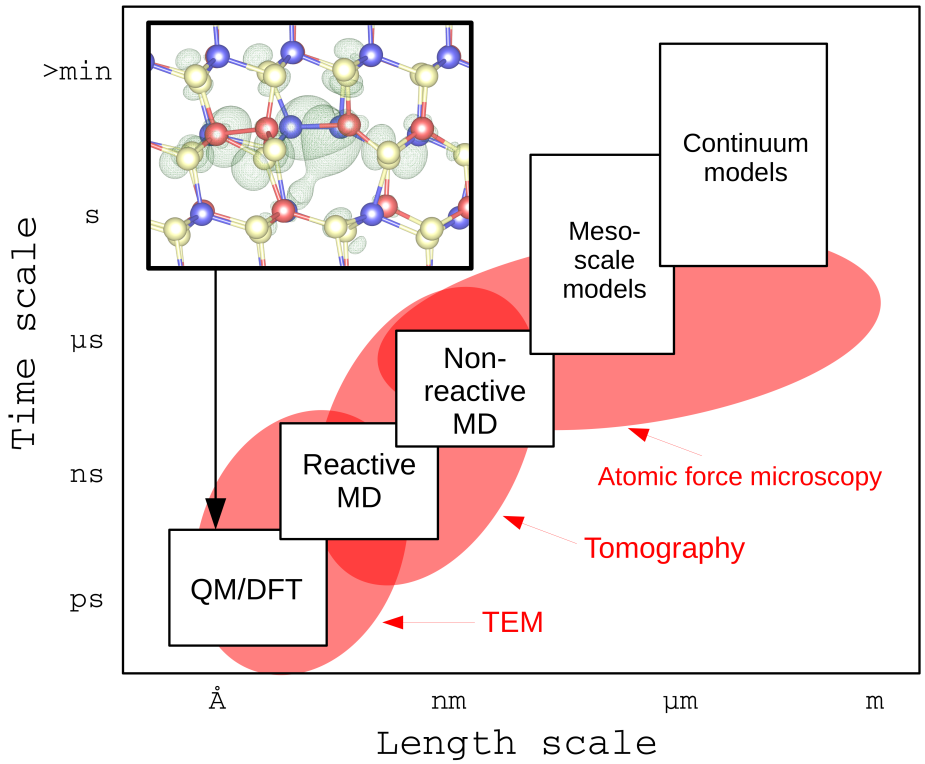

Figure 15.: Diagram of the time and length scales accesible to the different methods available to simulate materials. For completeness, red shaded regions provide the same information for the available experimental techniques. In here, QM and MD stands for quantum mechanics and molecular dynamics, respectively. The inbox shows a typical problem which needs quantum mechanics to be solved: the charge density isosurface of an electronic state caused by a defect in $CuInSe_2$

discussions on the subject we strongly recommend the books by Martin [119], Kohanoff [120] and Engel [121]. Furthermore, excellent introductions to DFT are also provided by Jones and Gunnarsson [122] and Jones [123], which give a complete overview of the historic development of the theory. A final reference we would like to highlight is the recent review by Cohen *et al.* [124], which points out the many issues to be solved in DFT and how this theory is still far from complete.

2.2 THE HAMILTONIAN FOR THE ELECTRONS IN A SOLID

Let us start with the definition of the Hamiltonian $\hat{H}$ for a system comprised of electrons and nuclei given by [119, 120]

$$\begin{aligned}\hat{H} = &-\frac{\hbar^2}{2m_{\mathrm{e}}}\sum_i \boldsymbol{\nabla}_i^2 - \sum_i\sum_I \frac{e^2 Z_{\mathrm{I}}}{|\mathbf{R}_{\mathrm{I}} - \mathbf{r}_i|} + \frac{1}{2}\sum_{i\neq j}\frac{e^2}{|\mathbf{r}_i - \mathbf{r}_j|} \\ &- \frac{\hbar^2}{2}\sum_I \frac{\nabla_I^2}{M_{\mathrm{I}}} + \frac{1}{2}\sum_{I\neq J}\frac{e^2 Z_{\mathrm{I}} Z_{\mathrm{J}}}{|\mathbf{R}_{\mathrm{I}} - \mathbf{R}_{\mathrm{J}}|},\end{aligned} \tag{2.1}$$

where upper case letters and subscripts refer to quantities associated to the nuclei, i.e. R_I, M_I and Z_I are the coordinates, mass and charge of nucleus I, respectively. Lower case letters and subscripts correspond to their electronic counterparts, i.e. r_i, m_e and e refer to the coordinates, mass and charge of electron i, respectively. Regarding the physical meaning of this Hamiltonian, its first and fourth terms are the operators for the kinetic energies of nuclei and electrons, respectively. The remaining second, third and fifth terms account for, in the same order, the interactions between electrons-nuclei, electron-electron and nuclei-nuclei.

Based on the fact that nuclei are much heavier than electrons (the mass of a single proton or neutron is about 1835 times larger than the electron mass), they are expected to move much more slowly than electrons. This is the physical principle behind the *Born-Oppenheimer approximation* [125] or *adiabatic approximation*, which allow us to decouple the electronic system from the nuclei, i.e. we can construct a Hamiltonian for the electrons inmersed in a field generated by a static configuration of nuclei. Such electronic Hamiltonian is given, in atomic units, by

$$\hat{H}_{el} = \underbrace{-\frac{\hbar^2}{2m_{\mathrm{e}}}\sum_i \boldsymbol{\nabla}_i^2}_{\hat{\mathrm{T}}} + \underbrace{\sum_i v_{\mathrm{ext}}(\mathbf{r}_i)}_{\hat{V}_{\mathrm{ext}}} + \underbrace{\frac{1}{2}\sum_{i\neq j}\frac{e^2}{|\mathbf{r}_i - \mathbf{r}_j|}}_{\hat{V}_{\mathrm{ee}}}, \tag{2.2}$$

where $\hat{T}$ is the operator for the kinetic energy of the electrons, $\hat{V}_{\mathrm{ext}}$ is the interaction of the electrons with the external potential $v_{\mathrm{ext}}(\mathbf{r})$ generated by the fixed nuclei and $\hat{V}_{\mathrm{ee}}$ accounts for the electron-electron interactions.

2.3 THE ELECTRONIC DENSITY AS THE BASIC VARIABLE

The dynamics of a quantum mechanical system, like the one described in Equation 2.2, is defined by the non-relativistic time-dependent Schrödinger equation

$$\left[i\hbar\partial_t + \hat{H}_{el}\right]\Psi(\mathbf{r}, t) = 0, \tag{2.3}$$

where $\Psi(\mathbf{r}, t)$ is the many-electron wave function. Nevertheless, for most systems it is sufficient to solve the time-independent version given by

$$\hat{H}_{el}\Psi(\mathbf{r}) = E\Psi(\mathbf{r}). \tag{2.4}$$

As mentioned before, the direct solution of this equation cannot be obtained for real systems. Approaches to overcome this difficulty are focused on replacing the complex many-electron wave function by simpler objects. A first proposal, which contained the complete quantum mechanical nature of electrons, is the Hartree-Fock (HF) method [126, 127]. In there, the many-electron wave function is assumed to have the form of a single Slater determinant (not including the spin) given by

$$\Psi_{HF}(\mathbf{r}_1, \mathbf{r}_2, ..., \mathbf{r}_N) = \frac{1}{\sqrt{N!}} \begin{vmatrix} \phi_1(\mathbf{r}_1) & \phi_1(\mathbf{r}_2) & \dots & \phi_1(\mathbf{r}_N) \\ \phi_2(\mathbf{r}_1) & \phi_2(\mathbf{r}_2) & \dots & \phi_2(\mathbf{r}_N) \\ \dots & & & \\ \phi_N(\mathbf{r}_1) & \phi_N(\mathbf{r}_2) & \dots & \phi_N(\mathbf{r}_N) \end{vmatrix}, \tag{2.5}$$

where N and $\mathbf{r}_{1,...,N}$ are the number and positions of the electrons in the system, respectively, and the $\phi(\mathbf{r})$ are the single-particle orbitals to be obtained in the calculation. Using this Slater determinant, the HF method is able to account exactly for the *exchange interaction* between electrons, which arises from the antisymmetry of the electronic wave functions. Nevertheless, it does so at a high computational expense.

A second and more powerful alternative was suggested by Hohenberg and Kohn [118], who proposed to replace the many-electron wave function by the electronic density $n(\mathbf{r})$ (not including the spin) given by

$$n(\mathbf{r}) = \mathrm{N} \int \mathrm{d}\mathbf{r}_2 ... \mathrm{d}\mathbf{r}_\mathrm{N} \Psi^*(\mathbf{r}, \mathbf{r}_2, ..., \mathbf{r}_\mathrm{N}) \Psi(\mathbf{r}, \mathbf{r}_2, ..., \mathbf{r}_\mathrm{N}). \tag{2.6}$$

Their work represents the backbone of DFT and it is contained in the following two theorems [119]:

- **Theorem I**: For any system of interacting particles in an external potential $v_{\mathrm{ext}}(\mathbf{r})$, the potential $v_{\mathrm{ext}}(\mathbf{r})$ is determined uniquely, except for a constant, by the ground state particle density $n_0(\mathbf{r})$.
  - **Corollary I**: Since the Hamiltonian is thus fully determined, except for a constant shift of the energy, it follows that the many-body wave functions for all states (ground and excited) are determined. Therefore, all properties of the system are completely determined only by the ground state density $n_0(\mathbf{r})$.
- **Theorem II**: A *universal functional* for the energy $E[n(\mathbf{r})]$, in terms of the density, $n(\mathbf{r})$ can be defined for any external potential $v_{\mathrm{ext}}(\mathbf{r})$. For any

particular $v_{ext}(\mathbf{r})$, the exact ground state energy of the system is the global minimun value of this functional, and the density $n(\mathbf{r})$ that minimizes the functional is the exact ground state density $n_0(\mathbf{r})$.

The first of these theorems shows that the ground state electronic density $n_0(\mathbf{r})$, the ground state wave function Ψ_0 and the external potential $v_{ext}(\mathbf{r})$ determine each other uniquely. In consequence, the Hamiltonian is also determined by $n_0(\mathbf{r})$. The second theorem gives us a hint on how to calculate a very valuable information: the ground state energy E_0. The energy functional $E[n(\mathbf{r})]$ defined by Hohenberg and Kohn has the following form (not including the interaction between nuclei)

$$E\left[n(\mathbf{r})\right] = \int \mathrm{d}\mathbf{r} v_{ext}(\mathbf{r}) n(\mathbf{r}) + F\left[n(\mathbf{r})\right], \tag{2.7}$$

where $F\left[n(\mathbf{r})\right]$ is given by

$$F\left[n(\mathbf{r})\right] = \left\langle \Psi\left[n(\mathbf{r})\right] \mid \hat{T} + \hat{V}_{ee} \mid \Psi\left[n(\mathbf{r})\right] \right\rangle, \tag{2.8}$$

which is an universal functional by construction and includes all internal energies of the electronic system. The ground state energy can then be obtained by minimizing $E\left[n(\mathbf{r})\right]$ as

$$E_0 = \min_{n(\mathbf{r})} E\left[n(\mathbf{r})\right], \tag{2.9}$$

which is analogous to the variational principle of quantum mechanics but performed over the electronic density. It must be noticed that the form of the universal functional is unknown.

2.4 THE ENGINE OF DFT

Up to this point it has been shown that the Schrödinger equation can be rewritten using the electronic density as a variable. However, we still cannot solve it. A year after the basic theorems of DFT were proposed, Kohn and Sham [128] came up with the brilliant idea needed to overcome this predicament: *replace the complicated many-body system with interacting electrons by an auxiliary independent-particle system which can be solved more easily*. As illustrated in Figure 16, such construction relies on the assumption that the $n_0(\mathbf{r})$ of the many-body system of interest is equal to the one of the chosen auxiliary system. Their idea allows us to study the many-body system by solving a set of coupled independent-particle equations associated with the auxiliary system. These independent-particle equations, known as *Kohn-Sham equations*, can be considered exactly soluble within the precision of the numerical scheme used to solve them.

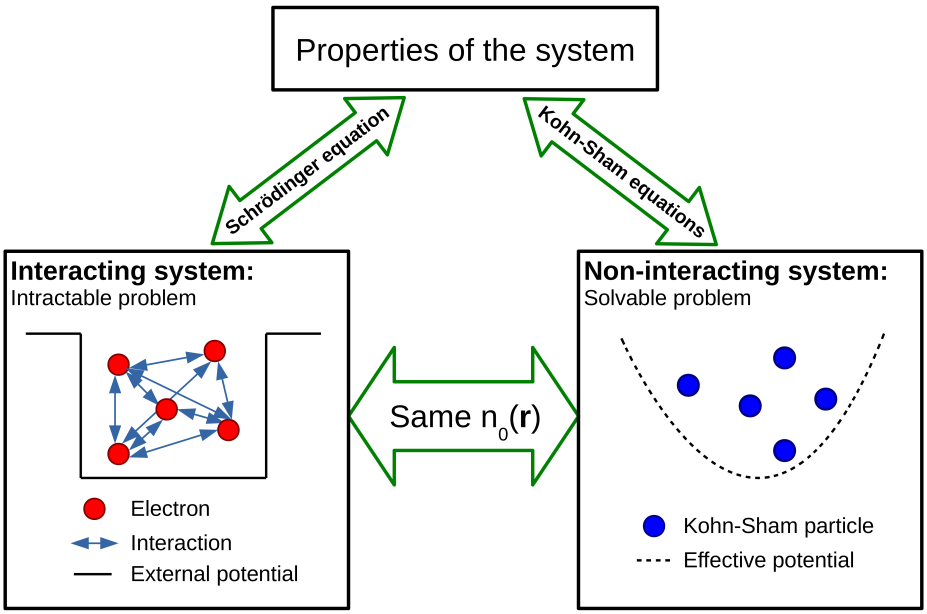

Figure 16.: Schematic of the Kohn-Sham proposal of replacing the complicated many-body system with interacting electrons by an auxiliary independent-particle system with the same ground state density $n_0(\mathbf{r})$. The particles in the auxiliary system are called Kohn-Sham particles.

Let us now focus on the mathematical machinery behind the Kohn and Sham approach. In their scheme, the universal functional $F[n(\mathbf{r})]$ has the following form:

$$F_{KS}[n(\mathbf{r})] = T_s[n(\mathbf{r})] + \underbrace{\frac{1}{2}\int\int d\mathbf{r}d\mathbf{r}'\frac{n(\mathbf{r})n(\mathbf{r}')}{|\mathbf{r}-\mathbf{r}'|}}_{E_{Hartree}[n(\mathbf{r})]} + E_{xc}[n(\mathbf{r})], \tag{2.10}$$

where $T_s[n(\mathbf{r})]$ is the kinetic energy of a system of non-interacting electrons with density $n(\mathbf{r})$, $E_{Hartree}[n(\mathbf{r})]$ is the Hartree energy which is the classical Coulomb interaction energy for the electron density $n(\mathbf{r})$ interacting with itself, and $E_{xc}[n(\mathbf{r})]$ is the *exchange-correlation* energy in which all many-body effects are isolated. All terms in Equation 2.10 can be evaluated exactly except for $E_{xc}[n(\mathbf{r})]$. If this term would be known, then the exact E_0 for the interacting system could be calculated using the auxiliary system. However, only approximations for $E_{xc}[n(\mathbf{r})]$ are attainable (see next section). The energy of such a system can be obtained by replacing $F[n]$ by $F_{KS}[n]$ in Equation 2.7 as

$$E_{KS}[n(\mathbf{r})] = T_s[n(\mathbf{r})] + \int d\mathbf{r}v_{\text{ext}}(\mathbf{r})n(\mathbf{r}) + E_{Hartree}[n(\mathbf{r})] + E_{xc}[n(\mathbf{r})]. \tag{2.11}$$

We can apply the variational principle and obtain

$$\frac{\delta E_{KS}\left[n(\mathbf{r})\right]}{\delta n(\mathbf{r})} = \frac{\delta T_s\left[n(\mathbf{r})\right]}{\delta n(\mathbf{r})} + v_{\text{ext}} + \int \mathrm{d}\mathbf{r}' \frac{n(\mathbf{r}')}{|\mathbf{r}-\mathbf{r}'|} + \frac{\delta E_{xc}\left[n(\mathbf{r})\right]}{\delta n(\mathbf{r})} = \Gamma, \tag{2.12}$$

where Γ is the Lagrange multiplier associated with the conservation of the number of particles in the system. The corresponding equation for a system also composed by non-interacting electrons with the same density but under the influence of an effective potential $V_{eff}\left[n(\mathbf{r})\right]$ is equal to

$$\frac{\delta E\left[n(\mathbf{r})\right]}{\delta n(\mathbf{r})} = \frac{\delta T_s\left[n(\mathbf{r})\right]}{\delta n(\mathbf{r})} + V_{eff}\left[n(\mathbf{r})\right] = \Gamma. \tag{2.13}$$

Comparing both, Equations 2.12 and 2.13, we see that the problems are equivalent if

$$V_{eff}\left[n(\mathbf{r})\right] = v_{\text{ext}} + \int \mathrm{d}\mathbf{r}' \frac{n(\mathbf{r}')}{|\mathbf{r}-\mathbf{r}'|} + \frac{\delta E_{xc}\left[n(\mathbf{r})\right]}{\delta n(\mathbf{r})}. \tag{2.14}$$

Therefore, the dynamics of the independent-particles in the auxiliary system, called *Kohn-Sham particles*, is determined by the following single-particle Schrödinger equations, i.e. the previously mentioned Kohn-Sham equations,

$$\underbrace{\left[-\frac{1}{2}\nabla^2 + V_{eff}\left[n(\mathbf{r})\right]\right]}_{\hat{H}_{KS}} \phi_i^{\text{KS}}(\mathbf{r}) = \varepsilon_i \phi_i^{\text{KS}}(\mathbf{r}), \tag{2.15}$$

with $\phi_i^{\text{KS}}(\mathbf{r})$ being the single-particle *Kohn-Sham orbitals* and ε_i their corresponding energies. The density of such system is given by

$$n(\mathbf{r}) = \sum_{i=1}^{N} f_i |\phi_i^{\text{KS}}(\mathbf{r})|^2, \tag{2.16}$$

where f_i are the occupation numbers of the Kohn-Sham orbitals. As we can see in Equations 2.15 and 2.16, the solutions of the Kohn-Sham equations depend on the electronic density and, at the same time, the density depends on the Kohn-Sham orbitals. Such non-linear problem can be solved by means of a self-consistent cycle, as the one shown in Figure 17. The first step of this scheme is to select an initial density $n_{init}(\mathbf{r})$. Although, any positive function normalized to the total number of electrons would be sufficient, a dramatic speed-up in the calculation is achieved when an educated guess is used instead [119, 120]. In the second step, the Hartree and exchange-correlation terms of the effective potential in Equation 2.14 are evaluated for $n_{init}(\mathbf{r})$. The external potential is typically constructed by a superposition of nuclear potentials or pseudo-potentials (see Section 2.6) centered at the atomic positions. At this point, $V_{eff}\left[n(\mathbf{r})\right]$ and $\hat{H}_{KS}$

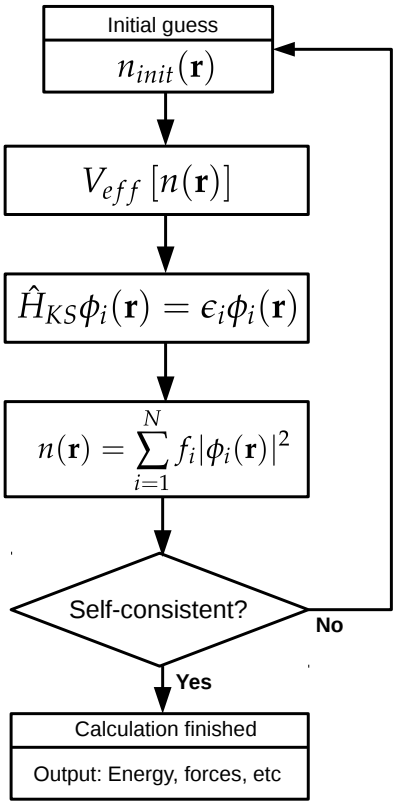

Figure 17.: Flowchart of the generic self-consistent cycle used to solve the Kohn-Sham equations.

are defined and we can proceed to solve the Kohn-Sham equations in the third step of the cycle. The solution of the Kohn-Sham equations is usually done by means of an iterative matrix diagonalization technique. This method can provide us with the N lowest eigenvalues while at the same time being memory efficient [129]. After the diagonalization is finished, the Kohn-Sham orbitals are available and in the fourth step of the cycle a new density can be obtained by means of Equation 2.16. The cycle starts again using the new density to construct the corresponding $V_{eff}\left[n(\mathbf{r})\right]$ and $\hat{H}_{KS}$. This procedure is repeated until self-consistency is achieved. This usually means that the difference in energies or densities at the beginning and at the end of the cycle differ by less than a user-defined tolerance. In principle, such cycle could work without containing any empirical parameters. Hence the name *ab-initio* or *first-principles* given to this type of calculations. The most widely used DFT codes, e.g. Vienna ab-initio simulation package (VASP) [130, 131] or ABINIT [132], solve the Kohn-Sham equations following the cycle shown in Figure 17.

2.5 APPROXIMATIONS FOR THE EXCHANGE-CORRELATION FUNCTIONAL

If the $E_{xc}[n(\mathbf{r})]$ term would be known, solving the Kohn-Sham equations would yield the exact $n_0(\mathbf{r})$ for the interacting system. However, finding the exact expression for $E_{xc}[n(\mathbf{r})]$ would be equivalent to solve the complex-many body problem we are trying to circumvent. In practice, only approximations for $E_{xc}[n(\mathbf{r})]$ are attainable. Let us now shortly introduce the aproximations mentioned in this thesis.

2.5.1 *Local and semi-local approximations*

The local density approximation (LDA) was proposed by Kohn and Sham [128]. Its main assumption is that the spatial distribution of the charge density varies slowly in the system under study. Hence, it is possible to consider it locally equivalent to the density of an homogeneus electron gas. The local character refers to the fact that both, the exchange-correlation energy and its functional derivative with respect to the density, depend only on the density at point $\mathbf{r}$. The exchange-correlation energy $E_{xc}^{\mathrm{LDA}}[n(\mathbf{r})]$ in LDA is given by

$$E_{xc}^{\mathrm{LDA}}[n(\mathbf{r})] = \int \mathrm{d}\mathbf{r}\, n(\mathbf{r}) \epsilon_{\mathrm{xc}}^{\mathrm{hom}}[n(\mathbf{r})]\,, \tag{2.17}$$

where $\epsilon_{\mathrm{xc}}^{\mathrm{hom}}[n(\mathbf{r})]$ is the exchange-correlation energy density of an homogeneous electron gas with density $n(\mathbf{r})$. The exchange-correlation potential $V_{\mathrm{xc}}(\mathbf{r})$ can then be written as

$$V_{xc}[n(\mathbf{r})] = \frac{\delta E_{xc}[n(\mathbf{r})]}{\delta n(\mathbf{r})} = \epsilon_{xc}^{\mathrm{hom}}[n(\mathbf{r})] + n(\mathbf{r}) \frac{\delta \epsilon_{xc}^{\mathrm{hom}}[n(\mathbf{r})]}{\delta n(\mathbf{r})}. \tag{2.18}$$

The exchange contribution within this functional is known analytically from the work by Dirac on the homogeneous electron gas [133]. Furthermore, exact analytical expressions of the correlation energy for the same system are only known for low- and high-densities [134–136]. Nevertheless, intermediate-densities have been analyzed based on highly accurate quantum monte-carlo simulations [137]. The correlation used in LDA interpolates the values obtained from quantum monte-carlo while reproducing the known exact limits [138, 139].

By construction, LDA performs well for systems with slowly varying densities, i.e. systems with highly delocalized electrons like metals. However, LDA fails to describe transition metal compounds, where the electron inhomogeneity due to the open 3d shell is particularly pronounced [119, 140]. Furthermore, regarding the structures predicted by LDA, it has been found that this approximation favors overbinding. This means that LDA calculations usually result in high cohesive energies, smaller lattice constants and bond lengths compared to experiments [119, 120].

Besides introducing the LDA, Kohn and Sham [128] also suggested a first step to go beyond: a *gradient expansion approximation*. Such functional includes both the density and its gradient at each point. Since including derivatives allows the functional to "feel" the density at the surroundings of point **r**, these functionals are called semi-local. Despite being the natural step to go beyond LDA, as proposed by Kohn and Sham [128], this approximation violates the sum rules and does not bring a consistent improvement over LDA [119, 141]. The origin of these problems is that such simple expansion cannot deal with the very large gradient found in real materials [119].

The *generalized gradient approximation* (GGA) proposes to modify the behavior at large gradients in a way that guarantees that the gradient expansion does not breakdown. The exchange-correlation energy $E_{xc}^{\mathrm{GGA}}[n(\mathbf{r})]$ for the GGA is given by

$$E_{xc}^{\mathrm{GGA}}[n(\mathbf{r})] = \int \mathrm{d}\mathbf{r}\, n(\mathbf{r}) \epsilon_{\mathrm{x}}^{\mathrm{hom}}[n(\mathbf{r})]\, F_{\mathrm{xc}}(n(\mathbf{r}), \nabla n(\mathbf{r})), \tag{2.19}$$

where $\epsilon_{\mathrm{x}}^{\mathrm{hom}}[n(\mathbf{r})]$ is the exchange energy density of the homogeneous electron gas and $F_{\mathrm{xc}}(n(\mathbf{r}), \nabla n(\mathbf{r}))$ is dimensionless.

The introduction of the gradients improves the calculated lattice parameters and corrects the overbinding observed in LDA. However, the main argument in favor of the GGA approximation comes from the fact that it improves the bonding energies for solids and molecules [120]. Some of the most extensively used GGA functionals are the ones proposed by: Perdew-Wang [142, 143], Becke [144] and the Perdew-Burke-Ernzerhof (PBE) [145].

Before continuing on further types of functionals, it must be said that both, LDA and GGA, fail to describe the band-gap and generally they understimate it. This issue is known as the *band-gap problem*.

2.5.2 *LDA+U and GGA+U*

As mentioned in the previous section, local approximations for $E_{xc}[n(\mathbf{r})]$ work better for delocalized electrons and fail to describe systems in which electrons tend to be localized. This is the case of transition metal compounds and rare earth elements and compounds [119, 120]. Aiming at a correct description of these systems, Anisimov *et al.* [146] introduced the so-called LDA+U method, where an LDA calculation is combined with an additional orbital-dependent on-site repulsion interaction. Such interaction is applied via an adjustable Coulomb parameter U, inspired on the "U" interaction in Hubbard models [147, 148]. Within this method, the energies ε_i of the Kohn-Sham orbitals are given by [149]

$$\varepsilon_i^{\mathrm{LDA}+U} = \varepsilon_i^{LDA} + U\left(\frac{1}{2} - f_i\right). \tag{2.20}$$

Compared to the LDA value, the LDA+U method lowers the occupied states by $-U/2$ and raises the unoccupied ones by $U/2$. As a consequence, LDA+U "repels" less than half-filled orbitals ($f_i < 1/2$) and favors fully occupied orbitals, i.e. enhances localization of the electrons [149]. Usually this approach is used on d and f orbitals whose localized nature is not well reproduced by LDA or GGA but is (partially) recovered due to the on-site Coulomb potential in LDA+U [149]. Furthermore, due to this enhanced electron localization, the LDA+U method also improves the description of the band-gap [149]. Although it usually does not reproduce the experimental band-gap, it does deliver a better result with an affordable computational effort.

Regarding the value of the U for an specific orbital in a system, it can be obtained without adjustable parameters by means of "constrained DFT" calculations or it can be tuned to reproduced a certain experimental feature [119, 120]. A final remark on this method is that when a GGA calculation is used instead of an LDA one, we refer to it as GGA+U.

2.5.3 *Hybrid functionals*

Due to the fact that the correlation contribution in LDA and GGA is provided by very accurate quantum Monte-Carlo calculations, it can be assumed to be properly described. However, this is not the case for the exchange contribution, which is considerable underestimated. As mentioned at the beginning of this chapter, the HF method evaluates the exchange interaction accurately. Therefore, a natural path for reaching a more complete approach would be to combine the advantages of both methods. This is the motivation behind the so-called hybrid functionals, whose basic idea behind is to create an exchange-correlation energy $E_{xc}^{\text{hybrid}}[n(\mathbf{r})]$ from mixing the LDA or GGA exchange-correlation energy with a fraction of the HF exchange [119–121]. A first option to perform this mixing is to apply a global approach, which in the case of using a GGA functional would be given by

$$E_{xc}^{\text{hybrid}} = E_{xc}^{\text{GGA}} + a_{hybrid}\left(E_x^{\text{HF}} - E_x^{\text{GGA}}\right), \tag{2.21}$$

where a_{hybrid} is constant that can be fitted experimentally or estimated theoretically [129, 150, 151]. A second option to carry out the mixing is to use a range-separated method. This is the case of the screened hybrid functionals, among which the widely used HSE06 [152, 153] is found. In the case of this specific functional, the exchange-correlation energy E_{xc}^{HSE} is given by

$$E_{xc}^{\text{HSE}} = \frac{1}{4}E_x^{\text{HF,SR}}(\omega_{\text{scr}}) + \frac{3}{4}E_x^{\text{PBE,SR}}(\omega_{\text{scr}}) + E_x^{\text{PBE,LR}}(\omega_{\text{scr}}) + E_c^{\text{PBE,LR+SR}}(\omega_{\text{scr}}), \tag{2.22}$$

where ω_{scr} is the exchange screening factor which defines the range separation and its standard value for the HSE06 functional is $\omega_{scr} = 0.2$ Å^{-1}. In Equation 2.22 the superscripts SR and LR stand for short and long range contributions, respectively. In general, hybrid functionals drastically improve the description of the band-gap but they do so at a very high computational cost. Compared to local or semi-local approaches, hybrids usually are at least two orders of magnitude more expensive.

2.6 BASIS SETS AND THE CONCEPT OF PSEUDOPOTENTIALS

Once the exchange-correlation potential has been chosen and the complete problem is set, we need to select an appropriate mathematical representation (basis set) of the Kohn-Sham orbitals $\phi_i^{KS}(\mathbf{r})$ in order to solve the Kohn-Sham equations. It is certainly possible to represent them using a three-dimensional grid in real space, and then solve the Kohn-Sham equations using finite differences [120]. However, one can make use of specific features of the system under study to construct more efficient alternatives. For example, based on the atomic nature of materials, an intuitive approach would be to use localized atomic orbitals as basis set [119]. However, although they can be very efficient, they lack transferability, i.e. such basis is system dependent.

A natural basis set to deal with crystalline systems, which are the main interest of this work, arises from the fact that we need to account for their translational periodicity. Therefore, the Kohn-Sham orbitals must satisfy the Bloch theorem [154]

$$\phi_i(\mathbf{r}) = e^{i\mathbf{k}\cdot\mathbf{r}}\Xi_i(\mathbf{r}), \tag{2.23}$$

where $\Xi_i(\mathbf{r})$ is a function with the periodicity of the lattice and $\mathbf{k}$ is a vector that belongs to the first Brillouin zone. This term can be expanded using a discrete and orthonormal set of plane-waves as follows

$$\Xi_i(\mathbf{r}) = \frac{1}{\sqrt{\Omega}} \sum_{\mathbf{B}} c_{i,\mathbf{B}} e^{i\mathbf{B}\cdot\mathbf{r}}, \tag{2.24}$$

where Ω is the volume of the unit cell, $c_{i,\mathbf{B}}$ are the coefficients of the expansion and $\mathbf{B}$ are lattice vectors of the reciprocal space. Inserting Equation 2.24 into 2.23 we obtain the following expansion

$$\phi_{i,\mathbf{k}}(\mathbf{r}) = \frac{1}{\sqrt{\Omega}} \sum_{\mathbf{B}} c_{i,\mathbf{k}+\mathbf{B}} e^{i(\mathbf{k}+\mathbf{B})\cdot\mathbf{r}}. \tag{2.25}$$

This last equation shows that plane waves are a natural representation of Kohn-Sham orbitals in periodic systems, like solids. When using this basis set, the Kohn-Sham equations assume a particularly simple form given by

$$\sum_{\mathbf{B}'} \underbrace{\left[\frac{1}{2}|\mathbf{k}+\mathbf{B}|^2\delta_{\mathbf{B},\mathbf{B}'} + V_{eff}(\mathbf{B}-\mathbf{B}')\right]}_{H_{\mathbf{k}+\mathbf{B},\mathbf{k}+\mathbf{B}'}} c_{n,\mathbf{k}+\mathbf{B}'} = \varepsilon_{i,\mathbf{k}} c_{n,\mathbf{k}+\mathbf{B}}. \tag{2.26}$$

In Equation 2.26, the kinetic energy is diagonal and the Kohn-Sham effective potential is described by its Fourier transform. Solution of Equation 2.26 is carried out by diagonalizing the Hamiltonian $H_{\mathbf{k}+\mathbf{B},\mathbf{k}+\mathbf{B}'}$. The size of such matrix is determined by the dimension of the plane-wave set in expansion 2.25, which is limited to a given maximum value of the kinetic energy known as the *cutoff energy* E_{cut}. This last value satisfies the following condition

$$\frac{1}{2}|\mathbf{k}+\mathbf{B}|^2 < E_{cut}. \tag{2.27}$$

The quality of a given DFT calculation which uses plane wave as basis set, can be controlled and improved by systematically increasing the value of E_{cut}. It must be noted that the precise value of E_{cut} is case dependent and should be optimized every time a new system is studied. Furthermore, although plane waves represent a general and accurate basis set, the solution of Equation 2.26 can become an intractable problem, if the size of the basis is too large. This is the case when studying large systems and when the rapidly oscillating wave functions associated to the core electrons are included in the expansion [119, 120]. This last problem can be overcome using the so-called pseudopotentials (PPs).

PPs are based on the fact that most physical properties of solids are strongly associated to the valence electrons. Conceptually, a pseudopotential replaces the density associated with a given set of core electrons with an smoother version designed to reproduce some properties of the true core, e.g. its scattering properties and the phase shifts of the real wave function [155]. Furthermore, outside of the core regions, the pseudopotential and the real potential are identical. Thanks to this smoother description of the core electrons, the size of the plane wave basis remains manageable.

A drawback of PPs approach is that all information on the full all-electron wave function close to the cores is lost. Such information is valuable when calculating certain properties like hyperfine parameters and electric field gradients [156]. It would be ideal then to keep the information of the full wave function and at the same time maintain a low size of the basis set. This is achieved by means of the projector augmented wave (PAW) method proposed by Blöchl [157]. Within this formalism, the full many-electron wave function $\Psi(\mathbf{r})$ is decomposed in smooth auxiliary wave functions $\widetilde{\Psi}(\mathbf{r})$, by means of a transformation τ [120]. In this way, a low number of plane waves is needed to describe $\widetilde{\Psi}(\mathbf{r})$, but the

full all-electron wave function is still implicitely accounted for. Further details on the theory of PPs and PAW can be found in the books by Martin [119] and Kohanoff [120].

2.7 FORCES AND STRESS IN DFT

At this point we know that DFT allows us to obtain the ground state electronic density and as a consequence gives us access to all the properties of a given system. Among them, the possibility of calculating the forces on the nuclei of a solid stands out because, if they are known, it its possible to find the equilibrium geometry for which the forces are smaller than a certain tolerance factor.

The Hellmann-Feynman theorem [158, 159], provides the mathematical machinery to find those forces. It states that if a given Hamiltonian $\hat{H}_\lambda$ depends on the parameter λ, the variation of the energy E_λ with respect to λ is given by

$$\frac{dE_\lambda}{d\lambda} = \left\langle \Psi_\lambda | \frac{\partial \hat{H}_\lambda}{\partial \lambda} | \Psi_\lambda \right\rangle, \tag{2.28}$$

where Ψ_λ represents any normalized variational solution of the Schrödinger equation associated to $\hat{H}_\lambda$.

Let us now use this theorem to evaluate the force $\mathbf{F}_\mathrm{I}$ on nucleus I in the Kohn-Sham auxiliary system, given by

$$\mathbf{F}_\mathrm{I} = -\frac{\partial E_{KS}\left[n(\mathbf{r})\right]}{\partial \mathbf{R}_\mathrm{I}} = \left\langle \Psi_{KS} | \frac{\partial \hat{H}_{KS}}{\partial \mathbf{R}_\mathrm{I}} | \Psi_{KS} \right\rangle, \tag{2.29}$$

with $\mathbf{R}_\mathrm{I}$ being the position of the nucleus I and the Hamiltonian $\hat{H}_\lambda$ being given by Equation 2.15. Furthermore, Ψ_{KS} is the wave function described by the Slater determinat shown in Equation 2.5 but constructed with the Kohn-Sham orbitals. Thus, $\mathbf{F}_\mathrm{I}$ can be explicitly expressed as [129]

$$\mathbf{F}_\mathrm{I} = \int \mathrm{d}\mathbf{r} n(\mathbf{r}) \frac{Z_\mathrm{I}(\mathbf{R}_\mathrm{I} - \mathbf{r})}{|\mathbf{R}_\mathrm{I} - \mathbf{r}|^3} + \sum_{I \neq J} \frac{Z_\mathrm{I} Z_\mathrm{J}(\mathbf{R}_\mathrm{I} - \mathbf{R}_\mathrm{J})}{|\mathbf{R}_\mathrm{I} - \mathbf{R}_\mathrm{J}|^3}. \tag{2.30}$$

The equilibrium geometries can be then found by variating all the $\mathbf{R}_\mathrm{I}$ until the energy is a minimum and the condition

$$\|\mathbf{F}_\mathrm{I}\| < tol, \tag{2.31}$$

is satisfied for all nuclei. In this last equation, $tol \approx 0$ and it is the user-defined tolerance factor mentioned before. This factor enters the calculation as a parameter.

Closely related to the calculation of forces within DFT, the stress tensor can also be obtained using this formalism. Macroscopically, the components of the stress tensor are defined as [119]

$$\sigma_{\eta\zeta} = -\frac{1}{\Omega}\frac{\partial E_{\text{total}}}{\partial \mathrm{u}_{\eta\zeta}}, \tag{2.32}$$

where $\mathrm{u}_{\eta\zeta}$ are the components of the strain tensor, $\mathbf{u}$, and E_{total} is the total energy of the system. The quantum-mechanical theory of stress developed by Nielsen and Martin [160], allows us to calculate these stress tensor components from DFT calculations. Their formulation is rather involved and goes beyond the aim of this short introduction to the methods used in this thesis. We refer the interested reader to their original paper. In here, we only point out the direct relation of the stress tensor components, $\sigma_{\eta\zeta}$, and the forces between atoms, which can be quantified in the following way [119]

$$\sigma_{\eta\zeta} = -\frac{1}{2\Omega}\sum_{I\neq J} \mathrm{F}_{IJ,\eta}\mathrm{r}_{I,\zeta}, \tag{2.33}$$

where $\mathrm{F}_{IJ,\eta}$ is the η-component of the contribution to the force on nucleus I due to nucleus J.

3

AB-INITIO CHARACTERIZATION OF DEFECTS IN SEMICONDUCTORS

3.1 INTRODUCTION

In this chapter, we provide an overview of the methodologies used in this thesis in order to study point defects and dislocations in Cu(In,Ga)Se_2. Although we are not strictly focused on point defects, we discuss the DFT-based calculation schemes developed for them because they are already in a mature stage and serve as a smooth introduction to the case of dislocations, for which the application of DFT is not well established. Specifically, we introduce the concepts of *formation energy* and *charge transition level* as proposed for point defects and we show how to apply them when dealing with dislocations. Furthermore, in the case of point defects, we also introduce the *elastic dipole tensor*, which allows us to study the strain-driven interaction between point defects and dislocations in Cu(In,Ga)Se_2.

For detailed discussions on the ab-initio theory of point defects we refer the reader to the excellent review by Freysoldt *et al.* [27] and the books by Drabold and Streicher [161], Alkauskas *et al.* [162] and the chapter dedicated to the topic in the book by Abou-Ras *et al.* [38]. For the connection between these simulations and experiments we recommend the tutorial by Alkauskas *et al.* [163] and references therein. In the case of DFT-based simulations of dislocations, we highlight the recent review by Rodney *et al.* [164]. Furthermore, although focused on other types of simulation techniques, the book by Bulatov and Cai [165] provides a detailed account on the method we use to create the input structures for ab-initio calculations.

3.2 THE SUPERCELL APPROACH

When using plane waves to solve the Kohn-Sham equations, periodic boundary conditions must be satisfied [119]. This, together with the fact that computational power is limited, means that we must perform our simulations with a finite-size box or *supercell*, which is then repeated infinitely in all three spatial directions. The main advantages of this approach are that the perfect material is accurately described and that allows us to use all the efficient techniques derived

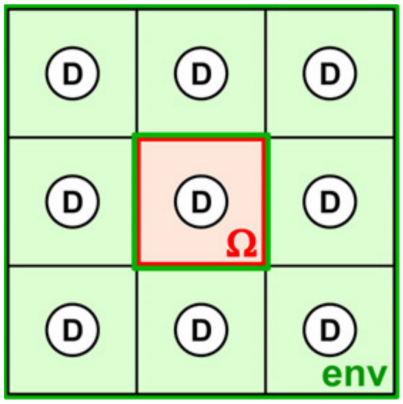

Figure 18.: Schematic of a defective supercell and its periodic images. As we can see, with this configuration, the defect D creates a periodic defect array. (Adapted and reprinted from Ref. [166] ©*IOP Publishing Ltd*)

from the quantum physics of periodic systems [161]. This means that with the supercell approach it is possible to apply the highly efficient and well tested DFT codes available for periodic solids [130–132]. Nevertheless, if a defect is inside, as shown in Figure 18, the supercell becomes the new unit cell and the system is actually a three-dimensional defect array. Such configuration results in unrealistic high defect concentrations and would induce spurious interactions between the studied defect and its periodic images.

Naturally, these interactions would be negligible at sufficiently large supercells, i.e. the *dilute limit*. However, reaching such limit would imply supercell sizes for which calculations become unfeasible [167, 168]. Therefore, the state-of-the-art approach to deal with these spurious effects, as presented by Freysoldt *et al.* [27], consists of three steps. The first step is to estimate how these effects behave as the size of the supercell increases. The second step is to minimize their influence on the calculated properties by means of adequate computational schemes. In the final third step, one should apply *a posteriori* corrections to eliminate any remaining impact of finite-size effects.

One may think that all these difficulties could be overcomed by means of using a different configuration like a *cluster* [119, 169] or by applying Green's function techniques [170–172]. However, the defect-defect interactions would still be present in those alternatives. The only difference is the mechanism from which they originate. For example, in the case of clusters one would see quantum confinement effects if the electronic states associated with the defect are not localized even for fairly large structures [27]. Therefore, the same problems would remain but we would be deprived of the advantages associated with supercell approach.

3.3 POINT DEFECTS

3.3.1 *Formation energies*

As proposed by Zhang and Northrup [173], we can use supercells to study individual defects or impurities in different charge states. Obviously, in such approach the particle number and charge conservation are not fulfilled. This means we are working in the grand-canonical ensemble where the thermodynamic description of the defect is provided by its *Gibbs free energy of formation*, $G^f[\mathrm{D}^q](\mathrm{P},\mathrm{T})$, defined as

$$G^f[\mathrm{D}^q](\mathrm{P},\mathrm{T}) = E_{\mathrm{tot}}[\mathrm{D}^q] - E_{\mathrm{tot}}[\mathrm{bulk}] + \mathrm{P}V^f[\mathrm{D}^q] - \mathrm{T}S^f[\mathrm{D}^q] - \sum_i n_i\mu_i(\mathrm{P},\mathrm{T}) + q(E_F + E_{\mathrm{VBM}}) + E^{\mathrm{tot}}_{\mathrm{corr}}, \tag{3.1}$$

where P and T are the pressure and temperature, respectively. Furthermore, $E_{\mathrm{tot}}[\mathrm{D}^q]$ is the total energy of the supercell containing defect D at charge state q, and $E_{\mathrm{tot}}[\mathrm{bulk}]$ is the total energy of an equivalent non-defective supercell. Both total energies are readily accessible from our DFT calculations. The third term in Equation 3.1 includes the *formation volume* of the defect $V^f[\mathrm{D}^q]$ and accounts for the pressure dependence of $G^f[\mathrm{D}^q](\mathrm{P},\mathrm{T})$. Analogously, the fourth term includes the *formation entropy* of the defect $S^f[\mathrm{D}^q]$ and quantifies most of the effect of temperature on $G^f[\mathrm{D}^q](\mathrm{P},\mathrm{T})$ [27].

For a defect to be formed, atoms must be added or removed from the supercell. Such process has an energetic cost which is included by means of the fifth term in Equation 3.1. In there, n_i is an integer value which indicates the number of atoms of type i that are added or removed from the supercell and $\mu_i(\mathrm{P},\mathrm{T})$ are their corresponding pressure- and temperature-dependent chemical potentials. The same analysis can be applied to the electrons added or removed to charge the defect and is accounted for in the sixth term in Equation 3.1. In this case, q indicates the number of electrons involved in the process and their chemical potential is given by the sum of the VBM energy E_{VBM} and the Fermi level E_F referenced to the VBM ($0 < E_F < E_G$). The final term of Equation 3.1 corrects all the spurious effects caused by the finite-size of the supercell and it will be discussed in detail in Section 3.3.2.

The main contribution to the free energy of the defect is called *formation energy* and is given by [27, 162]

$$E^f[\mathrm{D}^q] = E_{\mathrm{tot}}[\mathrm{D}^q] - E_{\mathrm{tot}}[\mathrm{bulk}] - \sum_i n_i\mu_i + q(E_F + E_{\mathrm{VBM}}) + E^{\mathrm{tot}}_{\mathrm{corr}}, \tag{3.2}$$

where $\mu_i(0,0)$ is refered to simply as μ_i. In reality, experimental conditions at which defects occur in a material define the relevant reservoirs. Therefore, we can

use different values of μ_i to explore various experimental conditions. Naturally, only physically sensible values must be used. In the case of solid phases the chemical potentials of the species can be expressed as

$$\mu_i = \mu_i^{el} + \Delta\mu_i, \tag{3.3}$$

where μ_i^{el} are the chemical potentials of the most stable elemental reference phase (equal to their corresponding cohesive energy) and $\Delta\mu_i$ quantifies the deviation from that value. When $\mu_i = \mu_i^{el}$, the calculations study the so-called *i*-rich conditions. Since the maximal deviations $\Delta\mu_i$ are restricted by the heat of formation of the compound under study, *i*-poor conditions can also be addresed. Moreover, information about secondary phases helps to set further specific bounds to the values of μ_i.

Once the formation energy is known, we can access one of the most important quantities that characterize defects, their equilibrium concentrations. In the dilute limit, it is given by the following Arrhenius relation [27, 162]

$$c^{eq}(\mathrm{T}) = N_{\text{sites}} \exp\left(-E^f[\mathrm{D}^q]/k_\mathrm{B}\mathrm{T}\right), \tag{3.4}$$

where N_{sites} quantifies the number of positions in the lattice (including the symmetry-equivalent ones) on which the defect can exist and k_B is the Boltzmann constant. Naturally, $E^f[\mathrm{D}^q]$ should have all finite-size effects removed such that it accurately describes the actual dilute limit.

3.3.2 *Correction schemes for the formation energies*

Let us now discuss the term $E^{\text{tot}}_{\text{corr}}$ in Equations 3.1 and 3.2. As mentioned when introducing the idea of applying supercells to study defects, spurious interactions due to the resulting periodic defect array are expected. Such interactions are of quantum-mechanical (ovelapping wave functions), elastic, magnetic and electrostatic nature. Nevertheless, in the case of charged defects, even for fairly large supercells, long-range electrostatic effects are dominant. Therefore, we will focus our discussion on how to apply corrections for such case. Before continuing, we point out that an excellent overview on the state-of-the-art correction schemes for all the effects mentioned before can be found in the review by Freysoldt *et al.* [27].

The first issue when dealing with charged defects using a supercell approach, is that an homogeneous neutralizing *jellium* background must be added in order to avoid divergences in the electrostatic energies [161, 166, 175]. Consequently, the charged defect under study interacts with its periodic images and with the *jellium* background. A second issue, illustrated in Figure 19, is that the average potentials of the charged defect calculation and that of the non-defective

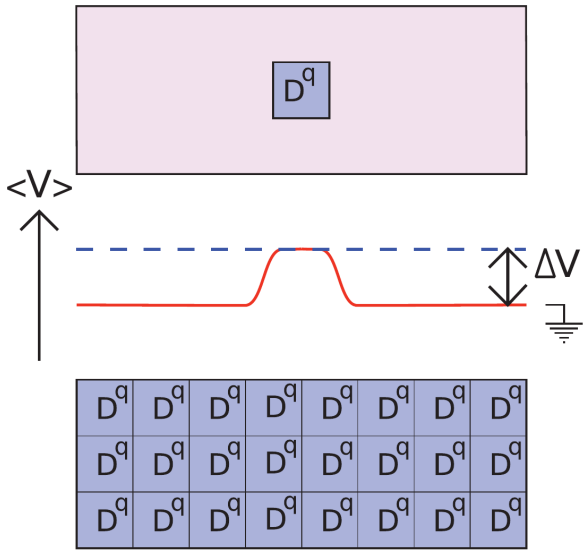

Figure 19.: Schematic of the origin and meaning of the potential alignment when using the supercell approach to study a charged defect D^q. The situation in the dilute limit is shown in the upper panel and the case of a finite-size supercell is shown in the lower panel. The average electrostatic potential is shown in the space between both figures. The solid red line corresponds to the case of the isolated defect and the dashed blue line to the supercell result. Both lines should be aligned in order to get meaningful results. (Reprinted with permission from Ref. [174], ©*American Physical Society*)

supercell need to be aligned [161, 174, 176, 177]. Having in mind these two contributions, Equation 3.2 can be re-written as

$$E^f[\mathrm{D}^q] = E_{\mathrm{tot}}[\mathrm{D}^q] - E_{\mathrm{tot}}[\mathrm{bulk}] - \sum_i n_i\mu_i + E^q_{\mathrm{corr}} + q(E_F + E_{\mathrm{VBM}}) + q\Delta V[\mathrm{D}^q], \tag{3.5}$$

where E^q_{corr} corrects the spurious interaction between the defect and its periodic images when inmersed in a *jellium* background and ΔV accounts for the needed potential aligment mentioned before. In the last couple of decades, several schemes have been proposed to deal with these undesired effects. Among them, the efforts of Makov and Payne (MP) [178], Lany and Zunger (LZ) [166, 175] and Freysoldt, Neugebauer and Van de Walle (FNV) [179, 180] stand out. The latter is the first fully ab-initio approach to calculate this correction and a recent comparative study showed that the FNV scheme gives the best performance when dealing with point defects with a very well localized charge distribution [176]. However, the same study showed that when dealing with defects with more extended but still localized charge distributions, the LZ and FNV schemes perform

equally well. Since extended but localized charge distributions is what we found for dislocations in Cu(In,Ga)Se_2 (see Part III), both methods could, in principle, be used in this thesis. Due to its flexibility and clear physical interpretation, we choose the LZ scheme. Let us now discuss the details of this scheme.

The $E^q_{\mathrm{corr-LZ}}$ used in the LZ method is closely related to the corresponding correction in the MP sheme. Therefore, let us focus first on $E^q_{\mathrm{corr-MP}}$, which has the following form for a cubic supercell

$$E^q_{\mathrm{corr-MP}} = \underbrace{\frac{q^2\alpha_{\mathrm{M}}}{2\varepsilon \mathrm{L}}}_{E_{\mathrm{MP1}}} - \underbrace{\frac{2\pi q Q}{3\varepsilon\Omega}}_{E_{\mathrm{MP2}}}, \tag{3.6}$$

where α_{M} is the Madelung constant (which can be calculated by the Ewald method [181, 182]), ε in this case refers to the macroscopic dielectric constant of the material under study, Ω and $\mathrm{L} = \sqrt[3]{\Omega}$ are the volume and linear dimension of the used supercell, respectively. In Equation 3.6, Q is the second radial moment of the localized charge distribution ρ_c and it is given by

$$Q = \int r^2 \rho_c(\mathbf{r}) \mathrm{d}\mathbf{r}. \tag{3.7}$$

The term E_{MP1} in Equation 3.6 is the screened Madelunk-like lattice energy of point charges interacting with its periodic images when inmersed in a neutralizing background. Naturally, E_{MP1} is accurate for the case of point-like charge distributions. However, such situation is not realistic in the case of real defects in a material. For this reason, MP includes the term E_{MP2} to account for the interaction between the delocalized part of the defect-induced charge distribution within the supercell and the screened point-charge potential of the periodic images [166, 175]. What is proposed in the LZ scheme is to calculate the E_{MP2} contribution from the difference between the total charge densities of the charged and neutral DFT calculations for a given defect. Following this path, Lany and Zunger [166, 175] found that for a cubic supercell

$$E_{\mathrm{MP2}} = -\frac{\pi q^2}{6\varepsilon \mathrm{L}} \left(1 - \frac{1}{\varepsilon}\right) = -E_{\mathrm{MP1}} c_{sh} \left(1 - \frac{1}{\varepsilon}\right), \tag{3.8}$$

where c_{sh} depends only on the supercell shape. Having in mind that in general $1/\varepsilon \sim 0$, the $E^q_{\mathrm{corr-LZ}}$ correction would have the following form

$$E^q_{\mathrm{corr-LZ}} = \left[1 - c_{sh}\right] E_{\mathrm{MP1}}. \tag{3.9}$$

Lany and Zunger [166] calculated the values of c_{sh} for various supercell shapes and found out that $c_{sh} = 1/3$ is generally valid, even in the case of supercells with

considerable anisotropic shape. Therefore, $E^q_{\mathrm{corr-LZ}}$ can be effectively calculated and applied as

$$E^q_{\mathrm{corr-LZ}} = \frac{2}{3} E_{\mathrm{MP1}}. \tag{3.10}$$

$E^q_{\mathrm{corr-LZ}}$ is completed with the corresponding potential alignment term in the LZ scheme given by [166, 175]

$$q\Delta V[\mathrm{D}^q] = q(V^{\mathrm{ref}}_{\mathrm{D},q} - V^{\mathrm{ref}}_{\mathrm{bulk}}), \tag{3.11}$$

where $V^{\mathrm{ref}}_{\mathrm{D},q}$ and V^{ref}_{bulk} are the reference electrostatic potentials for the defective and non-defective supercells, respectively. They are obtained by means of spherical averages of the electrostatic potential at atomic sites far away from the defect [166, 175].

3.3.3 *Charge transition levels*

As we saw in the previous section, the calculation of the formation energy of a given defect allows us to estimate its concentration in the dilute limit. Such result can be compared with experiments and is one of the main results a DFT-based defect calculation can deliver. Nevertheless, this is not the only quantity amenable available for comparison with experiments. Based on the formation energies we are also able to calculate the *charge transition levels* of a given defect. These levels determine the electronic behavior of the defect and are extremely valuable in order to correctly identify the origin of the defect signals observed in eperiments.

One could naively think that defect states formed by Kohn-Sham orbitals (henceforth called *defect states*), as obtained from the corresponding DFT-based defect calculation, can be directly associated with defect levels found in experiments. However, one must keep in mind that Kohn-Sham orbitals are artifical constructions which reproduce the ground state density of the interacting electronic system, but nothing else [27, 119, 121]. Nevertheless, total energies delivered by DFT are reliable and can be used to accurately position the thermodynamic charge transition levels $\epsilon(q/q')$ of a given defect. These charge transition levels are defined as the Fermi level for which the formation energies of charge states q and q' are equivalent [27, 38, 162] and can be calculated as

$$\epsilon(q/q') = \frac{E^{\mathrm{f}}[\mathrm{D}^q; E_{\mathrm{F}} = 0] - E^{\mathrm{f}}[\mathrm{D}^{q'}; E_{\mathrm{F}} = 0]}{q' - q}, \tag{3.12}$$

where $E^{\mathrm{f}}[\mathrm{D}^q; E_{\mathrm{F}} = 0]$ is the formation energy of the defect when E_F is at the VBM. The transition level $\epsilon(q/q')$ is also understood as the Fermi level below which the defect prefers the q charge state and above which the q' state is more

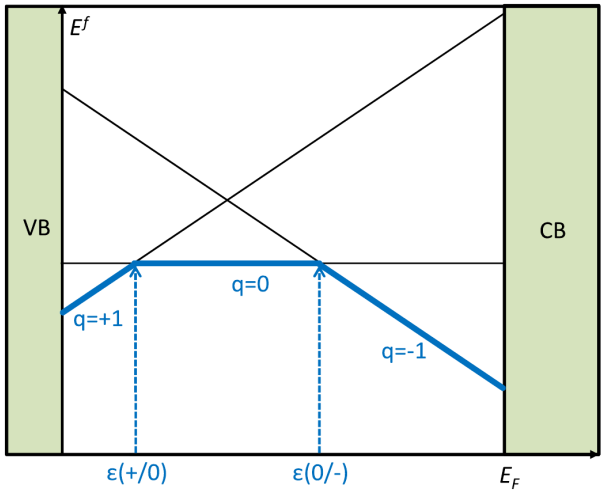

Figure 20.: Schematic of a formation energy diagram with respect to the Fermi level exhibiting two charge transition levels. Only the most favorable charge states are shown. (Reprinted with permission from Ref. [27], ©*American Physical Society*)

stable. As mentioned before, the $\epsilon(q/q')$ are relevant because they can be directly compared with experiments. Specifically, this is true when the perfomed measurement allows the defect to relax into the equilibrium configuration of its different charge states [27], e.g. in the case of deep-level transient spectroscopy (DLTS) [183, 184].

In Figure 20, we show an example of the usual $E^{\mathrm{f}}[\mathrm{D}^q]$ versus E_{F} diagrams used to depict the $\epsilon(q/q')$ in a given material. As mentioned before, if a transition level is located close to the center of the band-gap, as the examples in the figure, the $\epsilon(q/q')$ is said to be *deep*. On the contrary, a given $\epsilon(q/q')$ is called *shallow* if it is located close enough to the band edges so it can be easily thermally ionized. Furthermore, if the $\epsilon(q/q')$ levels exhibited by a defect include only positive or neutral charge states we talk about a donor defect and its charge transition are called *donor levels*. Analogously, if a given defect only exhibit negative or neutral charge states, it is refered to as acceptor defect and its $\epsilon(q/q')$ levels are called *acceptor levels*. If a defect is stable in both possitive and negative charge states, as in Figure 20, it is called *amphoteric*.

Evidently, the comparison between the $\epsilon(q/q')$ obtained from DFT-based defect calculations with experiments, is only valid if the simulation is able to correctly locate the charge transition levels within the band-gap of the material. As we discussed in the previous chapter, when using computational efficient local or semi-local exchange-correlation functionals, a DFT calculation will exhibit the well-known band-gap problem [119, 121]. Unfortunately, if our calculation is affected by this problem, the position of the $\epsilon(q/q')$ cannot be determined ac-

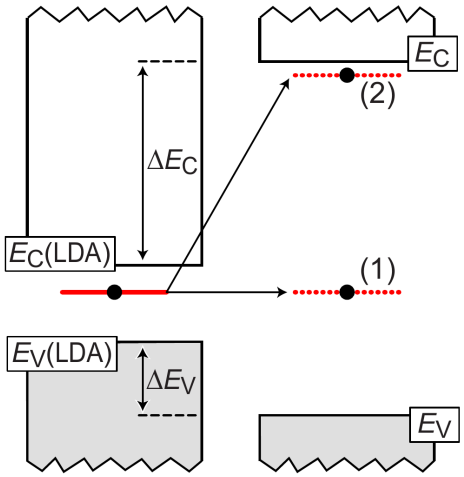

Figure 21.: Schematic of the band-gap problem influence on the determination of charge transition levels and the limitations of *a posteriori* corrections to fix the issue. On the left of the figure, a charge transtion level (marked as a red line) inside the LDA band-gap of a material is shown. On the right we can see how, once the band-gap is corrected up to its experimental value, the final position of the charge transition level cannot be uniquely determined. (Reprinted with permission from Ref. [175], ©*American Physical Society*)

curately [27, 166, 175]. This is so, even if we are able to calculate precisely the magnitude of the corrections ΔE_V and ΔE_C, which would have to be applied *a posteriori* to the VBM and CBM, respectively, in order to reproduce the experimental band-gap.

Such situation is depicted in Figure 21. In there, the result from a simple LDA calculation is shown on the left. In that case, it is found that the defect under study induces a donor level inside the wrongly described band (a solid red line in the figure). However, once ΔE_V and ΔE_C are applied, how should the position of the $\epsilon(q/q')$ change?. One possibility would be to use an internal potential reference and keep the position of $\epsilon(q/q')$ fixed with respect to that reference [27, 166, 175]. If this is done, the final position of the transition level corresponds to the one of the dashed line (1) shown on the right in Figure 21. Another possibility would be to consider that $\epsilon(q/q')$ is shallow and consequently should move together with the CBM [27, 166, 175]. In such case, its final position would be given by the dashed line (2) shown on the right in Figure 21. The question of which of the two possibilities is correct cannot be answered easily. Furthermore, these two possibilities on how to move $\epsilon(q/q')$ are not the only ones that could be applied. Therefore, using *a posteriori* corrections to the band edges and to the position of the transition levels cannot deliver conclusive results [27, 175]. The best solution for this problem is to use a calculation strategy that delivers directly

a more accurate band-gap. This is the case of hybrid functional [27, 162] or even more involved strategies, e.g. the GW approach [27, 185, 186].

3.3.4 *Elastic dipole tensor*

In general, defects induce lattice distortions on both local- and long-range scales. For the former, a description based on elasticity cannot be considered reliable as there may be large distortions in the region inmediate to the defect. In this region, an atomistic approach must be used [187], i.e. molecular dynamics, DFT or a more involved theory. In the specific case of point defects, the long-range elastic distortions can be completely described by means of the *elastic dipole tensor* (EDT) [188–195]. This tensor bridges the atomic structure of the defect with the elastic field it introduces in a material. Consequently, such mathematical entity also describes the interaction of point defects with strain or stress within linear elasticity. Due to these features, Leibfried and Breuer [190] affirmed that the EDT (which they called *double force tensor*) "is, withouth exageration, the most important concept needed in defect physics". Furthermore, used together with the elastic constants of the material under study, the EDT give us access to the $V^f[\mathrm{D}^q]$ in Equation 3.1 and to the enthalpy of formation $H^f[\mathrm{D}^q]$ of a given defect.

In order to understand the concept behind this tensor and how to calculate it, let us analyze a truncated Taylor expansion of the energy $E(n_\mathrm{D}, \mathbf{u})$ of a supercell, without entropy contributions, in terms of the strain $\mathbf{u}$ (with components $\mathrm{u}_{\eta\zeta}$) and the number of defects per supercell n_D (we will restrain our discussion to neutral defects for the moment)

$$\begin{aligned} E(n_\mathrm{D}, \mathbf{u}) = E(0,0) + \sum_{\eta\zeta} \frac{\partial E(n_\mathrm{D}, \mathbf{u})}{\partial \mathrm{u}_{\eta\zeta}}\Big|_{\mathbf{u}=0, n_\mathrm{D}=0} \mathrm{u}_{\eta\zeta} + \sum_{\eta\zeta\iota\chi} \frac{\partial^2 E(n_\mathrm{D}, \mathbf{u})}{\partial \mathrm{u}_{\eta\zeta} \partial \mathrm{u}_{\iota\chi}}\Big|_{\mathbf{u}=0, n_\mathrm{D}=0} \mathrm{u}_{\eta\zeta}\mathrm{u}_{\iota\chi} \\ + \frac{\partial E(n_\mathrm{D}, \mathbf{u})}{\partial n_\mathrm{D}}\Big|_{\mathbf{u}=0, n_\mathrm{D}=0} n_\mathrm{D} + \sum_{\eta\zeta} \frac{\partial^2 E(n_\mathrm{D}, \mathbf{u})}{\partial \mathrm{u}_{\eta\zeta} \partial n_\mathrm{D}}\Big|_{\mathbf{u}=0, n_\mathrm{D}=0} \mathrm{u}_{\eta\zeta} n_\mathrm{D}, \end{aligned} \tag{3.13}$$

where $E(0,0)$ is the is the energy of a corresponding non-defective and unstrained supercell. This equation can be rewritten based on the previously presented definitions of the stress and the formation energy of a defect. Additionally, the second derivative in the third term in Equation 3.13 is equal to the compo-

nents $C_{\eta\zeta\iota\chi}$ of the *elastic stiffness tensor* of the material. Therefore, Equation 3.13 could be better expressed as

$$E(n_{\mathrm{D}},\mathbf{u}) = E(0,0) + \sum_{\eta\zeta} \underbrace{\sigma_{\eta\zeta}\Big|_{\mathbf{u}=0,n_{\mathrm{D}}=0}}_{=0} \mathrm{u}_{\eta\zeta} + \sum_{\eta\zeta\iota\chi} C_{\eta\zeta\iota\chi}\mathrm{u}_{\eta\zeta}\mathrm{u}_{\iota\chi} + E^f[\mathrm{D}]n_{\mathrm{D}} + \sum_{\eta\zeta} \frac{\partial^2 E(n_{\mathrm{D}},\mathbf{u})}{\partial \mathrm{u}_{\eta\zeta}\partial n_{\mathrm{D}}}\Big|_{\mathbf{u}=0,n_{\mathrm{D}}=0} \mathrm{u}_{\eta\zeta} n_{\mathrm{D}}. \tag{3.14}$$

As mentioned before, the EDT describes how a given point defect interacts with strain. This means that it describes how its formation energy varies in the presence of the strain field $\mathbf{u}$. As a consequence, if we derivate Equation 3.14 with respect to n_{D} and obtain the strain dependent formation energy of defect D, we should find out the form of the EDT

$$\frac{\partial E(n_{\mathrm{D}},\mathbf{u})}{\partial n_{\mathrm{D}}} = E^f[\mathrm{D}](\mathbf{u}) = E^f[\mathrm{D}] + \sum_{\eta\zeta} \frac{\partial^2 E(n_{\mathrm{D}},\mathbf{u})}{\partial \mathrm{u}_{\eta\zeta}\partial n_{\mathrm{D}}}\Big|_{\mathbf{u}=0,n_{\mathrm{D}}=0} \mathrm{u}_{\eta\zeta}. \tag{3.15}$$

Evidently, all changes in the formation energy of the defect which are caused by strain are contained in the last term of this equation. Thus, the components $G_{\eta\zeta}[\mathrm{D}]$ of the EDT are given by

$$G_{\eta\zeta}[\mathrm{D}] = -\frac{\partial^2 E(n_{\mathrm{D}},\mathbf{u})}{\partial \mathrm{u}_{\eta\zeta}\partial n_{\mathrm{D}}}\Big|_{\mathbf{u}=0,n_{\mathrm{D}}=0} = -\frac{\partial E^f[\mathrm{D}]}{\partial \mathrm{u}_{\eta\zeta}} = -\frac{\partial \sigma_{\eta\zeta}}{\partial n_{\mathrm{D}}}. \tag{3.16}$$

Therefore, Equation 3.15 can be rewritten including the EDT as

$$E^f[\mathrm{D}^q](\mathbf{u}) = E^f[\mathrm{D}^q] - \sum_{\eta\zeta} G_{\eta\zeta}[\mathrm{D}^q]\mathrm{u}_{\eta\zeta}, \tag{3.17}$$

where the existence of charged defects in now taken into account. This last equation implies that the formation energy of a given defect inmersed in a strain field would only decrease if the elements of the EDT and the components of the strain have the same sign. This means that a defect with positive EDT components (dilation center) would prefer to be formed in a positively strained region of the material. Analogously, if the defect has negative EDT components (compression center), its formation energy would decrease in a negatively strained region. When calculating the strength of the interaction between a point defect and a strain field, the EDT formalism has the advantage that it inherently captures the symmetry of the defect [190, 191, 193, 195].

The scheme to calculate the components of the EDT is implicit in Equation 3.18. We simply calculate the difference in stress caused by the presence of one defect D^q on a given supercell without allowing the supercell volume or shape to change (*strain control*) as

$$G_{\eta\zeta}[D^q] = -\frac{\partial \sigma_{\eta\zeta}}{\partial n_D} = -\frac{(\sigma_{\eta\zeta}[D^q] - \sigma_{\eta\zeta}[0])}{n_D} = -\Omega\Delta\sigma_{\eta\zeta}[D^q], \tag{3.18}$$

where $\sigma_{\eta\zeta}[0]$ and $\sigma_{\eta\zeta}[D^q]$ are the stress components in the non-defective and defective supercell, respectively. As in the case of defect formation energies or charge transition levels, the calculated $G_{\eta\zeta}[D^q]$ are hampered by the finite size of the supercell. Therefore, if it is not computationally cumbersome, the EDT components should be obtained for different supercell sizes and its value for the dilute limit could be obtained by means of an extrapolation [196]. As we will see in the next section, when studying charged defects one should correct for the spurious stress arising from the electrostatic interaction with its periodic images and with the neutralizing background, and from the potential missalignement.

3.3.5 *Correction schemes for the EDT*

As proven by Bruneval and Crocombette [197], when studying the formation volumes of charged defects, there is an spurious pressure associated with the correction terms E^q_{corr} and $q\Delta V(D^q)$. For the former, Bruneval and Crocombette [197] found out that this pressure is given by

$$P^q_{\text{corr}} = \frac{q^2\alpha_M}{6\varepsilon\Omega^{4/3}}. \tag{3.19}$$

This means that there must be a correction to the diagonal terms of the stress tensor $\sigma_{\eta\eta,corr}[D^q]$ with the following magnitude (notice the positive sign)

$$\sigma_{\eta\eta,corr}[D^q] = \frac{q^2\alpha_M}{18\varepsilon\Omega^{4/3}}. \tag{3.20}$$

For the correction of the spurious stress related to $q\Delta V(D^q)$ we follow the elegant solution given by Goyal *et al.* [198]. Their proposal is shown in Figure 22 and is based on the difference between the volumes for which the formation energy of the defect under study is minimal, when the potential aligment correction is included and when is not. In the example shown in the figure, these volumes are shown as dashed lines. Once the difference is known, one can use the elastic constants and estimate the spurious pressure and stress associated to the $q\Delta V(D^q)$ correction.

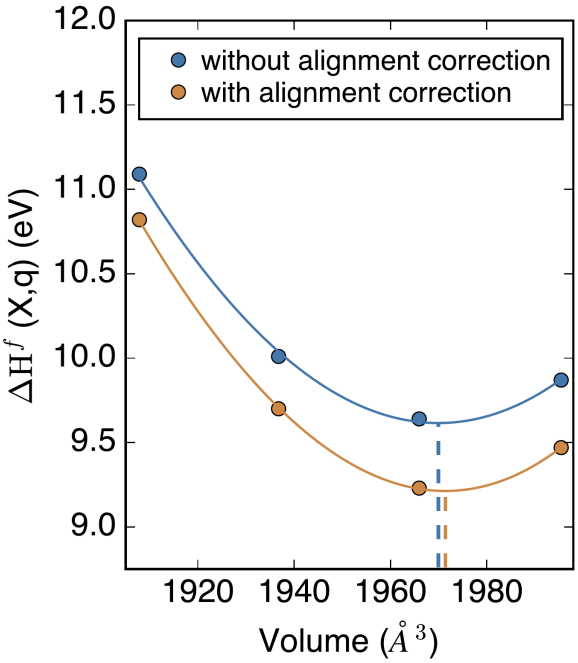

Figure 22.: Procedure followed to calculate the stress correction associated with the potential aligment $q\Delta V(D^q)$. The calculation is based on the difference between the volumes for which the enthalpy of formation of a given defect is minimal, shown as dashed lines, with and without the potential alignment correction. (From Ref. [198])

We must highlight that in a recent study, Bruneval *et al.* [199] proved that, as in the case of the potential, the stress is ill defined in charged supercells. They tested several DFT codes and found that most of them completely fail to account for this situation. However, they reported that the stresses obtained using VASP [130, 131] when studying a charged defect are qualitatively correct when compared with an accurate result from model-solid theory. Since we use this simulation package for our simulations, our EDT are essentially correct but can only be used to draw qualitative conclusions.

3.4 DISLOCATIONS

3.4.1 *Periodic boundary conditions and dislocations*

Our aim in this thesis is to accurately describe the structural and electronic properties of dislocations in Cu(In,Ga)Se_2 and its parent compounds. To achive such goal we use DFT and a supercell approach. Therefore, periodic boundary conditions must be satisfied and, in the case of dislocations, this implies that using

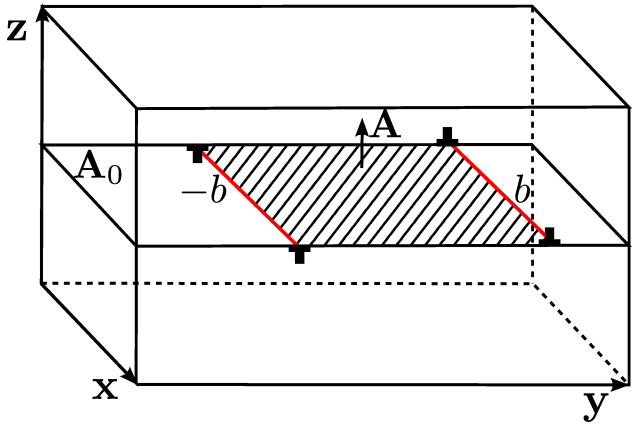

Figure 23.: Schematic of the dislocation dipole configuration used to satisfy periodic boundary conditions. Red lines mark the position of the dislocations. (This figure was first published in Ref. [201])

supercells we cannot study single dislocations withouth introducing undesired surfaces in the simulation [165, 200]. The only way to overcome this predicament is to use arrays of dislocations inside the supercell [165, 200], i.e. dipoles or quadrupoles. Naturally, this means that supercells needed to accurately study dislocations are much larger than the ones required for point defects. However, dislocations dipoles and quadrupoles have the advantage that they help to cancel out the elastic interaction with periodic images [165, 200]. Let us focus now on the details of the dipole configuration, which is the dislocation array used throughout this thesis.

A schematic of a supercell containing a dislocation dipole is shown in Figure 23. Such configuration is formed by two coplanar dislocations with antiparallel Burgers vectors, located in the midplane of the supercell. If these two dislocations recombine, we would end up with a non-defective supercell. Keeping this in mind, we can see that the formation of the dislocation dipole can be understood as a nucleation of a dislocation pair in the center of a non-defective supercell. After created, the dislocations move in opposite directions until the distance between them is equal to half the length of the supercell in the y direction. It is known that such movement would induce a plastic strain $\mathbf{u}^p$ given by (see Section B.2.2 for details)

$$\mathbf{u}^p = \frac{1}{2\Omega}(\mathbf{b} \otimes \mathbf{A} + \mathbf{A} \otimes \mathbf{b}), \tag{3.21}$$

where $\mathbf{A}$ is the vector perpendicular to the plane that contains the dipole. This last equation is a generalized form of Equation B.7. The scheme to eliminate this unwanted strain is to apply an elastic strain equal to $\mathbf{u}^{el} = -\mathbf{u}^p$ to the supercell.

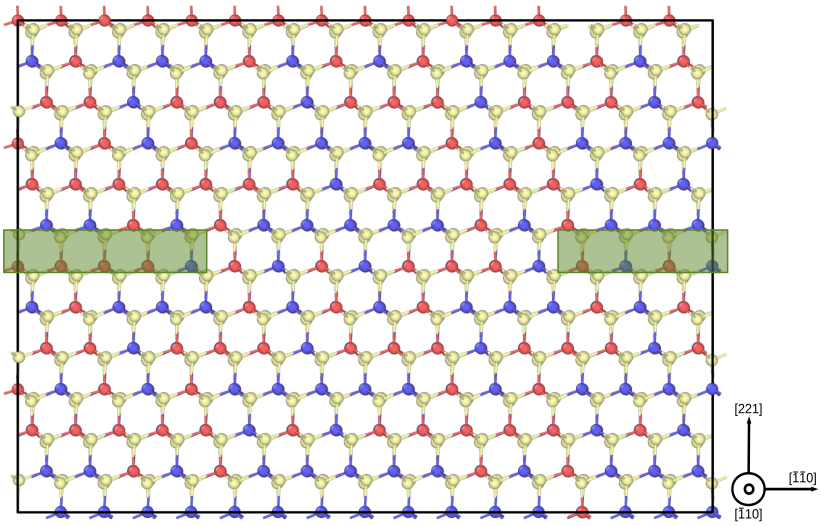

Figure 24.: Schematic of the first step towards the creation of edge dislocation dipoles without introducing plastic strain, i.e. the atoms in the green shaded areas are eliminated. The structure shown in the figure corresponds to $CuInSe_2$ and copper, indium and selenium are shown as red, blue and yellow spheres, respectively.

In the specific case of edge dislocations, we can construct a supercell containing a dipole without introducing the plastic strain mentioned before [165]. In this way, one avoids the supercell deformation associated to the elastic strain needed to eliminate the spurious strain given in Equation 3.21. The initial step of the scheme to achive this is depicted in Figure 24. In there, we show a $CuInSe_2$ supercell along with two green shaded regions. If we sequentially eliminate the atoms inside these regions, compress the supercell in the [221] direction by $1/12[221]$ and relax the atomic positions, we would end up with a dipole of pure edge character Frank partials. This last scheme is the one we use to create the supercell studied in Chapter 4.

One further consequence of the dipole configuration is that if the studied dislocation type has an edge component, the dipole will contain one α-core and on β-core. This fact has deep influence on the meaning of formation energies and charge transition levels of dislocations as obtained from supercell calculations. Such issue will be explored in the next section.

3.4.2 *Formation energies, charge transition levels and electronic structure*

The formalism developed to calculate formation energies and transition levels in the case of point defects, can be extended to the case of dislocations dipoles or quadrupoles. However, as we will see in this section, formation energies of

individual dislocations cannot be accessed and a clear picture of their electronic properties is only accesible after *a posteriori* analyses are carried out. Since we use the dislocation dipoles throughout this thesis, the forthcoming discussion is focused on the formalism and methods used for that configuration.

In such case, the formation energy given in Equation 3.5 can be rewritten as

$$E^f_{\text{dip}}[\text{D}^q] = E_{\text{tot}}[\text{D}^q] - E_{\text{tot}}[\text{bulk}] - \sum_i n_i\mu_i + E^q_{\text{corr}} + q(E_F + E_{\text{VBM}}) + q\Delta V(\text{D}^q), \tag{3.22}$$

where $E^f_{\text{dip}}[\text{D}^q]$ is the formation energy of a given dislocation dipole D in charge state q. The rest of the terms are equal to the ones described in Section 3.3.1 and 3.3.2. We stress the fact that this formation energy is given for a complete dipole. Therefore, if the cores composing the dipole are different, as it is the case when studying dislocation with an edge character [101, 165], the corresponding formation energy for individual dislocations cannot be obtained from DFT-based calculations, i.e. DFT is a total energy method. Only in the case of screw dislocations, for which the dipole is composed with two equal dislocation cores, we could divide $E^f_{\text{dip}}[\text{D}^q]$ by two and obtain the single dislocation formation energy.

Furthermore, contrary to the case of point defects, the $E^f_{\text{dip}}[\text{D}^q]$ cannot be used to estimate dislocations concentrations or densities. This is so because dislocation formation is not thermodynamically driven but they occur as growth accidents or due to strain relief [99, 100, 202]. However, its relevance lies on the fact that $E^f_{\text{dip}}[\text{D}^q]$ reveals which dislocation type is relatively more energetically favorable. Nevertheless, we emphasize that the total strain energy of a dislocation is dependent on the volume of the supercell [99, 100]. Therefore, comparing $E^f_{\text{dip}}[\text{D}^q]$ is valid as long as calculations are performed on equivalent supercells.

In the case of charge transition levels $\epsilon(q/q')$ for dislocation dipoles, based on Equation 3.12 we can use the following expression

$$\epsilon(q/q') = \frac{E^{\text{f}}_{\text{dip}}[\text{D}^q; E_{\text{F}} = 0] - E^{\text{f}}_{\text{dip}}[\text{D}^{q'}; E_{\text{F}} = 0]}{q' - q}, \tag{3.23}$$

where $E^{\text{f}}_{\text{dip}}[\text{D}^q; E_{\text{F}} = 0]$ is the value given by Equation 3.22 when E_F is at the VBM. As in the case of point defects, the $\epsilon(q/q')$ calculated for dislocation dipoles is amenable for comparison with experiments and can be interpreted as the Fermi level below which the dipole prefers the q charge state and above which the q' state is more stable. However, analogous to the case of formation energies discussed before, if the dislocation type under study has an edge character, finding out if a given $\epsilon(q/q')$ is associated to the α-core or to the β-core composing the dipole is not straightforward.

To circumvent this problem we use a concept developed by Richard Bader [203]. He proposed to estimate the surface through which the charge density gradient in molecule or solid has zero flux. The volume inside that surface is associated to the spatial region of influence of the individual atoms in the system and is called *Bader volume*. If we integrate the charge density inside the Bader volume, we will end up with the charge associated with each atom in the solid. This is the so-called *Bader charge*. After we calculate $\epsilon(q/q')$ for the dislocation dipoles of interest, we can analyze the difference in Bader charges between the relevant charge states. In this way we can conclude where are the extra electrons or holes localized and which of the two dislocation cores inside the supercell is the electrically active one for that given $\epsilon(q/q')$. Furthermore, combining this approach with an electronic structure analysis results in a very powerful tool, as we will see in Part III of this thesis. Specifically, we are able to calculate both *global* and *local density of states* (DOS and LDOS, respectively). The latter implies adding up the atomic resolved DOS for a given spatial region and allows us to access the electronic structure of individual cores inside the supercell.

A final and general issue regarding the study of electronic properties of dislocation cores using DFT-based calculations, refers to the band-gap problem. As we discussed in Section 3.3.3, in the case of point defects this problem can be overcomed by means of the very succesful hybrid functionals or even more involved theories. However, when studying dislocations the extremely large supercells needed make it impossible to use such advanced methods. Therefore, we need to find an alternative valid for both, $CuInSe_2$ and $CuGaSe_2$, which are the focus of this thesis.

When using LDA for these materials, the calculated band-gap (-0.4eV in the case of $CuInSe_2$, i.e. valence and conduction bands are overlapping by 0.40 eV) is underestimated due to the incorrectly described repulsive interaction between the Cu *d*-orbitals and Se *p*-obitals. This repulsion pushes the antibonding $p-d$ valence band states to higher energies [204]. One viable way to correct this is to apply the LDA+U approach as described in Section 2.5.2 to the Cu *d*-orbitals. This reduces the repulsion and lowers the VBM. For both, $CuInSe_2$ and $CuGaSe_2$, a physically sensible parameter is $U_d(Cu) = 6eV$, which correctly positions the Cu *d*-like valence band resonances according to photoemission experiments [205, 206]. However, with this method the band-gap problem is not fully solved, i.e. it predicts a band-gap of 0.12eV for the $CuInSe_2$, which is still far away from its experimental value (1.04eV).

A first proposal to overcome this limitation is to fit U parameters for different orbitals in a given compound such that the band-gap is reproduced [207]. However, such solution implies forcing an unphysical localization to *s* and *p*-like orbitals, which are otherwise delocalized [27]. On the other hand, although the physically driven LDA+U method with $U_d(Cu) = 6eV$ only corrects the band-gap error partially, its predicted charge transition levels can be extrapolated by the physically justified scheme proposed by Janotti *et al*. [208]. Their

approach is based on the fact that defect states are a mixture of valence-band and conduction-band states. Therefore, the extent to which charge transition levels change when going from LDA to LDA+U, depends on their relative valence-band and conduction-band character. The first step for using this method is to calculate the transition level $\epsilon(q/q')$ with both LDA and LDA+U, and then apply the following extrapolation

$$\epsilon(q/q') = \epsilon(q/q')^{\mathrm{LDA+U}} + \frac{\Delta\epsilon}{\Delta E_{\mathrm{G}}}(E_{\mathrm{G}}^{\mathrm{expt}} - E_{\mathrm{G}}^{\mathrm{LDA+U}}), \tag{3.24}$$

with

$$\frac{\Delta\epsilon}{\Delta E_{\mathrm{G}}} = \frac{\epsilon(q/q')^{\mathrm{LDA+U}} - \epsilon(q/q')^{\mathrm{LDA}}}{E_{\mathrm{G}}^{\mathrm{LDA+U}} - E_{\mathrm{G}}^{\mathrm{LDA}}}, \tag{3.25}$$

where, $E_{\mathrm{G}}^{\mathrm{LDA}}$, $E_{\mathrm{G}}^{\mathrm{LDA+U}}$ and $E_{\mathrm{G}}^{\mathrm{expt}}$ are the band-gaps given by LDA, LDA+U and obtained by experiments, respectively. The term $\frac{\Delta\epsilon}{\Delta E_{\mathrm{G}}}$ is the rate of change in the charge transition level with respect to the change in the band-gap. As seen in Equation 3.25, this coefficient depends on $\epsilon(q/q')^{\mathrm{LDA+U}}$ and $\epsilon(q/q')^{\mathrm{LDA}}$, which are the charge transition levels predicted with LDA and LDA+U, respectively. Henceforth, this last method will be refered to as LDA/LDA+U extrapolation method. In the next chapter we will evaluate its performance and we will show that it is suitable to calculate the $\epsilon(q/q')$ of dislocation dipoles in $CuInSe_2$ and $CuGaSe_2$.

3.4.3 *Correction schemes for the formation energies*

The correction terms in Equation 3.22 are calculated using the LZ scheme as presented in Section 3.3.2. Although our supercell has a fairly anisotropic shape, Lany and Zunger [166] found that their approach is generally valid, even for such cases. Naturally, the magnitude of E_{MP1} is not the one given in Equation 3.6, which is valid only for cubic supercells. We calculated its value by means of a direct method and with the help of the general utility lattice program (GULP) [209, 210]. Regarding the potential aligment, we apply the formalism as presented in Equation 3.11. Nevertheless, in our case the reference electrostatic potentials for the defective and non-defective supercells were obtained by means of cylindrical rather than spherical averages of the electrostatic potential at atomic sites far away from the dislocations.

The validity of this approach is based on the fact that, even though dislocations are extended one-dimensional defects, electrons and holes involved in the $\epsilon(q/q')$ of dislocation dipoles in $CuInSe_2$ and $CuGaSe_2$ are relatively well localized in specific bonds (see Part III). Therefore, charged dislocations in these materials can be understood as one-dimensional arrays of charged point defects rather than continuous charge distributions. This result, together with the fact that for

the dimension of our supercell along the direction of the dislocation we use the shortest possible value, allows us to use a correction scheme which is designed originally for point defects. We choose the LZ scheme since, as mentioned before, it has a high performance when dealing with defects with more extended but still localized charge distributions [176]. Therefore, we expect it to work reasonably well for the systems we are interested in.

3.4.4 *Interaction with point defects*

The interaction between dislocations and point defects can have an elastic and, if both defects are charged, an electrostatic nature. For the former, within the limits of linear elasticity, we can use Equation 3.17 to estimate how the formation energy of a given defect changes when inmersed in the strain field of a given dislocation. Such strain field can be obtained directly from the equations provided by linear eleasticity theory [99, 100, 202, 211, 212]. In the case of a screw dislocation whose line direction coincides with the z direction, its induced strain is given by

$$\mathrm{u}_{xx} = \mathrm{u}_{yy} = \mathrm{u}_{zz} = \mathrm{u}_{xy} = 0, \tag{3.26}$$

$$\mathrm{u}_{xz} = \frac{\|\mathbf{b}\|}{2\pi} \frac{y}{x^2 + y^2}, \tag{3.27}$$

$$\mathrm{u}_{yz} = -\frac{\|\mathbf{b}\|}{2\pi} \frac{x}{x^2 + y^2}, \tag{3.28}$$

where b is the norm of the Burgers vector. For an edge dislocation oriented in the same direction, we have the following set of equations to describe its strain field

$$\mathrm{u}_{zz} = \mathrm{u}_{xz} = \mathrm{u}_{yz} = 0, \tag{3.29}$$

$$\mathrm{u}_{xx} = \frac{\|\mathbf{b}\| y}{2\pi} \frac{S y^2 + (2\lambda + 3S) x^2}{(\lambda + 2S)(x^2 + y^2)^2}, \tag{3.30}$$

$$\mathrm{u}_{yy} = -\frac{\|\mathbf{b}\| y}{2\pi} \frac{(2\lambda + S) x^2 - S y^2}{(\lambda + 2S)(x^2 + y^2)^2}, \tag{3.31}$$

where S is the shear modulus of the material and λ is the other Lamé constant. In Part III of this thesis we use this approach to study the elastic contribution to the interaction between defects and dislocations. As mentioned before, this method is limited to the range of validity of linear elasticity theory and is therefore valid outside of the core of the dislocation. Nevertheless, it can deliver qualitative insights valuable in order to explain segregation tendencies observed in experiments as we will show in Part III of this thesis. A final remark to make

on the elastic interactions is that, although out of the reach of this thesis, a further way to have more realistic simulations would be to obtain the strain fields induced by a given dislocation from molecular dynamics studies of extremely large structures. However, to do so it is mandatory to have an available interatomic potential. Unfortunately, this is not the case for $CuInSe_2$ and $CuGaSe_2$.

Regarding electrostatic interactions between charged point and line defects, we cannot study them with a simple and elegant approach like the one we just explained for the elastic interaction. Such drawback arises from the fact that within DFT calculations we cannot force the system to distribute the charges in the correct fashion. Therefore, when several defects that prefer to be charged are inside a supercell, such calculations are not able to deliver unambiguous results for definite individual charge states. This is the reason why in Part III for the case of charged perfect dislocations, we intentionally focused on the segregation of neutral species and did not addressed the case of charged intrinsic point defects, despite the fundamental role they play in the properties of $Cu(In,Ga)Se_2$-based devices. A more detailed discussion on this issue can be found in the Outlook of this thesis.

3.5 TECHNICAL DETAILS OF THE CALCULATIONS

3.5.1 *Bulk properties: why using the LDA+U for relaxations?*

It is well known that hybrid functionals greatly improve the description of the bulk properties of $CuInSe_2$ and $CuGaSe_2$. It would be ideal to use such functional to study dislocations in these materials. However, as stated before, their high computational cost makes them unfeasible to study the extremely large supercells needed to simulate dislocations. For the electronic properties we will use the LDA/LDA+U extrapolation method presented in Chapter 3 and tested in Section 3.5.3 of this chapter. However, besides electronic properties, we are also focused on the structural features of dislocations in $CuInSe_2$ and $CuGaSe_2$. Therefore, we need to clarify which of the available options represent the best choice for that matter.

To answer this question we used LDA, LDA+U and GGA functionals to calculate the structural parameters of both $CuInSe_2$ and $CuGaSe_2$. Results for the lattice constants a, c, the c/a ratio, the internal displacement parameter u and bulk modulus B of these materials are shown in Table 1. For completeness, in Table 1 we also report the corresponding band-gaps. All these properties were calculated using the 16-atom tetragonal unit cell and a k-point grid of 8x8x4 for all local and semi-local functionals. For the hybrid we use a k-grid of 4x4x2 instead and a exchange-screening parameter of $\omega = 0.13$ Å^{-1}. Calculations are performed using the software VASP [130, 131].

		Parameter				
		E_G (eV)	a (Å)	c/a (Å)	u (Å)	B (GPa)
Expt.	$CuInSe_2$	1.04 [23]	5.814 [23]	2.001	0.2258 [213]	54 [214], 72 [215]
	$CuGaSe_2$	1.68 [23]	5.614 [23]	1.964	0.250 [216]	71 [217]
LDA	$CuInSe_2$	-0.4	5.718	2.012	-0.85	69.86
	$CuGaSe_2$	0.25	5.523	1.990	0.2403	72.45
LDA $+ U$	$CuInSe_2$	0.12	5.710	2.008	0.2146	68.21
	$CuGaSe_2$	0.7	5.519	1.983	0.2410	70.61
GGA	$CuInSe_2$	0.01	5.885	2.012	0.2178	55.8
	$CuGaSe_2$	0.02	5.684	1.985	0.2438	59.3
Hybrid	$CuInSe_2$	1.07	5.839	2.013	0.2259	57.9
	$CuGaSe_2$	1.68	5.650	1.965	0.2508	66.7

Table 1.: The band gaps E_{gap}, lattice parameter a, c/a ratio, internal displacement parameter u and the bulk modulus B calculated using different exchange-correlation functionals and the corresponding values obtained from experiments (Expt.).

As we can see from the results reported in the table, the GGA cannot describe the B of these materials. Therefore, it would not be expected to produce reliable results if used to study dislocations or the EDT of relevant point defects. It is interesting to notice that even the highly accurate hybrid functional cannot achieve a correct description of the bulk modulus. On the other, both LDA and LDA+U do a great job reproducing the experimental value for B. Furthermore, both functionals do an equally satisfactory job at describing the structure. If the structural relaxations carried out in this thesis were only focused on neutral systems, we could use either ot the two functionals. However, this is not the case and charged systems are a central issue on this thesis. We choose LDA+U over LDA because it does a better job at describing the band-gap of $CuInSe_2$ and $CuGaSe_2$. Consequently, LDA+U improves the description of both the charge carrier localization and the local relaxations around charged defects in these materials.

3.5.2 *Supercell creation and characteristics*

All supercells used in this thesis have the same coordinate axes given by $x = [\bar{1}10]$, $x = [\bar{1}\bar{1}0]$ and $z = [221]$. Thus, the xy-planes correspond to the $\{112\}$ planes in the chalcopyrite structure. Since these planes are the preferred slip planes for dislocations in $CuInSe_2$ and $CuGaSe_2$, supercells with these axes allows us to simulate all relevant dislocation types we are interested in.

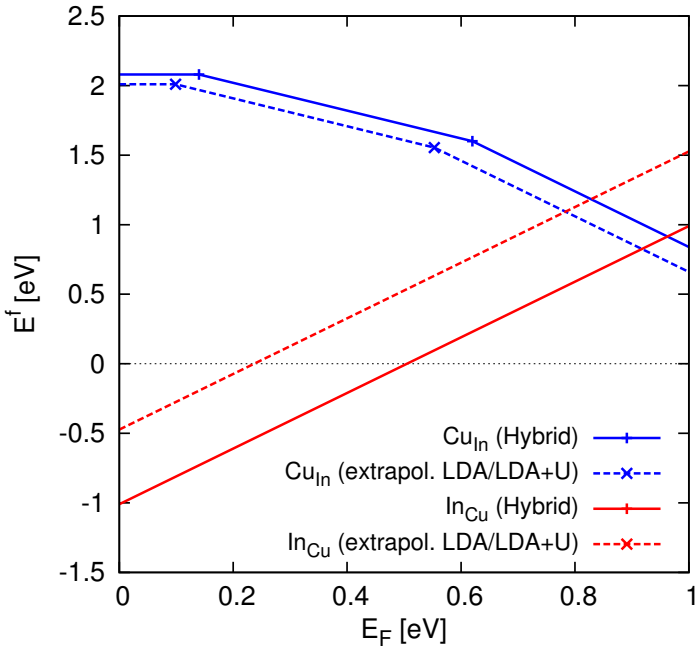

Figure 25.: Comparison between the charge transition levels of Cu_{In} and In_{Cu} antisites in $CuInSe_2$ obtained using an screened-exchange hybrid potential reported in Ref.[5] versus the LDA/LDA+U extrapolation method proposed in Ref.208. (This figure was first published in Ref. [201])

The supercell used to study the Frank loops in Cu(In,Ga)Se_2 was created following the ideas on how to create a dipole of edge dislocations presented in Section 3.4.1. The resulting structure has 800 atoms and it will be studied in detail in Chapter 4.

On the other hand, the supercell used to investigate perfect screw and 60°-mixed dislocations in $CuInSe_2$ and $CuGaSe_2$ was created by applying the theoretical strain distribution associated with each dislocation type to an otherwise perfect structure. In this case it was necessary to apply the elastic strain correction described in Section 3.4.1.

3.5.3 *Validity of the LDA/LDA+U extrapolation method*

In order to check the accuracy of the LDA/LDA+U extrapolation method for defects in $CuInSe_2$ and $CuGaSe_2$, we compare the charge transition levels it predicts with the values obtained with a screened-exchange hybrid potential. As we have stated before, the latter has been proven to be a reliable tool to study such systems [5]. We carry out such comparison for the cation-antisites, Cu_{In} and In_{Cu} in $CuInSe_2$, whose $\epsilon(q/q')$ are uncorrectly described when using (semi)local ap-

proximations [3, 205]. These calculations were performed for a supercell with 64 atoms. The calculated formation energies are shown in Fig. 25. In there it is possible to see that the positions of charge transition levels of these antisites are correctly predicted by the extrapolation method when compared to the hybrid potential calculations.

3.5.4 *Setup of calculations*

In the following chapters, DFT-based calculations are carried out for dislocations and the EDT of point defects in $CuInSe_2$ and $CuGaSe_2$. All DFT calculations presented in this thesis were conducted using the software VASP [130, 131] and the PAW method. Visualization of structures was done with the open visualization tool (OVITO) [218] and the visualization for electronic and structural analysis (VESTA) software [219]. Further technical details of these calculations are summarized below. In the case of dislocations:

- A converged plane-wave energy cutoff of 350 eV was used for all dislocation studies.
- Supercells constructed as explained in Section 3.5.2 were used.
- For relaxations, we use the LDA+U functional and k-grids with a single k-point (Γ) were employed.
- For the calculation of energies we use a 4x1x2 Γ-centered k-grids. Obtained formation energies and charge transition levels were found to differ by few meV when compared to the ones obtained when a 4x2x2 grid was used instead.
- Smooth DOS and LDOS were calculated using a 4x2x2 Γ-centered k-grids and using the LDA+U functional.
- Ionic relaxation is conducted until the Hellmann-Feynman forces are below 0.05 eV/Å.

On the other hand, for the calculation of the EDT of relevant point defects:

- All EDT calculations are performed using the LDA+U functional.
- A converged plane-wave energy cutoff of 550 eV was used for all EDT calculations. Such high cutoof was used in this case due to the slow convergence of stress calculations with DFT.
- Two quasi-cubic supercells of different size were used in order to estimate finite-size effects on the value of the EDT. The first one was the 2x2x1 supercell of the tetragonal 16-atom chalcopyrite unit cell and with 64 atoms.

The second one was the 4x4x2 supercell of the same unit cell and with 512 atoms.

- Γ-centered k-grids were used for both supercell sizes. For the 64-atoms cell we use a 4x4x4 grid and for the 512-atoms configuration we used a 2x2x2 grid.
- Ionic relaxation is conducted until the Hellmann-Feynman forces are below 0.002 eV/Å for supercells of 64 atoms and below 0.005 eV/Å for supercells of 512 atoms.

Part III

DISLOCATIONS IN $CuInSe_2$, $CuGaSe_2$ AND $Cu(In,Ga)Se_2$

This part of the thesis deals with the structural and electronic properties of of dislocations in $CuInSe_2$, $CuGaSe_2$ and $Cu(In,Ga)Se_2$ by means of DFT-based calculations. We start by characterizing a Frank dislocation loop in $Cu(In,Ga)Se_2$. We then discuss the relation of these loops to the efficiency-boost effect of the Cu-rich stage in state-of-the-art growth methods for $Cu(In,Ga)Se_2$-based thin-film solar cells. Afterwards, we focus on the stoichiometric configurations of the experimentally observed and theoretically possible perfect dislocations in $CuInSe_2$ and $CuGaSe_2$. Based on these results, we confirm that the electrical activity of the cores is caused by the presence of cation-cation or anion-anion bonds. Based on these results for its parent compounds, it is possible to draw conclusions on the properties of most perfect dislocations in $Cu(In,Ga)Se_2$. However, for the glide $60°$-mixed dislocation this is not straightforward. We address this issue by exploring the segregation tendency and effect of gallium in the surrounding of this structure. Finally, we focus on the segregation of sodium in the surroundings of all active dislocation cores in $CuInSe_2$ and $CuGaSe_2$. Such analysis allows us to explain the origin and effect of the experimentally observed accumulation of sodium at dislocations in $Cu(In,Ga)Se_2$.

4

FRANK PARTIALS IN $Cu(In,Ga)Se_2$

The results in this chapter were first published in Ref. [112]. Experimental results presented in this chapter were obtained by Ekin Simsek-Sanli and are reprinted with her permission.

4.1 INTRODUCTION

The three-stage coevaporation technique [46], including a Cu-rich stage, with ([Cu]/([In] +[Ga]) >1), is known to lead to $Cu(In,Ga)Se_2$ thin-films with high efficiencies and to a reduction of planar defects (PDs) [50, 115]. Highly symmetric PDs, like lamellar twin boundaries and stacking faults, are present in growth-finished $Cu(In,Ga)Se_2$ layers and they have been found not to substantially affect the electrical properties of the photovoltaic absorber [85]. Therefore, the beneficial effect of the PDs reduction should be associated to the disappearance of irregular PDs that do introduce noticeable changes in the DOS relative to the bulk [50].

In order to shed some light on this puzzle, in this chapter we use ab-initio calculations to investigate the structural and electronic properties of a specific type of irregular defect, namely a Frank dislocation loop, which was observed in a sample whose growth process was interrupted and did not go through the Cu-rich stage and has not being characterized until now.

4.2 EXPERIMENTAL SETUP

The study presented in this chapter was carried out in close collaboration with experimental partners within the Helmholtz Virtual Institute HVI-520 "Microstructure Control for Thin-Film Solar Cells". In this section we describe shortly the fabrication process of the sample where the Frank loop was observed and the setup our collaborators used for the measurements.

Let us start with the way the investigated $Cu(In,Ga)Se_2$ absorber layer was deposited: a growth-interrupted three-stage coevaporation process. In the first

stage of such process, In and Ga were deposited sequentially under Se atmosphere at 330°C. This resulted in an In-Se/Ga-Se stack. In the second stage, the substrate temperature was increased to 430°C. The process continued with Cu deposition under Se atmosphere. Our collaborators intentionally interrupted the three-stage process during this second stage, before reaching the Cu-rich composition, in order to obtain high defect concentrations [220, 221]. Up to the point where the process is interrupted, the sample was grown like a fully working solar cell.

The setup of their microscopy analysis is as follows: cross-sectional TEM lamellae from the Cu(In,Ga)Se_2 (CIGSe) thin films were prepared with a Zeiss Crossbeam 1540XB focused ion beam (FIB) machine using the lift-out method [222, 223]. Structural analysis with atomic resolution was performed using high-resolution scanning TEM (HR-STEM) and electron energy-loss spectroscopy (EELS) [224], providing insights into the atomic arrangements in and around the dislocation cores. A Cs-corrected Nion UltraSTEM 100, equipped with a cold field emission gun (CFEG), was operated at 100 kV acceleration voltage for the HR-STEM investigations [225]. The microscope is equipped with a Gatan Enfina spectrometer for the EELS spectrum imaging, i.e., the acquisition of a three-dimensional data cube with both, special and spectral information about the selected region. A dispersion of 1 eV/channel was used to cover an energy-loss range from 315 to 1655 eV, allowing for the simultaneous elemental mapping of the Cu-$L_{2,3}$, In-$M_{4,5}$, Ga-$L_{2,3}$, and Se-$L_{2,3}$ edges.

4.3 STRUCTURAL PROPERTIES

Figure 26a shows a high-angle annular dark-field (HAADF) image recorded along the $[1\bar{1}0]$ zone axis, in which an extended defect is present. In this projection, the stacking sequence of Se columns along the <221> direction is ...ABCABC... In the same figure, it is possible to detect a region with a slightly different stacking between two yellow boxes: ...ABC**BA**BC... There is an additional B plane, which is further complemented by an A plane. Interestingly, this extrinsic stacking fault terminates within the yellow boxes drawn in the same figure. This termination is only possible due to the presence of partial dislocations separating the faulted regions from the perfect crystal [100].

The partial dislocations shown in Figure 26a have a Burgers vector $\mathbf{b} = \mp 1/6\langle 221 \rangle$, which indicates that this is an extrinsic Frank partial dislocation as discussed in Section 1.3.2. Furthermore, similar to the case of silicon [226] and based on its sessile nature and what has been found for planar defects in $CuInSe_2$ occurring on low energy facet planes[108], it can be concluded that this is a grown-in defect and not the result of mechanical strain relaxation.

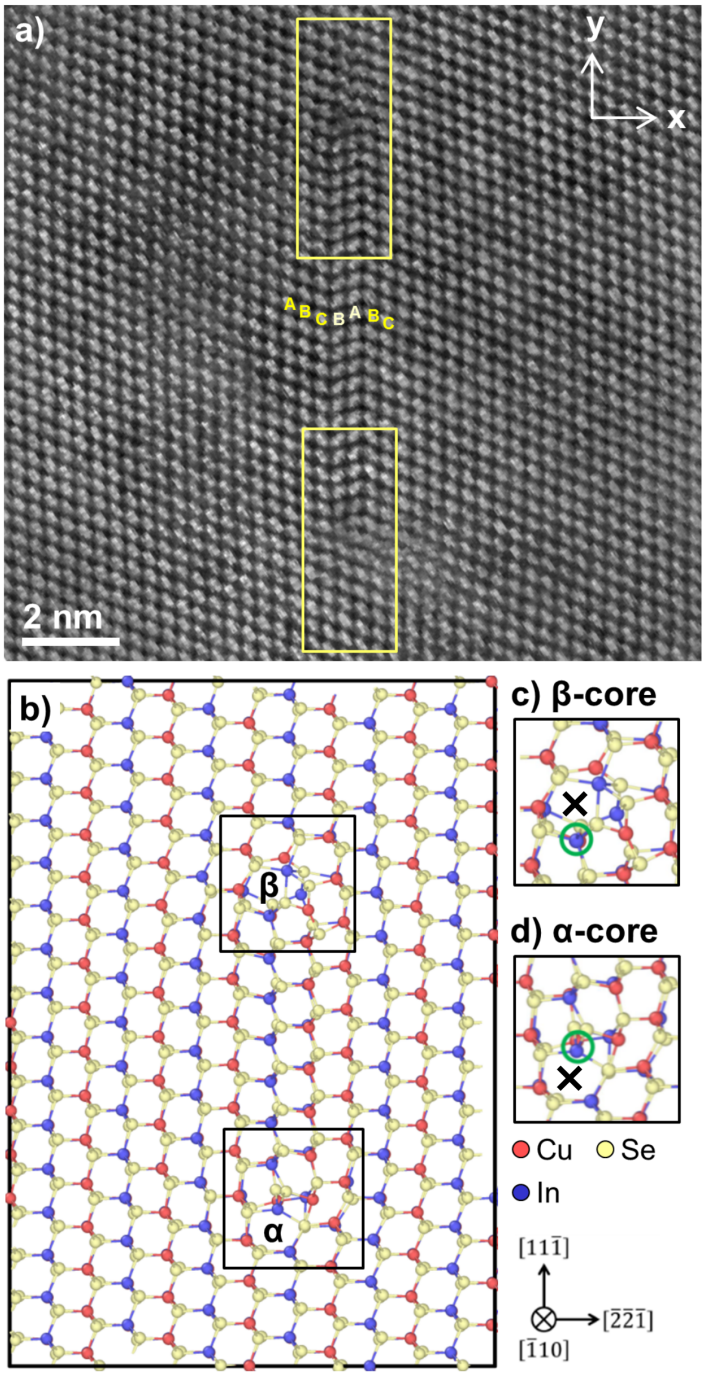

Figure 26.: HAADF image of the positive Frank partial dislocations associated with an extrinsic stacking fault (a). In there, two yellow boxes indicate the top and bottom parts of the stacking fault including partial dislocation cores (β-core in the upper box and α-core in the bottom one). Relaxed structure of an extrinsic Frank loop in $CuInSe_2$ obtained with DFT. Complete supercell showing the simulated loop(b), the β-core (c) and the α-core (d) .

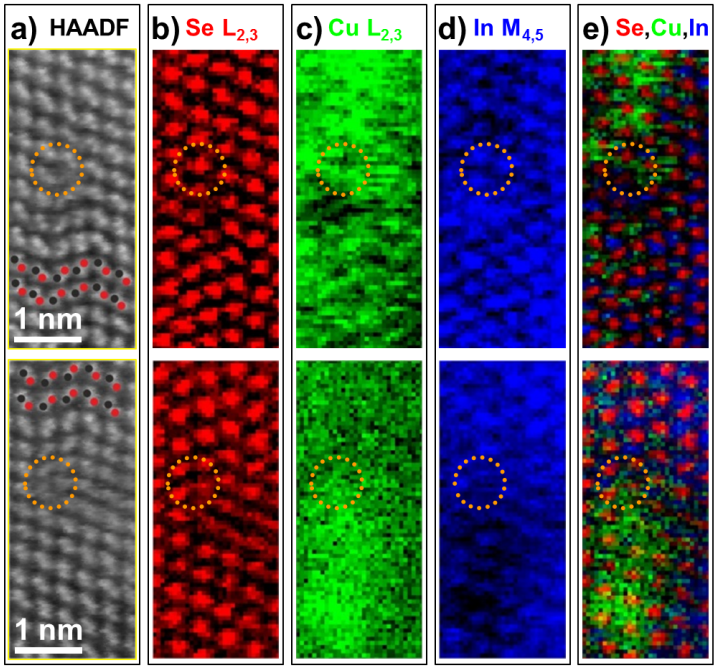

Figure 27.: Two simultaneously acquired HAADF images from the areas indicated by yellow boxes on Figure 26 show the association of the stacking fault and the Frank loop (β-core in the upper panels and α-core in the bottom ones) (a). In there, dislocation cores are indicated by orange circles. The corresponding Se-$L_{2,3}$, Cu-$L_{2,3}$ and In-$M_{4,5}$ elemental distribution maps are shown in red, green, and blue colors in Figures (b-d). Finally, the red-green-blue composite map is a color-coded superposition of the individual elemental maps (e).

In order to study the properties of this Frank loop by means of DFT calculations, we use the supercell creation method described in Section 3.5.2 for the specific case of edge dislocations. As the observed defect was localized in the Ga-poor region of the sample, the simulations were carried out for a pure $CuInSe_2$ structure. The used supercell allows us to study a slice of an extrinsic Frank loop, and its relaxed configuration can be seen in Figure 26b. We found out that all atoms in this structure are fully coordinated, and no dangling bonds are seen. Due to the symmetry of the chalcopyrite structure of $CuInSe_2$, any transversal cut of a stoichiometric Frank loop in this material will contain an α-core (Figure 26c) and a β-core (Figure 26d), and the extrinsic stacking fault between them. One great advantage of using the dipole configuration is that this symmetry constraint is inherently included.

The two regions indicated by the yellow boxes in Figure 26a were also analyzed by means of EELS, with the HAADF intensity distributions acquired simultaneously with the spectrum images. In this $[1\bar{1}0]$ projection shown in Figure 27a,

closely spaced Se and alternating In/Ga and Cu columns are visualized as an inset with red (Se) and black (Cu and In/Ga) balls. Se, Cu and In elemental distribution maps were extracted from the acquired EEL spectra and are shown in Figures 27b-d in red, green and blue, respectively (the intensities were normalized to range from 0 to 1 for simplicity and should therefore not be taken as a quantitative indication of the local chemical composition). Figure 27e shows a composite red-green-blue (RGB) image for visual conciseness. Note, that no Ga map is presented since, as mentioned above, this dislocation loop was localized in the Ga-poor region of the sample. This made the extraction of the low intensity Ga-$L_{2,3}$ edge, which also overlaps with the Cu-$L_{2,3}$ edge, not reliable. The positions of the In and Se columns fit well to the HAADF image atomic column positions. The stacking fault exhibits a polarity inversion, as depicted in the ball models superimposed on the HAADF images. More importantly, Cu-rich clouds were found outside of both cores coinciding with a lower In signal intensity. Directly at the dislocation cores, however, the α-core shows a considerable excess of Cu, while the β-core exhibits only a slight increase in the Cu signal compared to the bulk material. Furthermore, immediately below the cores and to the side of the stacking fault, a subtle drop in Cu signal is seen to coincide with a small increase in In.

4.4 ORIGIN OF THE OBSERVED CHEMICAL CHANGES INSIDE AND AROUND THE CORES

In this section we aim at resolving the origin of the atomic rearrangements seen in the experiments. To do so we can divide the problem in two regions: inside and outside the cores. For the former, our approach is to use an extension of the formation energy of point defects given in Equation 3.5. We name such extension as *relative formation energy*, $E_{\mathrm{RFE}}[\mathrm{D}^q]$, and is given by

$$E_{\mathrm{RFE}}[\mathrm{D}^q] \quad = \quad \Delta E_{\mathrm{def}} + \sum_i n_i \mu_i + E^q_{\mathrm{corr}} + q(E_{\mathrm{F}} + E_{\mathrm{VBM}}) + q\Delta V[\mathrm{D}^q]. \quad (4.1)$$

Here ΔE_{def} is the calculated energy difference between the supercell containing a non-stoichiometric Frank loop with a given point defect D with charge q located at one of the cores and the stoichiometric Frank loop supercell. The rest of the terms in this equation are equivalent to the ones previously defined. The $E_{\mathrm{RFE}}[\mathrm{D}^q]$ allows us to calculate the tendency of a given point defect to segregate inside the Frank partial cores. Non-stoichiometric Frank loop supercells were constructed by creating relevant point defects in the positions indicated by green circles in both Figure 26c and 26d in the case of the Cu vacancy and antisite defects (Cu_{In} and In_{Cu}), while the *X*'s mark the position chosen for Cu interstitials. Defect complexes with copper vacancies were not included in our analysis

since previous calculations have shown that formation of such complexes does not occur in thermodynamic equilibrium, i.e. their formation energies are higher than the ones of the individual point defects [5]. The validity of using the calculated $E_{\mathrm{RFE}}[\mathrm{D}^q]$ to draw conclusions on the chemical changes observed in the experiments, comes from the fact that a time interval of several days passed between the growth of the analyzed sample and its experimental study. Therefore, it is expected that the sample as observed under the microscope has reached thermodynamic equilibrium.

The $E_{\mathrm{RFE}}[\mathrm{D}^q]$ of various defect types in the α-core and β-core are shown in Figure 28a and 28b, respectively. The chemical potential for Cu was chosen to mimic the experimental Cu-poor conditions $\Delta\mu_{\mathrm{Cu}} = -0.4\mathrm{eV}$. Although the In chemical potential was varied between the limiting values $-1.68\mathrm{eV} \leq \Delta^{-}_{\mathrm{In}} \leq -1.0\mathrm{eV}$ of the stability region of the chalcopyrite phase for $\Delta\mu_{\mathrm{Cu}} = -0.4\mathrm{eV}$ (see Ref. [5] for details), our analysis is focused on the case where $\Delta\mu_{\mathrm{In}} \simeq -1.0\mathrm{eV}$ in which the system is close to the experimental conditions. In addition, we assume a Fermi level position close to the VBM. Relative formation energies of charged defects are presented as colored bands reflecting the range of possible Fermi levels ($0\,\mathrm{eV} \leq \mathrm{E_F} \leq 0.25\mathrm{eV}$).

In the cation-containing α-core, Figure 28a, the neutral and charged $\mathrm{Cu_{In}}$ antisites exhibit negative formation energies, which means that this defect would occur spontaneously and that the α-core has a tendency to be decorated by excess Cu. Within the relevant range of Fermi energies, the neutral antisite is the most stable configuration. Thus, the Cu-rich dislocation core has no excess charge. Furthermore, the $\mathrm{In_{Cu}}$ antisite is likely to form only when $\mathrm{E_F}$ is extremely close to the VBM, i.e. for such Fermi level the $\mathrm{In_{Cu}}$ antisite has a very low or even negative $E_{\mathrm{RFE}}[\mathrm{D}^q]$. Since these thermodynamic conditions do not occur in the real absorber, we can conclude that the decoration of the α-core by neutral $\mathrm{Cu^0_{In}}$ is the main reason for the considerable Cu accumulation at the α-core observed in experiments. For the Se-containing β-core, Figure 28b, all defect structures exhibit positive formation energies when $\Delta\mu_{\mathrm{In}} \simeq -1.0\mathrm{eV}$, which is the reason why compositional changes observed experimentally inside this core are less marked compared to its α counterpart. The presence of neutral $\mathrm{Cu^0_{In}}$ antisite and some Cu interstitials explains the slight Cu increase found in this structure. Therefore, the experimentally observed behavior of Cu at the dislocation cores, Figure 27, is in full agreement with our theoretical results.

Now let us focus on the nature and origin of the Cu clouds detected around the cores (Figure 27). The absence of dangling bonds in the relaxed stoichiometric structures and the resulting absence of localized charges rules out electrostatic interaction, which is in contrast to the case of full dislocations reported by Dietrich *et al.* [13]. The non-symmetric distribution of the Cu clouds around the dislocations also provides a hint that these cannot be due to electrostatic potentials, which would imply only a radial dependence of Cu distribution.

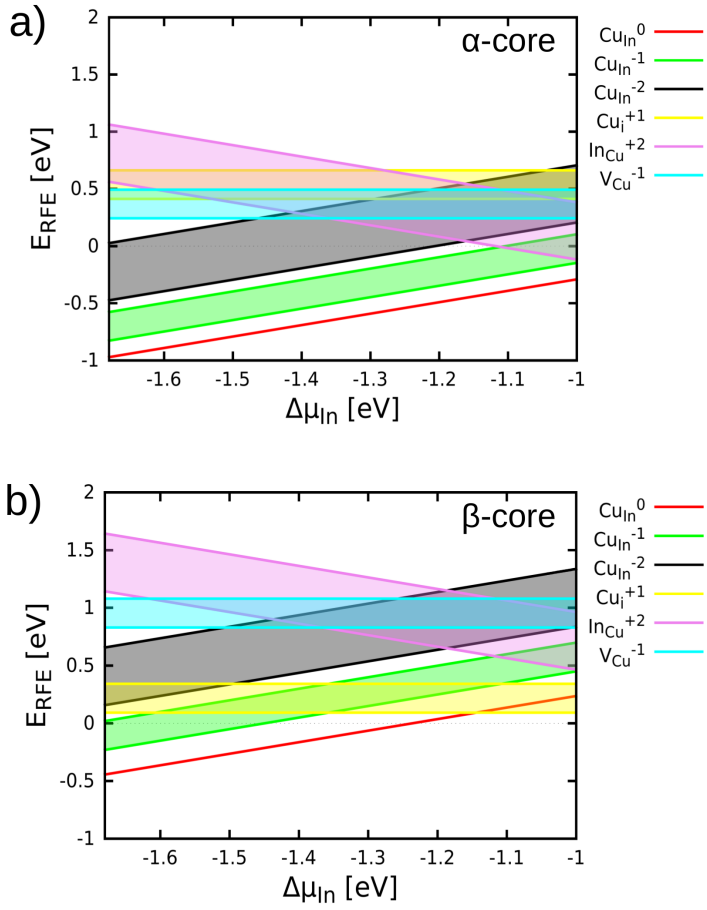

Figure 28.: Relative formation energies of point defects inside the (a) α and (b) β-cores of the Frank loop. The chemical potentials for Cu and In were chosen to mimic the experimental Cu-poor conditions and charged defects are presented as bands rather than lines to show also their values when 0eV $\leq E_F \leq$ 0.25eV.

The other possible driving force for such atomic redistribution around the cores is strain, which would explain the non-symmetric feature of the Cu-clouds. To test this hypothesis we start by studying the strain distributions by means of geometrical phase analysis (GPA) [227], which allow us to visualize the compressive and tensile strain fields associated with the dislocation cores. The main x and y axes, chosen for the strain analysis, are presented on the HAADF image in Figure 26a. We point out that the x component in the experiment corresponds to the z component of the simulated supercell. This does not change the results, but must be kept in mind. Figures 29a and 29b show the corresponding components, u_{xx} and u_{yy}, of the strain tensor superimposed to the same HAADF image (with a 90° rotation to the left) to correlate visually the measured strain values to the exact atomic positions. The color bar indicates a change in strain

from +5% tensile to -5% compressive for both the u_{xx} and u_{yy} components. The atoms at the stacking fault, especially those near the dislocation cores, experience compressive strain. At the sides of the stacking fault, the effect is inverted, and atoms experience tensile strain. At the stacking fault, the atomic columns are displaced horizontally from their positions, larger distances away from the dislocation cores along the x direction. It results in larger strain fields as is shown in the u_{xx} map. In contrast, the vertical displacement is rather localized close to the dislocation core in the y direction.

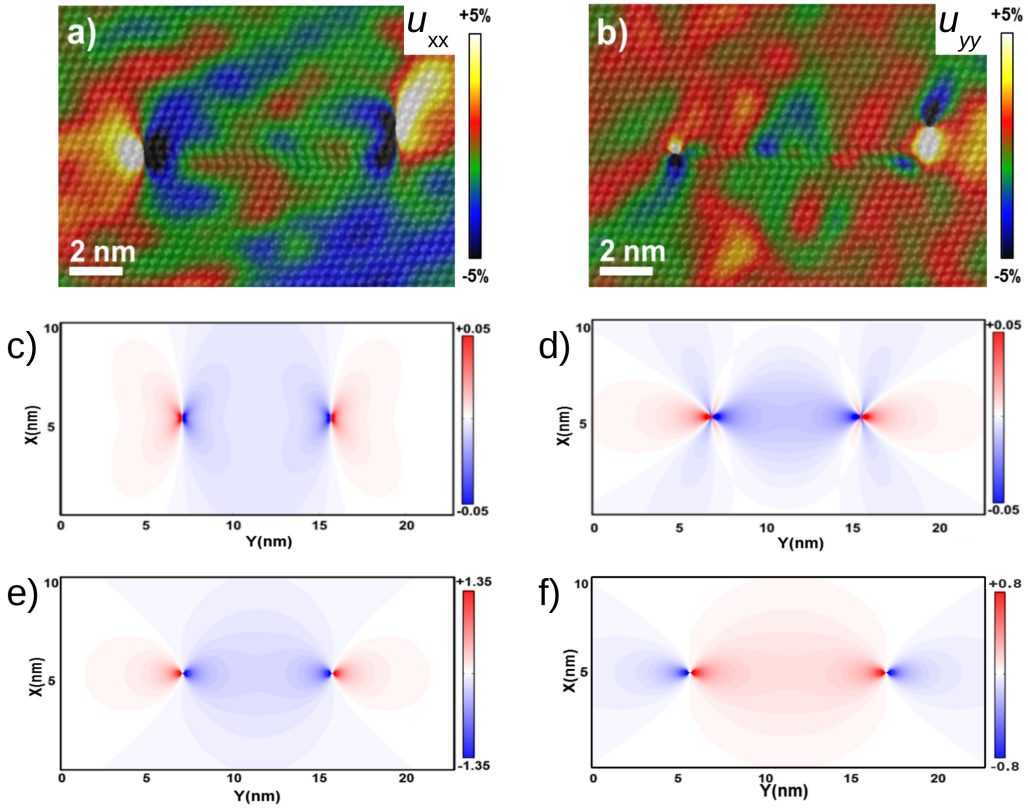

Figure 29.: The HAADF image shown in Figure 26 is superimposed with u_{xx} (a) and u_{yy} (b) strain components extracted by GPA. Strain fields for an extrinsic Frank loop as predicted from linear elasticity solutions, u_{xx} (c) and u_{yy} (d). Finally, the term $\sum_{\eta\zeta} u_{\eta\zeta} G_{\eta\zeta}$ term in eV for the Cu_{In}^{-2} (e) and In_{Cu}^{+2} (f) antisites.

For comparison we calculated the strain field components for a pair of Frank partial dislocations, u_{xx} and u_{yy} presented in Equations 3.29, from linear elasticity [99, 100, 202, 211, 212]. As we can see in Figure 29, similarities in the positioning of the tensile and compressive regions between theoretical and experimental results provides evidence that the defect studied with HR-STEM is

indeed an extrinsic Frank loop (Since linear elastic results are divergent, very close to the core we bound the results to a maximum of ±5%).

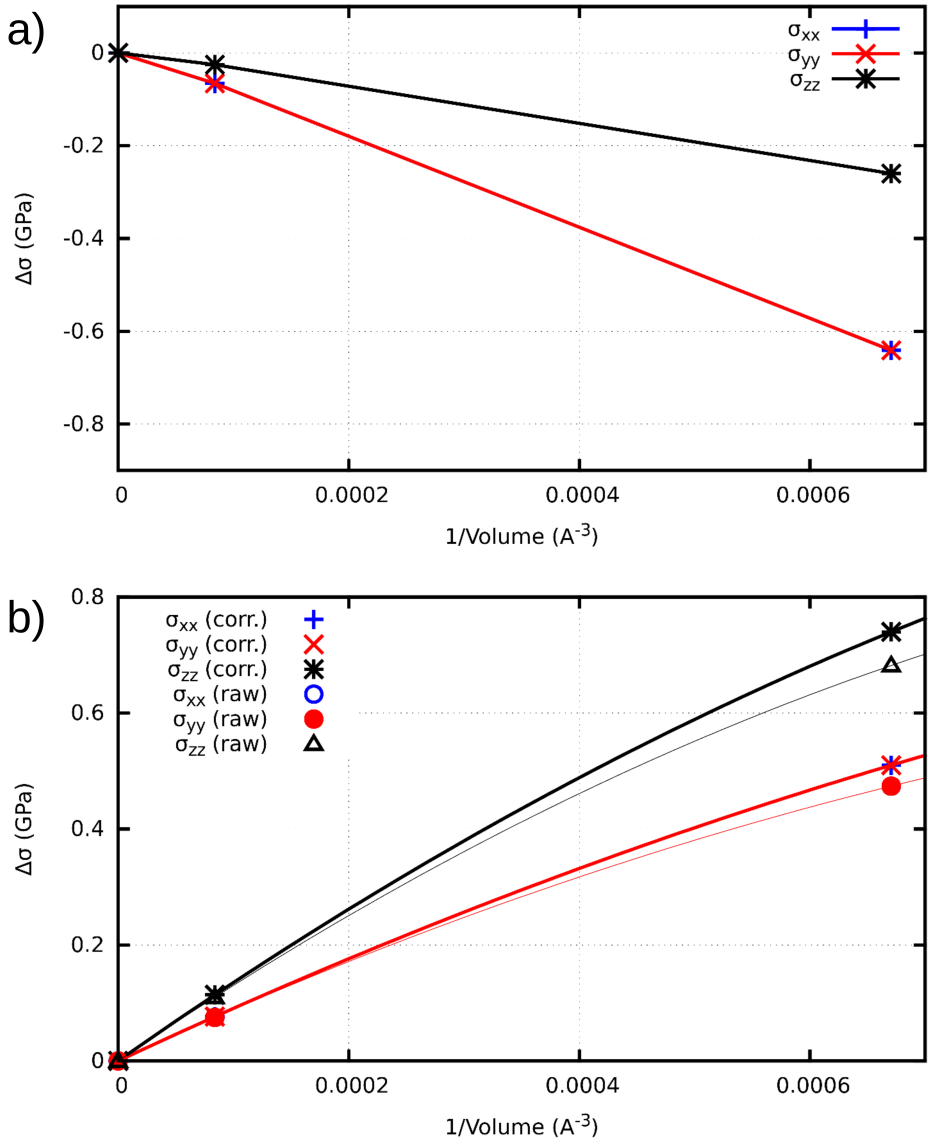

Figure 30.: Stress induced in a $CuInSe_2$ supercell containing a V_{Cu} with respect to the inverse of the supercell volume for the (a) neutral and (b) charged states. In the latter, we show the raw data obtained directly from the DFT calculations and the corrected values following the precepts introduced in Section 3.3.5.

As we can see when comparing Figures 29a-d with the elemental distribution maps shown in Figures 27, there is a clear correlation between the strain around

the Frank partials and the chemical changes observed in their surroundings. In order to reveal whether strain is the actual cause for such changes, we analyzed the mechanical coupling of this strain field to the defect thermodynamics To do so we apply the EDT formalism introduced in Section 3.3.4, specifically Equation 3.17. We have calculated the EDT of the most relevant point defects for their possible charge states as reported by Pohl and Albe [5]. In order to estimate the values of the EDT we follow the calculation scheme and corrections introduced in Sections 3.3.4 and 3.3.5 and we use the calculation setup described in Section 3.5.4. As explained in those sections, the first step is to estimate the EDT in the dilute limit. We perform such analysis in terms of the induced stress in the supercell rather than in the actual values of the EDT components. The advantage of this approach is that we know that in the dilute limite the stress induced by any defect should be zero. Therefore, this strategy provides us with one extra data point to perform the interpolation needed to estimate the actual values of the EDT components and allow us to avoid calculations for extremely large supercells. Clearly, the dilute limit value of the EDT components corresponds to the coefficient of the first order term of such interpolation. In Figure 30 we show the obtained results for the case of the V_{Cu} in $CuInSe_2$ in neutral and singly charged state. Although we know this defect is a shallow acceptor and prefers to be charged with one extra electron for all values of the E_F, analyzing its neutral version allow us to better understand the obtained results. Furthermore, we point out that our findings for V_{Cu} are general to all point defects studied.

As expected, the induced stress in the case of the neutral defect shown in Figure 30(a) behaves linearly with respect to the inverse of the volume. On the other hand, analogous to the case of the formation energy, the induced stress for the case of the charged vacancy shown in Figure 30(b), exhibits a slower convergence and a linear behavior is only seen for very large supercells. We draw the attention of the reader to the fact that the corrections applied in the case of the charged defect, although small, favor a linear convergence.

Since our final interest is to analyze the strain driven point defect segregation around Frank loops, once the EDT components of all relevant point defects are obtained for the dilute limit, we applied a rotation operator to them in order to be consistent with the coordinate system of the supercell containing the loop. The calculated EDT are given by:

$$\mathbf{G}[V_{Cu}^{-1}] = \begin{pmatrix} 5.68 & 0 & 0 \\ 0 & 7.07 & 1.39 \\ 0 & 1.39 & 7.07 \end{pmatrix} \text{eV}$$

$$\mathbf{G}[Cu_i^{+1}] = \begin{pmatrix} -4.43 & 0.78 & -0.78 \\ 0.78 & -4.38 & 1.86 \\ -0.78 & 1.86 & -4.38 \end{pmatrix} \text{eV}$$

$$\mathbf{G}[\mathrm{In}_{\mathrm{Cu}}^{+2}] = \begin{pmatrix} -7.95 & 0 & 0 \\ 0 & -6.51 & 1.44 \\ 0 & 1.44 & -6.51 \end{pmatrix} \mathrm{eV}$$

$$\mathbf{G}[\mathrm{Cu}_{\mathrm{In}}^{0}] = \begin{pmatrix} -8.34 & 0 & 0 \\ 0 & -6.01 & 2.33 \\ 0 & 2.33 & -6.01 \end{pmatrix} \mathrm{eV}$$

$$\mathbf{G}[\mathrm{Cu}_{\mathrm{In}}^{-1}] = \begin{pmatrix} 2.06 & 0.03 & -0.03 \\ 0.03 & 4.09 & 2.17 \\ -0.03 & 2.17 & 4.09 \end{pmatrix} \mathrm{eV}$$

$$\mathbf{G}[\mathrm{Cu}_{\mathrm{In}}^{-2}] = \begin{pmatrix} 13.13 & 0.19 & -0.19 \\ 0.19 & 15.13 & 1.64 \\ -0.19 & 1.64 & 15.13 \end{pmatrix} \mathrm{eV}$$

We point out that, as discussed previously, the EDT for charged defects calculated using VASP can only be used to draw qualitative conclusions. Having this in mind, let us continue with out analysis. We must keep in mind that the formation energy of a defect would decrease only if the term $\sum_{\eta\zeta} G_{\eta\zeta}[\mathrm{D}^q]\mathrm{u}_{\eta\zeta}$ is positive. As we can see, the largest positive $G_{\eta\zeta}[\mathrm{D}^q]$ are found for the $\mathrm{Cu}_{\mathrm{In}}^{-2}$ antisite and therefore, it is the preferred defect in areas under tensile strain. On the other hand, $\mathrm{In}_{\mathrm{Cu}}^{+2}$ antisites exhibit the largest negative $G_{\eta\zeta}[\mathrm{D}^q]$ and hence, could be expected to occur in areas under compressive strain. As a quantitative example, Figure 29e and 29f show the values of $\sum_{\eta\zeta} G_{\eta\zeta}[\mathrm{D}^q]\mathrm{u}_{\eta\zeta}$ for $\mathrm{Cu}_{\mathrm{In}}^{-2}$ and $\mathrm{In}_{\mathrm{Cu}}^{+2}$ antisites, when immersed in the theoretical strain field presented in Figure 29c and 29d. The maximum change in formation energy due to strain for such antisites is around 1.51eV for the $\mathrm{Cu}_{\mathrm{In}}^{-2}$ and 0.65eV for the $\mathrm{In}_{\mathrm{Cu}}^{+2}$, which are of the order of formation energies of these defects in $CuInSe_2$ [5]. Therefore, the massive excess Cu clouds are likely caused by strain-driven accumulation of such defects. Charge accumulation associated with an excess of $\mathrm{Cu}_{\mathrm{In}}^{-2}$ must be compensated, which may be satisfied through the presence of $\mathrm{In}_{\mathrm{Cu}}^{+2}$ antisites, creating positively charged In-area directly opposite the Cu clouds. The EELS maps show a few atomic columns below the cores and to the side of the stacking fault (in the compressive region) where a significant increase in In signal is accompanied by a decrease in Cu, pointing towards the presence of the expected $\mathrm{In}_{\mathrm{Cu}}^{+2}$ antisites.

4.5 ELECTRONIC PROPERTIES AND EFFECTS OF THE POINT DEFECT SEGREGATION

After unraveling the causes of such chemical changes inside and around the α and β-cores, we used the LDOS of both structures when decorated with their preferred point defects, Figures 31a and 31b, to study the effects of such non-stoichiometric structures on the electrical properties of the absorber layer. We found out that the presence of Cu_{In} inside both, α- and β-cores, induces a defect state around the middle of the gap and enhances non-radiative recombination. Thus, the decorated Frank loop should be electrically active due to the presence of Cu_{In} inside the α- and β-cores. Moreover, although there are no dangling bonds in the stoichiometric structures, defect states are also observed in the LDOS of the stoichiometric structures. We argue that they are strain induced, similar to what has been observed in the case of threading dislocations in GaN [228].

Regarding the effect of such clouds on the electrical properties of a device containing dislocation loops like the one studied here, it has been pointed out in previous studies, that the Cu_{In}^{-2} antisite constitutes the most harmful hole-trap in Cu(In,Ga)Se_2 absorber layers [5]. Thus, Cu clouds composed by such defects would be also detrimental for the efficiency of the device.

In the case of the quaternary compound Cu(In,Ga)Se_2, conclusions can be draw by including Ga in our analysis. In such situation the expected In rich clouds would include Ga_{Cu}^{+2} along with In_{Cu}^{+2}, since both would respond similarly to strain due to the analogous ionic radius of In and Ga. It has been proven that both Ga_{Cu}^{+2} along with In_{Cu}^{+2} are shallow donor defects [5]. Therefore, our finding of Cu_{In} presence being the factor determining the detrimental nature would remain valid for Cu(In,Ga)Se_2.

4.6 SUMMARY

In conclusion, by means of DFT calculations we have elucidated the structure and chemistry of Frank loops in Cu(In,Ga)Se_2 thin films at atomic-resolution as observed in experiments. Both EELS and DFT results suggest that inside the cores, asymmetric Cu excess occurs depending on the structurally caused cation or anion excess in α- and β-cores, respectively. We found that the considerable Cu excess observed in the α-core is due to the neutral Cu_{In}^{0} antisites, which have a negative formation energy and therefore may form spontaneously. In the case of the β-core, the slight Cu excess is explained by the presence of both Cu_{In} and Cu interstitials, which have low positive formation energies inside the β-core. Evidence is provided that the formation of the Cu clouds detected outside of the core region, which probably consist of Cu_{In}^{-2} point defects, is driven by interaction of the strain fields of the dislocations with the point defects. Also due

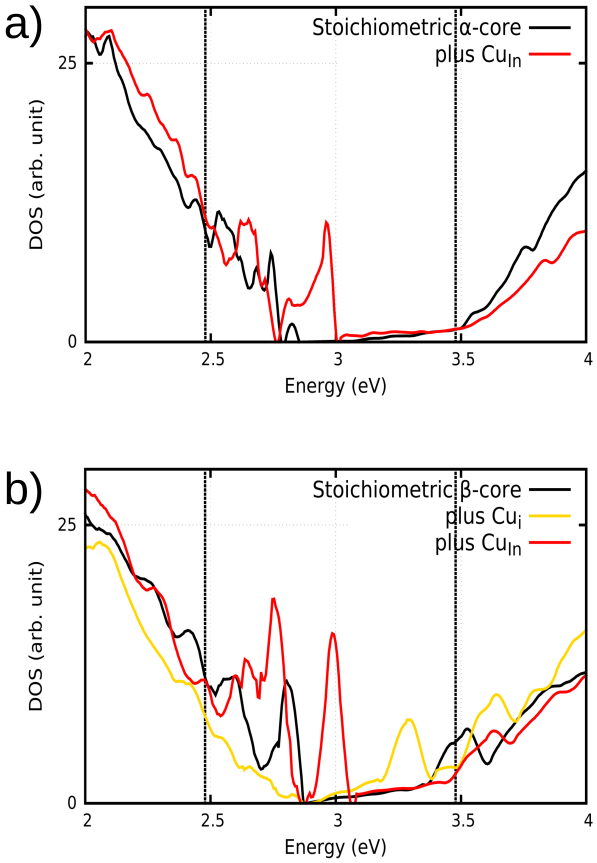

Figure 31.: LDOS of stoichiometric and decorated cores are shown for both α-core (a) and β-core (b). The band gap of the bulk structure is marked by doted vertical lines.

to strain, In_{Cu}^{+2} antisites are predicted to accumulate in areas under compressive strain, providing a charge-compensation mechanism. Although not as prominent as the Cu rich clouds, they are observed by means of the EELS. Since the electronic structure calculations suggest that the presence of Cu_{In} at the α- and β-cores induces deep mid-gap defect states, the annihilation of Frank loops during the Cu(In,Ga)Se_2 growth is essential in order to obtain high absorber qualities for record conversion efficiencies of the corresponding solar-cell devices. These findings could, at least partially, explain the beneficial effect of the observed PDs annihilation associated to the Cu-rich stage in the three-stage coevaporation technique used to deposit high efficient Cu(In,Ga)Se_2-based solar cells.

5

PERFECT DISLOCATIONS IN $CuInSe_2$ AND $CuGaSe_2$

The results in this chapter were first published in Ref. [201].

5.1 INTRODUCTION

In the previous chapter we focused on Frank partials and loops, which were observed in an absorber whose growth process was interrupted before reaching the Cu-rich phase. We found that such defects are detrimental and its annihilation due to the Cu-rich stage could at least partially explain the physical mechanism behind the efficiency boost induced by this stage on fully grown samples. Nevertheless, as discussed in Chapter 1, by means of transmission electron microscopy, significant dislocation densities up to 10^{11} cm^{-2} were found in fully grown $Cu(In,Ga)Se_2$-based solar cells, which at the same time show power-conversion efficiencies of more than 15% [13]. This finding implies that lattice dislocations in fully grown $Cu(In,Ga)Se_2$-based absorber materials are electrically inactive. So far, experimental studies have dealt with the properties of line defects in single crystalline $CuInSe_2$ and found evidence for the presence of $\langle 1\,1\,0 \rangle$-type superdislocations [108]. A recent experiment on polycrystalline samples was conducted by Dietrich *et al*. [13]. They found full, undissociated 60°-mixed dislocations with an inserted {112} half-plane and showed that the density of dissociated dislocations and stacking faults is rather low compared to Si crystals.

In this chapter, we present a theoretical study of undissociated 60°-mixed and pure screw dislocations by means of DFT calculations. We start our discussion with the relaxed core structures and their electronic properties based on the LDOS. Then, we use atomic orbital theory (AOT) to reveal the origin of the observed defect states. Afterwards, we determine how charging affects the formation energy of dislocation dipoles allowing us to draw conclusions regarding the electrical activity of such extended defects. Finally, in order to grasp some insight on the properties of individual cores, local changes in the charge density of the neutral dipoles are studied by means of the Bader charge analysis.

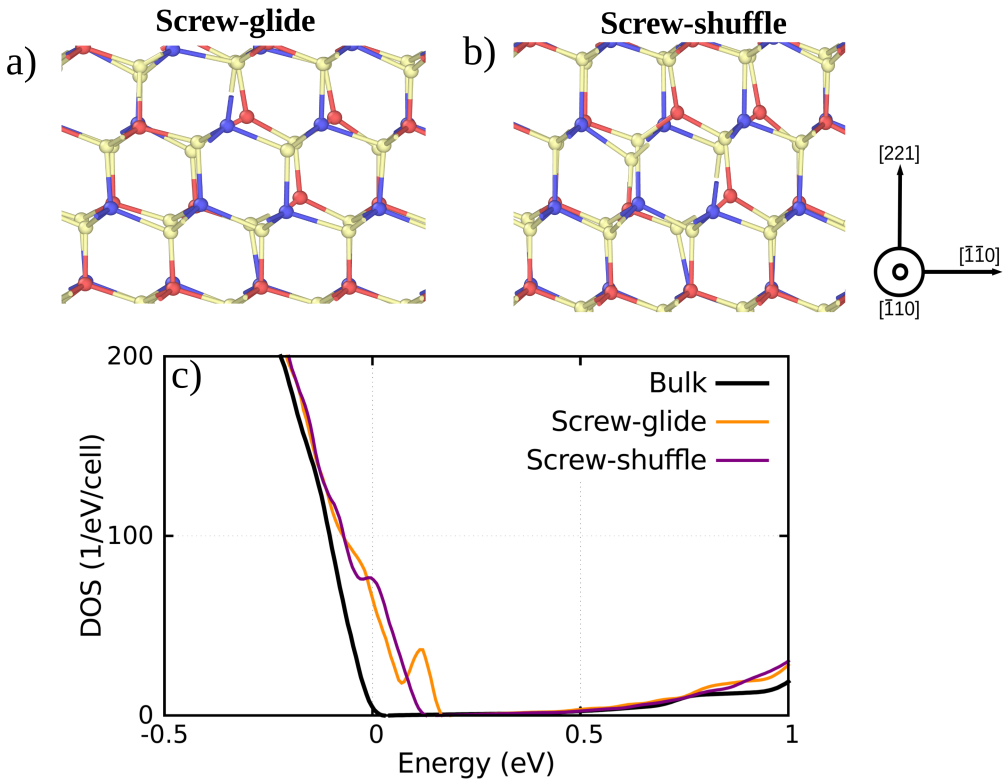

Figure 32.: Relaxed cores structures of screw dislocations in $CuInSe_2$ in their glide (a) and shuffle (b) configurations. Copper, indium and selenium are shown in red, blue and yellow, respectively. Structures are visualized using OVITO. The DOS of the neutral states of these relaxed configurations is shown in (c).

5.2 ATOMIC AND ELECTRONIC STRUCTURES

As explained in Section 3.5, the starting geometries, obtained from applying the displacement field of each dislocation to the supercell, are relaxed into the structures shown in Figures 32, 33, 34, and 35, where only bonds shorter than 2.8Å are presented. The structural features observed for each relaxed core are correlated with their electronic structure. The latter is studied by means of their DOS (obtained from the LDA+U calculations), which is presented in the same figures. As mentioned before, the LDA+U method opens the bandgap only partially. Despite this limitation, it allows us to clarify whether or not defect states are induced by the dislocations. We remark that the actual position of charge transition levels associated with the observed defect states is determined by means of the LDA/LDA+U extrapolation method, whose results are presented in detail in the next section. Whenever we refer to the CBM in the current subsection,

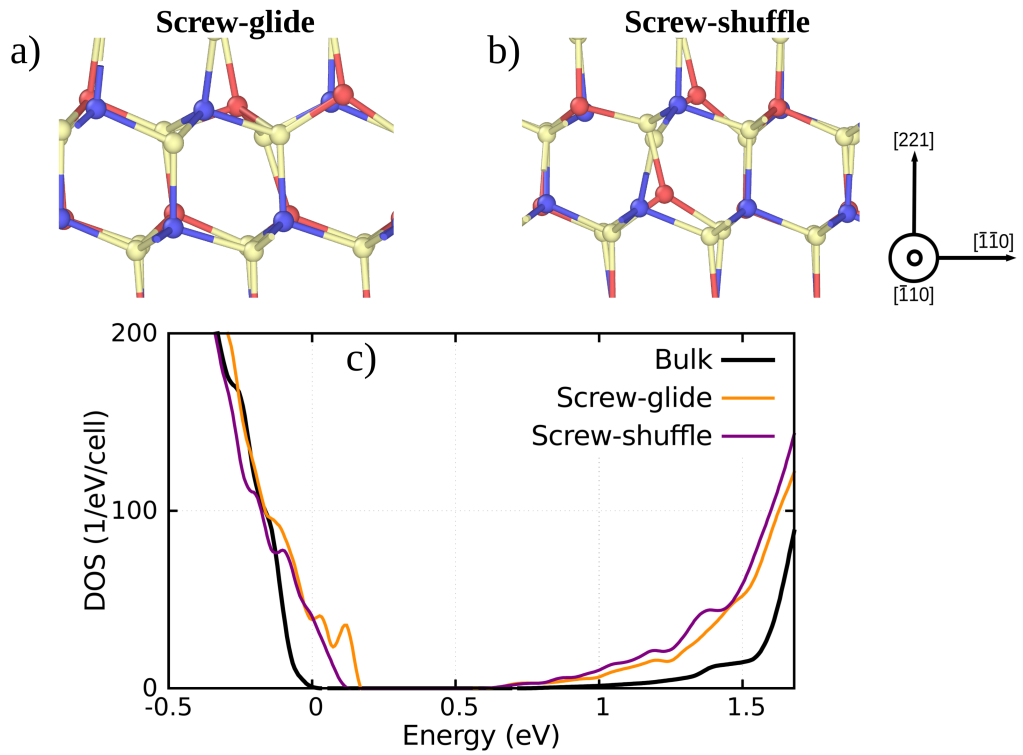

Figure 33.: Relaxed cores structures of screw dislocations in $CuGaSe_2$ in their glide (a) and shuffle (b) configurations. Copper, gallium and selenium are shown in red, blue and yellow, respectively. Structures are visualized using OVITO. The DOS of the neutral states of these relaxed configurations is shown in (c).

we mean its experimental location, which corresponds to the upper limit of the energy range in all graphs showing the DOS.

We start our analysis with studying pure screw dislocations in $CuInSe_2$ and $CuGaSe_2$, of both glide and shuffle sets. As mentioned before, for this dislocation type each dipole is formed by two structurally equivalent cores. Their relaxed structures can be seen in Figures 32a-b and 33a-b. The first point to notice is that neither cation-cation or anion-anion bonds, called "wrong" bonds in the following, nor dangling bonds are present in these structures. However, strain associated changes in bond lengths do exist. Using the coordination analysis tool provided by OVITO, we studied the minimum distance between atoms in the surrounding of the core compared to the bulk case. For the glide set in $CuInSe_2$, this distance is 4.9% shorter compared to the bulk case, and 4.5% shorter for the shuffle dislocation. In $CuGaSe_2$, the same analysis results in a 4.3% decrease in the minimum distance between atoms for the glide dislocation, and 3.2% for the shuffle dislocation. Thus, in both materials the glide dislocation induces larger changes in the structure compared to its shuffle counterpart.

The DOS of the screw dislocations in these materials, Figures 32c and 33c, present defect states close to the VBM and CBM for both the glide and shuffle dipoles. Based on the structural analysis performed before, we conclude that these states are strain induced. A similar situation was observed for threading dislocations in GaN, where in absence of dangling bonds, a localized defect state was observed [228]. Due to the fact that compression of bonds is larger for the glide cores, defect states in this case exhibit a more pronounced detachment from the band edges. This is easy to observe for the state close to the VBM. For both, screw glide and shuffle dislocations, states close to the CBM are accompanied by a band tail caused by the strain field around the dislocation cores [229].

We continue our analysis with the 60°-mixed dislocation. In $CuInSe_2$, the α-core of the glide set, Figure 34a, exhibits several cations which are not fully coordinated, including the ones that terminate the inserted plane. Dangling bonds occur and there are also two "wrong" bonds (one Cu-Cu and one Cu-In) in this core. In the case of the β-core, Figure 34b, there is one Se-Se bond and one of the Se atoms located at the termination of the inserted half plane is not fully coordinated. The latter leads to the formation of dangling bonds. The α-core of the shuffle structure exhibits three "wrong" bonds, namely a Cu-In, a Se-Se and a In-In which crosses the center of the core, as shown in Figure 34c. An important point is that besides a "wrong" Cu-Cu bond, the β-core of the same set exhibits full coordination as can be seen in Figure 34d. Performing the same coordination analysis mentioned before, we find a 5.1% and 4.5% decrease of the minimum distance between atoms for the glide and shuffle dislocations, respectively. The DOS of these dislocation types, Figure 34e, shows that the shuffle structures induce defect states close to the VBM. On the other hand, for the glide set dipole we found defect states located at $E_{\mathrm{VBM}} + 0.41$ eV and at $E_{\mathrm{VBM}} + 0.58$ eV along with a state just above the VBM and another state inside the conduction band tail.

In $CuGaSe_2$, the α-core of the glide configuration contains three gallium atoms which are not fully coordinated (Figure 35a). Consequently, dangling bonds are formed. One of them is a gallium atom at the end of the inserted half plane. In addition, one Cu-Cu and one Ga-Ga "wrong" bonds are found. In the case of the glide β-core, Figure 35b, one of the selenium atoms that terminates the half-plane is not fully coordinated, leading to a dangling bond. Furthermore, as in $CuInSe_2$, there is one Se-Se "wrong" bond in this core. Regarding the shuffle set, the α-core presented in Figure 35c, exhibits three "wrong" bonds, namely a Cu-Cu, a Cu-Ga and a Ga-Ga which crosses the center of the core. On the other hand, as it was observed for the case of $CuInSe_2$, besides a weak "wrong" bond (Cu-Cu), the β-core of the same set shown in Figure 35d exhibits full coordination. In $CuGaSe_2$, the minimum distance between atoms is found to decrease by 2.9% and 2.5% for the glide and shuffle sets, respectively. Regarding the electronic structure, their DOS exhibits several induced defect states as can be seen in Figure 35e. Nevertheless, for this material defect states are only found close to the VBM.

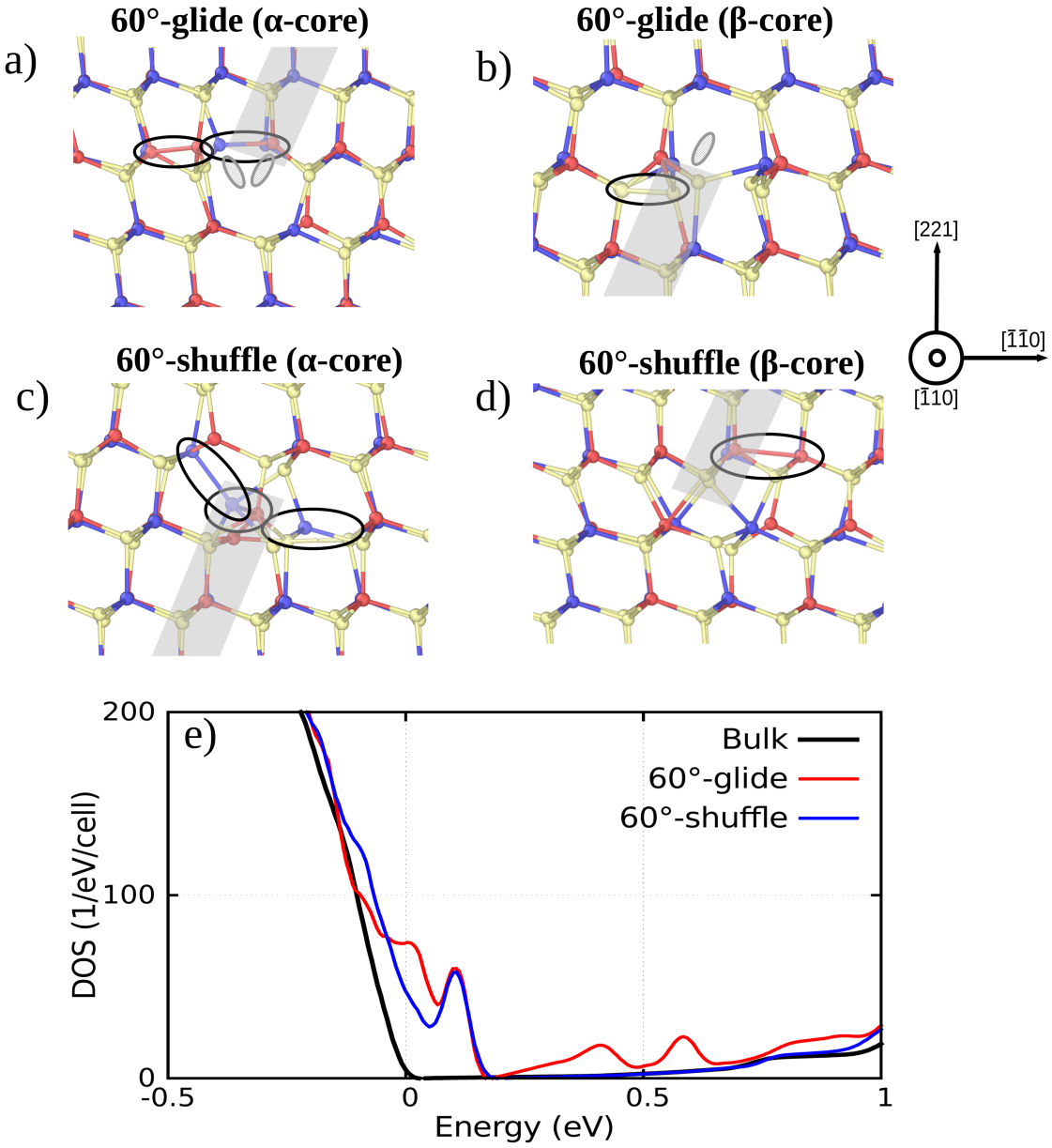

Figure 34.: Relaxed cores structures of 60°-mixed dislocations in $CuInSe_2$: α-core (a) and β-core (b) of the glide configuration and α-core (c) and β-core (d) of the shuffle configuration. "Wrong" and dangling bonds are marked by ellipses. The ones with black boundary for the former and the ones striped for the later. Copper, indium and selenium are shown in red, blue and yellow, respectively. The highlighted gray region marks the inserted half plane. Structures are visualized using OVITO. The DOS of the relaxed and charge neutral dislocation dipoles are shown in (e).

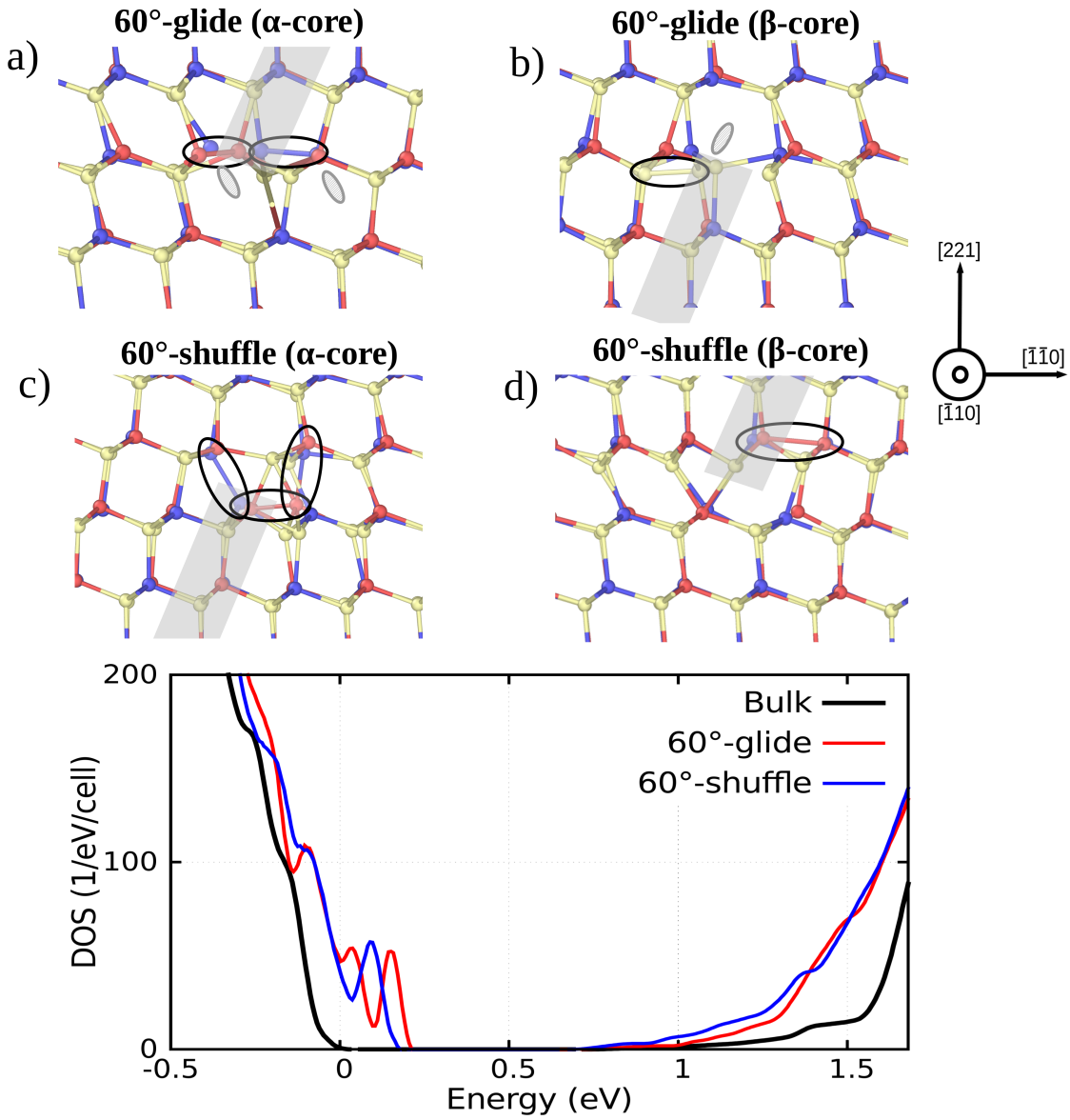

Figure 35.: Relaxed cores structures of 60°-mixed dislocations in $CuGaSe_2$: α-core (a) and β-core (b) of the glide configuration and α-core (c) and β-core (d) of the shuffle configuration. "Wrong" and dangling bonds are marked by ellipses. The ones with black boundary for the former and the ones striped for the later. Copper, gallium and selenium are shown in red, blue and yellow, respectively. The highlighted gray region marks the inserted half plane. Structures are visualized using OVITO. The DOS of the relaxed and charge neutral dislocation dipoles are shown in (e).

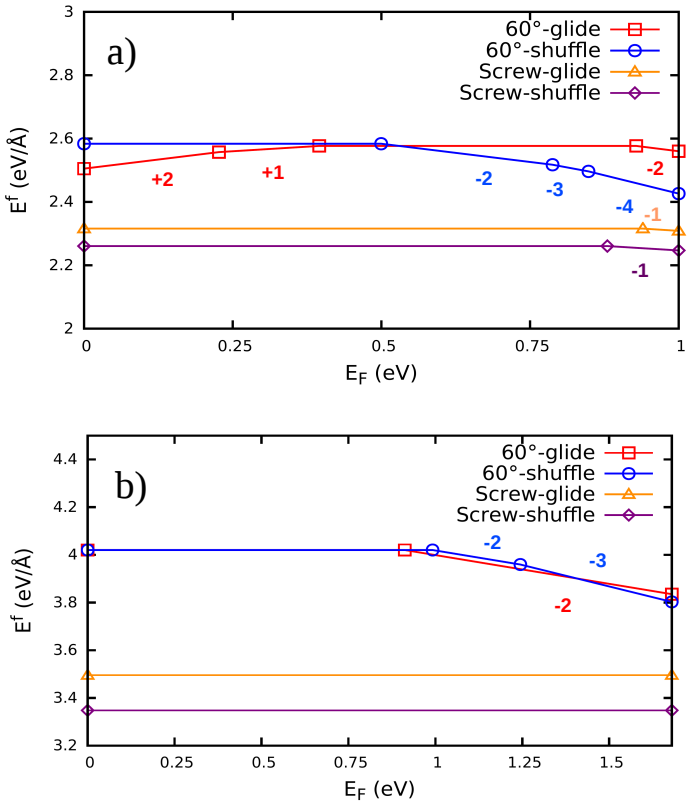

Figure 36.: Formation energies of the screw and 60°-mixed dislocation dipoles. In $CuInSe_2$ (a) and in $CuGaSe_2$ (b). Charge states are given by the slopes of the formation energy lines and for each dislocation type they are marked by numbers with corresponding color.

Beside the induced defect states, there are other features common to both materials for this dislocation type, e.g the existence of a large conduction band tail which originates from the strain introduced by the dislocation. Further common features are that bond deformation is larger for the glide structures and that all defect states are localized.

5.3 ELECTRICAL ACTIVITY AND ORIGIN OF DEFECT STATES

Let us now analyze the electrical activity of the various dislocations by comparing their formation energies and inspecting the charge transition levels they induce. As explained in Chapter 3, every dipole of 60° dislocations consist of two different cores, one α-core and one β-core. Therefore, their individual formation energies cannot be obtained from supercell calculations containing dipoles.

Consequently, formation energies considered in the following are calculated per dipole. For a particular Fermi level and dislocation type, we only display the formation energy of the charge state, per dislocation dipole, with the lowest formation energy. For clarity, we emphasize that the formation energies obtained from Eq. 3.22, are divided by the cell length of the relaxed structure in the direction of the dislocation line. In Figure 36, the charge state is given by the slope of the plot and is labeled by colored numbers. We remark again that charge transition levels, $\epsilon(q/q')$, of a given defect must not be confused with the defect Kohn-Sham states. In the previous section we analyzed the defect states induced by the dislocation dipoles and their position in the DOS of the LDA+U calculation. In order to study the electrical activity of these dipoles, we use the LDA/LDA+U extrapolation method, which allows us to obtain accurate charge transition levels associated with the found defect states when the gap is opened up to its experimental value. In order to obtain information about the origin of the transition levels, we inspect the local DOS of each individual core.

Results for $CuInSe_2$ are presented in Figure 36a. The screw dislocations in this material have a similar behavior for both glide and shuffle sets. They are neutral when the Fermi level is below 0.93eV and 0.88ev, respectively. Above those levels, the dipoles prefer a singly negative charge state. Therefore, these dislocation types introduce an extremely deep acceptor level, which is electrically harmless. One further remark is that for all charge states and both n-type and p-type conditions, the shuffle set of the screw dislocation dipole have a lower energy than its glide counterpart.

For the same material, our results point out that 60° dislocation dipoles are electrically active. Specifically, the shuffle 60° dislocation dipole exhibits a neutral charge state until the Fermi level reaches 0.49eV. Above that value, deep acceptor levels appear (2^-, 3^- and 4^- charged states are stable). Therefore, this dislocation pair would prefer to be charged for n-type conditions and neutral for p-type conditions. Moreover, in an n-type sample of $CuInSe_2$ the shuffle configuration is always lower in energy than its glide conterpart. The case of the glide 60° dislocations is exceptional in the sense that deep donor levels are observed for Fermi energies below 0.40eV, where 1^+ and 2^+ states are stable. Furthermore, a harmless extremely deep acceptor level was also found for a Fermi energy of 0.92eV. Within the p-type regime, the glide configuration has a lower formation energy. For example, at $E_F = 0.0$eV, the formation energy of the glide core is 2.5 eV/Å and 2.58 eV/Å for the shuffle core. Thus, if a 60° dislocation exists in a p-type sample of $CuInSe_2$, it would in principle prefer the glide configuration. However, as mentioned before, dislocation formation is not thermally activated, but a result of the growth kinetics or strain release. Thus, the formation energies only provide a measure for the excess energy needed to form one or the other.

The calculated values for $CuGaSe_2$ are presented in Figure 36b. In general, we found that 60° dislocation dipoles in this material are electrically active but their formation energies do not show a strong dependence on the Fermi level, contrary

to what was found for $CuInSe_2$. Additionally, all dislocations are predicted to be in a neutral charge state for *p*-type conditions. The screw dislocations, as for $CuInSe_2$, have a similar behavior for both glide and shuffle sets and they are neutral for all Fermi energies. Regarding the 60° dislocations in this material, contrary to what was found in $CuInSe_2$, both glide and shuffle sets behave in a similar way: they induce deep acceptor levels. Furthermore, the difference in formation energies between the glide and the shuffle 60° is small for all *p*-type, *n*-type and intrinsic regimes.

These thermodynamic charge transition levels provide insights about the electrical activity of the supercells containing a dislocation dipole. However, the following question arises: which of the two chemically different cores is associated with the acceptor levels and which with the donor ones?. To answer this question we focus on the glide 60° dislocation dipole in $CuInSe_2$, which exhibits both behaviors. We start by comparing the total Bader charges associated with the surrounding volumes of both cores, with respect to the Bader charge accumulated in the same volume in a defect free supercell. From this comparison we get the change in the Bader charges, ΔN_e, inside the analyzed volume for different charge states. The volume assigned to a given core corresponds to the volume of a cylinder with a radius of 8 Å , whose axis corresponds to the dislocation line. This means that a volume of ∼30% of the total volume of the supercell is assigned to each core. With that information at hand, we can establish which core receives or releases electrons while the supercell gets charged. Results of this calculation are shown in Table 1. We find that around 57% of the electrons given away in the $2^+/1^+$ and $1^+/0$ transitions come from the β-core. Regarding the acceptor level, the data suggest that around 56% of the two electrons added to the supercell in the $0/2^-$ transition are located at the α-core. This gives us a first indication that acceptor states are induced by α cores and donor levels, if present, by β-cores. We remark that the excess charge is not fully localized in one of the cores. This is due to the unavoidable charge transfer between the cores in the dipole configuration we used in our study.

	ΔN_e			
	+2	+1	0	-2
α-core	-0.13	0.29	0.72	1.84
β-core	-1.87	-1.29	-0.72	0.16

Table 2.: Change in the Bader charge accumulated inside a cylinder around the α- and β-cores of the glide 60° dislocation dipole in $CuInSe_2$ for its possible charge states. As explained in the text, the reference used is the Bader charge accumulated inside an equivalent cylinder located in a defect free supercell.

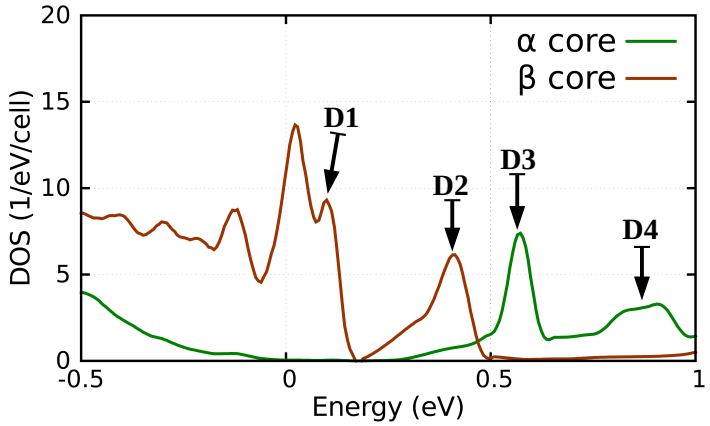

Figure 37.: LDOS of both α and β-cores of the glide 60° dislocation dipole in $CuInSe_2$ indicating D1, D2, D3 and D4 defect states.

In the following, we use the LDOS as second and conclusive tool to clarify which of the two chemically different cores is associated with the acceptor levels and which with the donor ones. We calculated the LDOS for atoms inside a radius of 8Å from the center of the core of α and β-types of the glide 60° dislocation in $CuInSe_2$ (Figure 37). It is expected that $2^+/1^+$ and $1^+/0$ transitions levels are associated with the defect states close to the VBM observed for this dislocation type. By means of the LDOS, we are able to indicate which core is associated with these defect states. We find that defect states closer to the VBM, which we name D1 and D2, are induced by the β-core. This provides a further proof that this core type is associated with donor levels. Analogously, it is expected that the $0/2^-$ transitions level is associated to defect states close to the CBM. From the LDOS we prove that such defect states, which we name D3 and D4, are indeed induced by the α-core. This result confirms that this core type induces acceptor states.

Now we direct our attention to the origin of the four defect states induced by the glide 60° dislocation dipole, whose individual charge density isosurfaces are shown in Figures 38a-d. Such analysis allows us to understand also the defect states and levels induced by the other dislocation types in these materials. In the case of grain boundaries in $Cu(In,Ga)Se_2$, it has been pointed out that deep defect states are induced by the cation-cation or anion-anion "wrong" bonds [7, 8]. In Figure 39, we illustrate the arguments based on the AOT, which helps us to understand the previous statement. Regarding dangling bonds, see Figure 39a, the AOT imples that if there is a cation with a dangling bond in $CuInSe_2$ and $CuGaSe_2$, a donor like state will be induced and it would lie between the cation atomic s-orbital and the CBM as indicated by DBS_d, i.e. donor dangling bond state). In the case of an anion dangling bond, an acceptor state will be induced

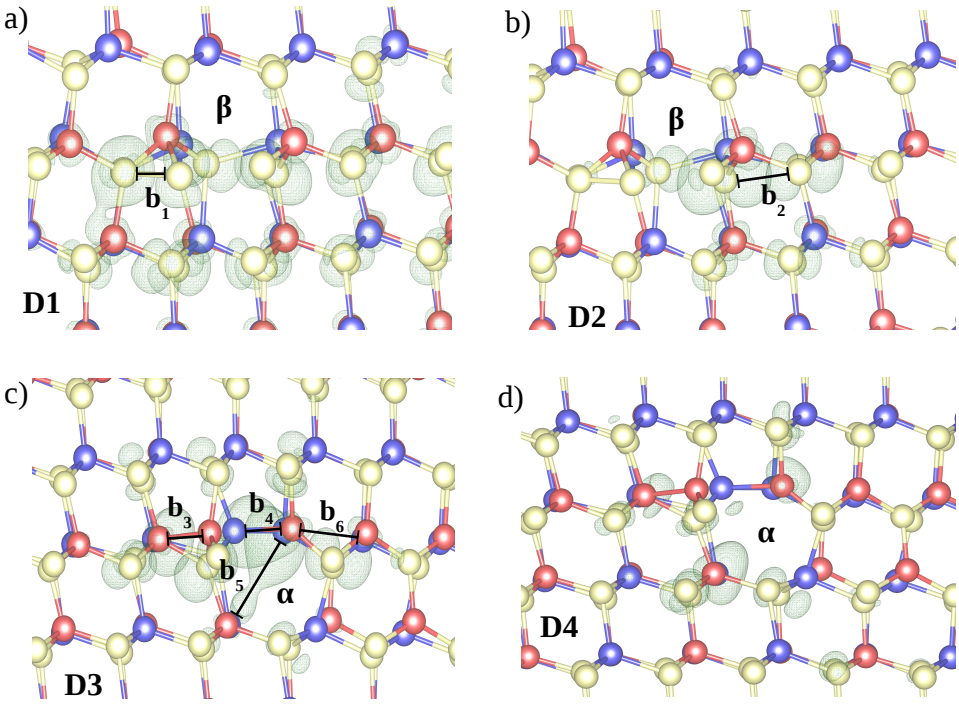

Figure 38.: Charge density isosurfaces of the defect states found for the glide 60° dislocation dipole in $CuInSe_2$: D1 (a), D2 (b), D3 (c) and D4(d). The isosurfaces are visualized using VESTA and are displayed at 10% of their maximum value.

between the anion p-orbital and the VBM as indicated by DBS_a in the same figure. On the other hand, cation-cation or anion-anion "wrong" bonds induce bonding and anti-bonding states which can be located deep inside the band gap, as shown in Figure 39b. There, bonding and anti-bonding defect states are indicated by WBS for the former case and WBS* for the latter (WBS stands for "wrong" bond state). A subscript clarifies whether the WBS is induced by a cation-cation or anion-anion "wrong" bond. As stated before, the position of these defect states is determined by the lengths of the "wrong" bonds, which is directly related to the strength of the bond. We claim that dislocations induce deep defect states by means of this mechanism. As we pointed out when analyzing the structures in the previous subsection, several "wrong" bonds were found in the defects we are studying. In the specific case of the β-core in the glide 60° dislocation dipole, there is a very noticeable Se-Se "wrong" bond highlighted in Figure 34b. When the isosurfaces of the defect states associated with this core are analyzed together with its structural features, we notice that defect state D1 is strongly influenced by the Se-Se bond mentioned above. In general, D1 and D2 are induced by Se

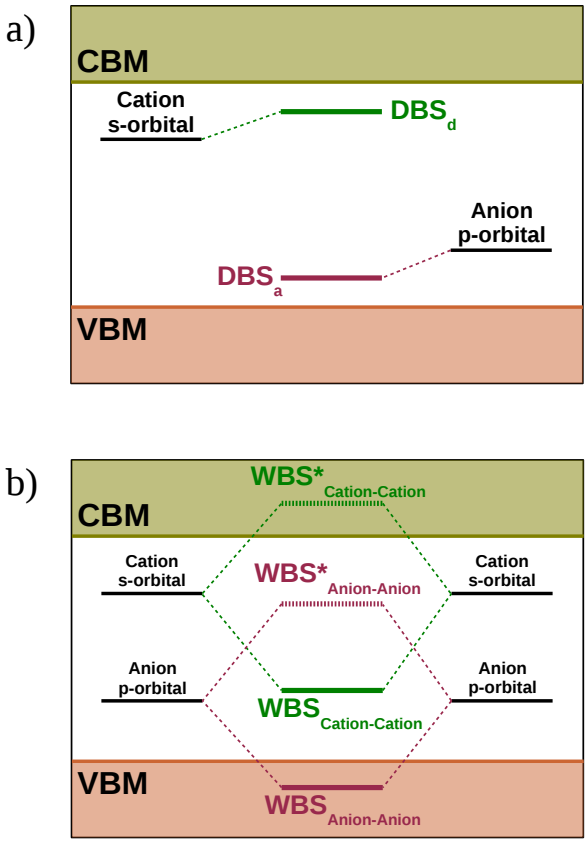

Figure 39.: Atomic orbital theory picture on the formation of defect levels in $CuInSe_2$ and $CuGaSe_2$: for dangling bond states (DBS) (a) and for "wrong" bond states (WBS) (b). Anti-bonding states in the case of WBS's are indicated by a *.

orbitals. For D2, we notice that it is induced by a Se-Se bond whose existence is evident only by means of the charge density isosurfaces. On the other hand, defect states associated with the α-core are caused by Cu and In orbitals. We highlight that D3 exhibits a strong influence from the Cu-Cu and Cu-In bonds mentioned before and from a bond that crosses the center of the core. This last "wrong" bond was not mentioned in the structural analysis because the simple method used then is not able to detect it. It is an In-In bond with a length of 4.35Å , which is remarkably long compared to the In-In distance of $\sim$4Å found in the bulk. Based on the "wrong" bonds distribution discussed in the previous subsection, an analogous AOT-based analysis provide further proof that acceptor and donor levels, if present, are induced by α- and β-cores, respectively.

The strength of the "wrong" bonds depends on how strained they are. Therefore, an analysis of their lengths provides further insights about the origin of the

electronic properties found for the studied dislocations. We can now clarify why the glide 60° dislocation dipole in $CuGaSe_2$ does not induce defect states in the same positions as $CuInSe_2$ despite both relaxed cores exhibit similar features. For that matter, the length of relevant "wrong" bonds indicated in Figures 38(a)-(d) are reported in Table 2 for both materials. Each bond is designated as b_x, where the subscript x indicates a specific bond. They should not be confused with the Burgers vector of the dislocations.

	Distance (Å)					
	b_1	b_2	b_3	b_4	b_5	b_6
$CuInSe_2$	2.45	3.45	2.68	2.61	4.35	3.53
$CuGaSe_2$	2.41	3.64	2.35	2.62	4.17	2.37

Table 3.: Comparison of relevant atomic distances within the α- and β-cores of the glide dislocation dipole in both $CuInSe_2$ and $CuGaSe_2$.

We find that the Se-Se bond, b_1, relevant for the D1 defect state and seen in both β-cores is equally strong in both materials. Therefore, the position of the D1 state should be the same in both materials. This is actually what is seen in the DOS of both glide dipoles, Figure 34e and Figure 35e. However, the defect state D2 is located at different positions for each of the cores. For the $CuGaSe_2$ structure it is seen close to the VBM and just above the D1 state. The reason for this is that the Se-Se bond with largest contribution to that state, b_2, is shorter in the $CuInSe_2$ core. Hence, the WBS* state D2 is pushed away from the VBM for that material. Electrical activity of the glide β-core in $CuInSe_2$ is related to both D1 and D2 defect states. Since for the $CuGaSe_2$ core these two defect states are close to the VBM, they do not create any deep donor charge transition level for that material.

Let us now focus on the acceptor states. The first issue to be addressed in this case is why the position of the D3 state is also not the same for the $CuGaSe_2$ glide 60° dislocation dipole. As shown before, this state is associated to the α-core of that dislocation type and the largest contribution to the formation of such defect state in the $CuInSe_2$ core comes from a Cu-Cu bond, b_3, a Cu-In bond, b_4, and from an In-In bond, b_5, that crosses the center of the α-core. In Table 1, we report the length of these three bonds along with a cation-cation b_6 "wrong" bond which, although non existing for the $CuInSe_2$ structure, is important in the case of its $CuGaSe_2$ counterpart. Since in all cases these bonds are shorter in $CuGaSe_2$, the defect state D3 (caused by bonding $WBS_{Cation-Cation}$ states) is pushed further into the band gap, close to the VBM in the LDA+U calculation. Actually, for the glide 60° dislocation dipole in $CuGaSe_2$, defects above the VBM are a mixture of D1, D2 and D3 states observed in the $CuInSe_2$ structure. The acceptor levels related to the D3 state are close to the CBM in $CuInSe_2$. As this

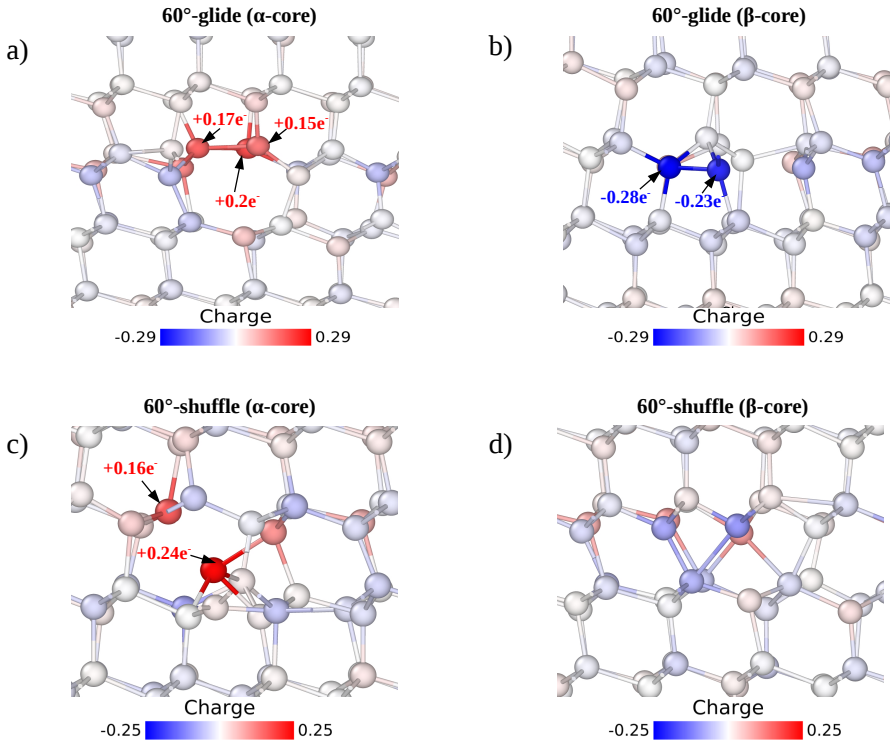

Figure 40.: Difference in Bader charges between a neutral supercell containing a 60° dislocation dipole and a defect free supercell for $CuInSe_2$: α-core of the glide set (a), β-core of the glide set (b), α-core of the shuffle set (c) and β-core of the shuffle set(d). A positive or negative difference means that the atoms located at such position gained or lost, respectively, electrons in the presence of the dislocation dipole. All dipoles presented here are neutral and visualized using OVITO.

defect state is further apart from the CBM for $CuGaSe_2$, when the band gap is opened up to its experimental value the correspondent transition levels should also get deeper into the gap compared to the $CuInSe_2$ case. This result is in-line with our calculated transition levels for the glide 60° dislocation dipole in $CuGaSe_2$. Finally, the state D4 is induced by the same In-In bond, b_5, that crosses the center of the core. However, it is caused by the anti-bonding $WBS^{*}_{Cation-Cation}$ state. Hence, due to a shorter bond length in $CuGaSe_2$, this state is pushed up into the CBM and is not seen in the case of that material.

Using the AOT, we can also understand our findings for the shuffle cores. In both materials the β-cores are fully coordinated and no Se-Se bond is observed. Therefore, based on the previous discussion, donor levels do not occur for these structures. Furthermore, the observed cation-cation bond in this core is a weak one and will only induce defect states close to the CBM. Structural features ob-

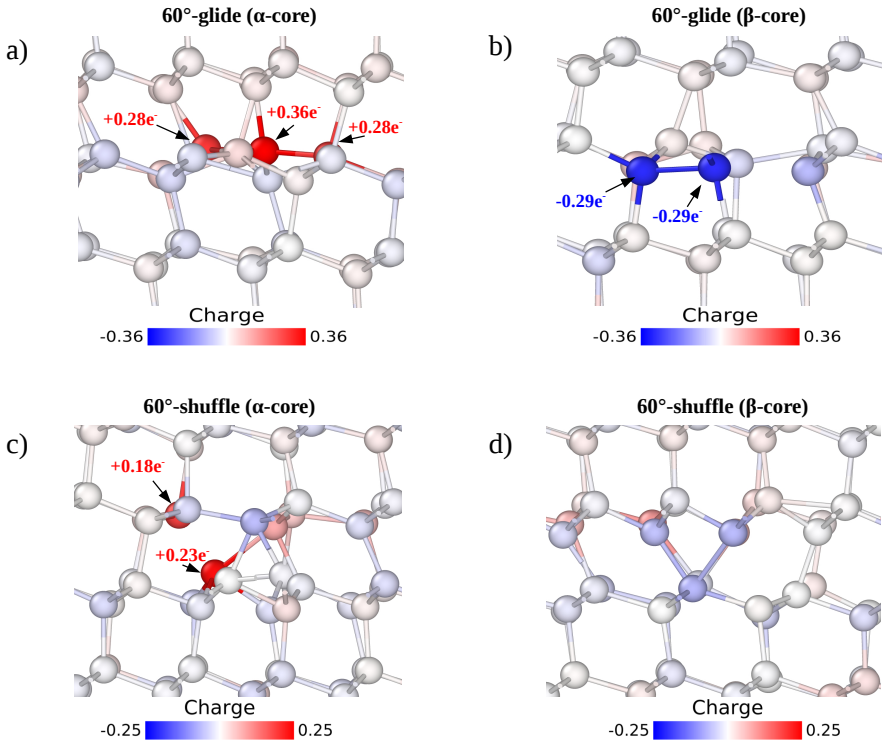

Figure 41.: Difference in Bader charges between a neutral supercell containing a 60° dislocation dipole and a defect free supercell for $CuGaSe_2$: α-core of the glide set (a), β-core of the glide set (b), α-core of the shuffle set (c) and β-core of the shuffle set(d). A positive or negative difference means that the atoms located at such position gained or lost, respectively, electrons in the presence of the dislocation dipole. All dipoles presented here are neutral and visualized using OVITO.

served for the α-cores are common in both materials. The D3-like defect state induced by that core, a strong bonding $WBS_{Cation-Cation}$ state, is pushed far apart from the CBM and is located just above the VBM in the LDA+U calculation. Therefore, the electrical activity of these cores should be like the one observed for the glide 60° dislocation dipole in $CuGaSe_2$. We proved such conclusion by means of the calculated charge transition levels, where only deep acceptor levels were found for the shuffle dipoles in both materials.

5.4 THE MEANING OF THE NEUTRAL STATE: LOCAL CHARGE ACCUMULATION

Since we use a dipole configuration in this study, the neutral state, mentioned while analyzing the formation energy diagrams, refers to neutral supercells. However, this does not exclude the possibility of local changes in the charge density associated to charge transfer between the cores. In order to have a clear understanding of this feature, we use the Bader analysis to calculate charges associated with each atom in the corresponding supercells. Differences in Bader charges between a neutral supercell containing a 60° dislocation dipole and a defect free supercell for both $CuInSe_2$ and $CuGaSe_2$ are presented in Figures 40 and 41. Although all dipoles shown are neutral, there are indeed local changes in the charge density. In general, there is electron accumulation in α-cores. The reason for this excess in Bader charge is that for cations, each missing or "wrong" bond means that less charge is given away. On the other hand, β-cores of the glide set exhibit electron depletion. The reason for this is that for anions, each missing or "wrong" bond means less charge being accepted. Due to their full coordination, negligible local charge rearrangements are observed for the β-cores of the shuffle set. For completeness, an analogous analysis was performed for the screw dislocations. For the neutral state, such dislocations do not show local charge accumulation or depletion in the surrounding of the cores, not even at the dislocation cores (always below ± 0.03 electrons). The relaxed structures found within this study, Figures 32a-b and Figures 33a-b, explain this behavior since dangling and "wrong" bonds are not seen.

5.5 SUMMARY

We have performed first-principles calculations of relaxed dislocation cores with smallest **b** in a chalcopyrite structure, the screw and the 60°-mixed types. In both, $CuInSe_2$ and $CuGaSe_2$, screw dislocations present distorted bonds, but are characterized by fully coordinated cores after relaxation. On the other hand, relaxed structures of the 60°-mixed dislocations exhibit dangling and "wrong" bonds. In order to clarify whether the glide or the shuffle set is prefered, we calculated formation energies of all dipoles. Additionally, based on the position of the charge transition levels found in the dipole formation energy diagrams, we drew conclusions about the electrical activity of the dislocations under study. Our results show that in both materials, $CuInSe_2$ and $CuGaSe_2$, screw dislocations prefer their shuffle configuration. Moreover, no deep transition level was found for this dislocation type, pointing out their harmless nature. On the other hand, deep acceptor levels were observed for most of the 60° dislocation dipoles. The only exception is the glide dislocation dipole in $CuInSe_2$, which exhibits two deep donor levels. By means of Bader charges and LDOS we identified that ac-

ceptor and donor levels, if present, are induced by α and β-cores, respectively. Furthermore, based on the AOT, we proved that deep defect states induced by the dislocation dipoles are caused by the presence of "wrong" bonds observed in the relaxed cores. Additionally, all defect states are found to be localized and in all cores exhibiting "wrong" or dangling bonds there is charge accumulation.

Regarding the properties of 60°-mixed dislocations in the technologically relevant Cu(In,Ga)Se_2 semiconductor alloy, results up to this point allow us to draw conclusions only for the α-cores. Since they are all active acceptors in both parent compounds, it is possible to conclude that they are also active in the quaternary compound. Nevertheless, such conclusion cannot be easily drawn for the β-cores because only the glide set in $CuInSe_2$ is active. This is the reason why in Chapter 6 we will evaluate the segregation tendency and effects of gallium segregation inside the glide β-core in $CuInSe_2$. Such study together with the results presented in this chapter, allow us to draw a complete picture of the properties of dislocations in Cu(In,Ga)Se_2. Therefore, a more detailed discussion on how our results relate to the findings and model presented by Dietrich *et al*. [13], will have to wait until the end of that chapter.

6

PERFECT DISLOCATIONS IN $Cu(In,Ga)Se_2$: NEUTRAL SPECIES SEGREGATION

The results in this chapter were first published in Ref. [230].

6.1 INTRODUCTION

At this point we are aware of the properties of stoichiometric perfect dislocations in $CuInSe_2$ and $CuGaSe_2$. It is clear that most 60°-mixed dislocation core configurations are electrically active in these materials. This is caused by the presence of homopolar cation-cation or anion-anion "wrong" bonds in the active cores. Specifically, we found that in $CuInSe_2$ the glide β-core and the shuffle α-core are active, while in the case of $CuGaSe_2$, both glide and shuffle α-cores are active. Therefore, the apparent harmless nature of dislocations in $Cu(In,Ga)Se_2$ based absorber could only be accounted for if the active 60°-mixed dislocation cores are passivated by chemical changes in their surroundings.

The aim of the present Chapter is to analyze whether the passivating mechanism is associated to the segregation of neutral species into the active dislocation cores in $CuInSe_2$ and $CuGaSe_2$. A first hint that such process could play a role on the properties of dislocations in $Cu(In,Ga)Se_2$ was given in Chapter 5. There we proved that among the β-cores in the parent compounds, only the glide structure in $CuInSe_2$ is electrically active despite the structural similarities with its counterpart in $CuGaSe_2$. Therefore, segregating gallium in the form of neutral Ga_{In} could passivate this electrically active core. If this is the case, we would have a clear indication that β-cores in $Cu(In,Ga)Se_2$ would be electrically inactive. A second segregating species with possible beneficial effects has been pointed out recently by Dietrich *et al.* [13]. They found experimental evidence of sodium accumulation in the surrounding of dislocations in $Cu(In,Ga)Se_2$. Moreover, they proposed a model in which accumulated neutral Na_{Cu} creates a hole barrier that prevents recombination at the cores. The relevance of their study lies in the fact that although it is known that sodium incorporation is crucial to achieve high-efficient $Cu(In,Ga)Se_2$-based solar cells [40, 231, 232], the physical origin of this effect is not fully understood. It is widely accepted to be

partially caused by an enhanced p-type conductivity inside the absorber, resulting in a higher open-circuit voltage [40, 232]. Nevertheless, the specific details of the mechanism through which this enhancement occurs are not yet clear [40, 233, 234]. It has been proposed that sodium accumulates into the grain boundaries and passivates the donor-like defects found there [234–238]. However, atom probe tomography have shown that sodium is also present in the interior of grains [235, 239, 240] where it has been suggested that sodium would create new acceptors or eliminate donor defects [4, 241, 242], but this idea has been challenged by both theory and experiments [233, 241, 243, 244]. Recently, Z-K Yuan *et al.* [245] have proposed an alternative explanation related to sodium out-diffusion during cooling and water rinsing. Nevertheless, the discussion is not yet settled and if, as proposed in Ref. 13, sodium segregation inside electrically active cores in $CuInSe_2$ and $CuGaSe_2$ is preferred and has a beneficial effect, our research would add valuable information to clarify the role of this species when present inside the grains.

Our study is based on DFT calculations performed on supercells containing dislocation dipoles in order to satisfy periodic boundary conditions, as presented in Chapter 3. Based on the previous discussion, we study the segregation of Ga_{In} only in the surroundings of the glide β-core in $CuInSe_2$ but in the case of Na_{Cu}, we focus on all active dislocation cores in $CuInSe_2$ and $CuGaSe_2$. Then, using the concept of the elastic dipole tensor, we aimed at revealing the driving force of the observed segregation tendency. Finally, we analyze the effect of these neutral species on the charge transition levels of the studied dislocation cores and assess whether these neutral species are relevant passivating agents.

6.2 CALCULATION SCHEME

The actual strategy used in order to reveal whether Ga_{In} or Na_{Cu} segregation occurs in the surrounding of the dislocation cores of interest is shown in Figure 43. We start from a stoichiometric supercell containing a dislocation dipole. The first step is to create a Ga_{In} or Na_{Cu} close to the analyzed core. The total energy for that configuration is called E_{near}. We obtained this energy for all different copper or indium sites in the surroundings of the core (closer than 10 Å). Afterwards, an analogous substitution is done for the two farthest apart copper or indium sites. The average energy obtained for these two far configurations is called E_{far}. The Ga_{In} or Na_{Cu} would segregate into the sites close to the core only if the difference $\Delta E = E_{near} - E_{far}$ is negative. The site for which this difference is most negative is the preferred site for the neutral Ga_{In} or Na_{Cu}. The complete scheme is repeated for up to three gallium or sodium atoms inside the supercell. For cases where multiple Ga_{In} or Na_{Cu} are involved, the starting supercell is the relaxed structure obtained at the end of the previous cycle. For example, in case

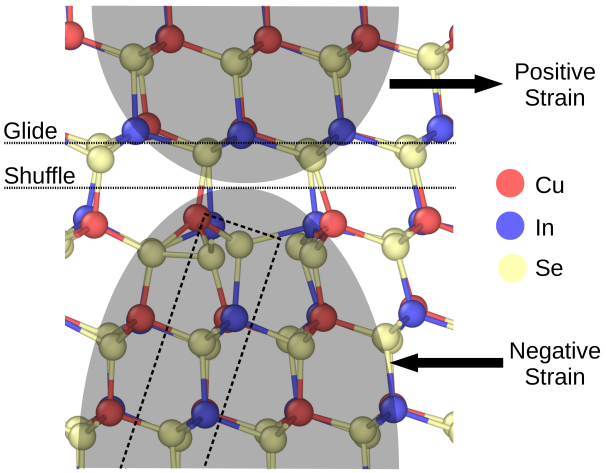

FIG 42.: Example of a 60°-mixed dislocation cores in the chalcopyrite structure (Glide β-core in CISe) with its distinctive inserted half-plane indicated by a dashed line box. Shaded areas point out the positive and negative strain regions associated to the core. Copper, Indium/Gallium and selenium are shown in red, blue and yellow, respectively.

of a second Ga_{In} segregating close to the glide β-core in $CuInSe_2$, we start with the supercell that contains one Ga_{In} in its prefered site. Although the used supercells are at the size limit of what can be accurately tackled with DFT, the periodic boundary conditions that must be satisfied. This implies that each Ga_{In} or Na_{Cu} included in the cell is actually a row of gallium or sodium atoms in the direction of the dislocation. Meaningful conclusions are still attainable since this artificial arrangement is in included in both energies, E_{near} and E_{far}.

Since Ga_{In} and Na_{Cu} are both neutral, their segregation tendency and pattern in the surroundings of the analyzed dislocation cores should be solely determined by their elastic interaction with the strain fields induced by the cores. As for the case of a Frank loop in Chapter 4, such interaction can be quantified by means of the EDT formalism introduced in Section 3.3.4, specifically Equation 3.17. We know that the formation energy of a defect would decrease only if the term $\sum_{\eta\zeta} G_{\eta\zeta}[D^q]u_{\eta\zeta}$ is positive. In order to estimate the values of the EDT for Ga_{In} and Na_{Cu} we follow the calculation scheme and corrections introduced in Sections 3.3.4 and 3.3.5 and we use the calculation setup described in Section 3.5.4. Furthermore, we applied a rotation operator to the obtained dipole tensors in order to be consistent with the coordinate system of the supercell containing the dislocation dipole under study.

In order to quantify the effect of segregating Ga_{In} or Na_{Cu} on the electrical activity of a given core, we analyze the position of the charge transition levels $\epsilon(q/q')$ as the segregation occurs. To that end we use the physically justified LDA/LDA+U extrapolation scheme proposed by Janotti *et al.* [208] and intro-

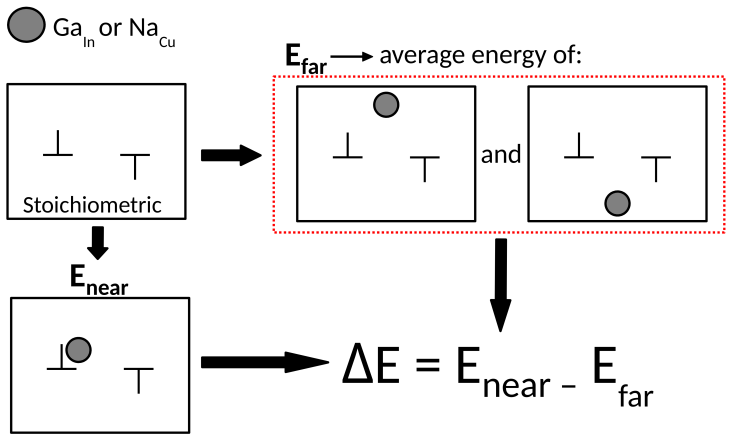

FIG 43.: Schematic illustration of the computational setup used to study Ga_{In} and Na_{Cu} segregation close to the electrically active cores in CISe and CGSe. When the segregating species are located in sites closer than 10 Å to the specific core under study, the corresponding energy is labeled E_{near}. Such calculation is performed for more than 15 copper or indium sites which are the closest to the analyzed core. The average of the energies when Ga_{In} or Na_{Cu} are located in the farthest possible sites they can occupy, we call it E_{far}. The difference, $\Delta E = E_{near} - E_{far}$, indicates whether Ga_{In} or Na_{Cu} prefer to be close or far from the core. This calculation cycle is carried out for up to three Ga_{In} or Na_{Cu} inside the supercell.

duced in Section 3.4.2 of this thesis. As discussed in Chapter 5, a given dislocation configuration is considered harmful if deep charge transition levels exist within the band gap. Such levels provide radiative or nonradiative recombination channels which deteriorate the device performance. [27] Therefore, if Ga_{In} or Na_{Cu} segregation has a beneficial effect on the properties of the active cores, the $\epsilon(q/q')$ transition level would become deeper by moving closer to the valence in the case of donor levels or to the conduction bands in the case of acceptor levels.

6.3 GALLIUM SEGREGATION

Using the calculation scheme described in the previous section, we find that gallium segregation to the core is indeed favored. Relaxed structures and atomic sites, where Ga_{In} is located are shown in Figure 44. The energy gain ΔE due to segregation for the configurations presented in Figure 44 are -0.13 eV, -0.12 eV and -0.1 eV for the cases of one, two and three segregated gallium atoms, respectively (see Table 4). Although such driving force would be too small to induce drastic changes in point defect concentrations, one has to consider that the gallium content in $CuIn_{1-x}Ga_xSe_2$ based solar cells is typically $x \sim 0.3$ [23]. Therefore, with Ga_{In} being as abundant, noticeable changes in the gallium distribution around dislocations can thus be expected. We notice also that the prefered

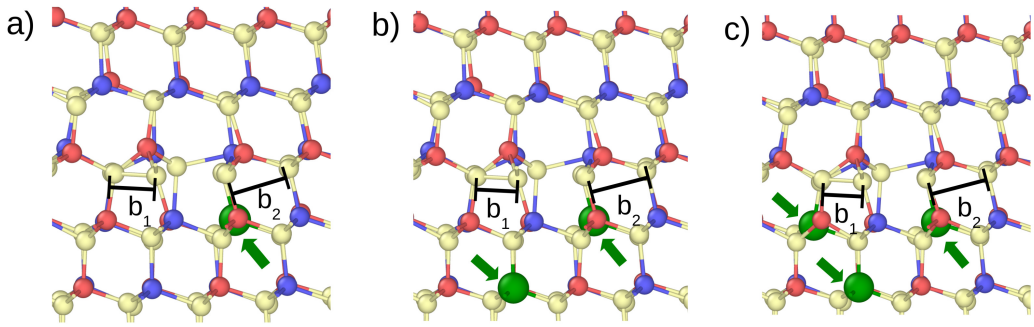

Figure 44.: Relaxed structures of the gallium decorated glide β-core in $CuInSe_2$ (b)-(d). Segregated gallium atoms in their preferred positions are shown in green and pointed out by means of green arrows. Color coding for the other atomic species is equal to the one used in Figure 42. Relevant "wrong" bonds b_1 and b_2, as reported in Section 5.2, are also marked.

positions are located in the region of negative strain (as shown in Figure 42). Furthermore, the energy gain ΔE for sites in the negatively strained region is consistently negative. On the other hand, ΔE for all investigated sites in the positively strained region are invariably positive. As mentioned in the previous section, since the Ga_{In} is neutral, this interesting behavior should be explained by its interaction with the strain field induced by the dislocation. Such hypothesis would be true if the components of $\mathbf{G}[Ga^0_{In}]$ are negative, i.e. $\sum_{\eta\zeta} G_{\eta\zeta}[D^q]u_{\eta\zeta}$ would be positive when the Ga_{In} is located in the negatively strained region. Thus, we calculate its $G_{\eta\zeta}$ in $CuInSe_2$ and obtained the following result:

$$\mathbf{G}[Ga^0_{In}] = \begin{pmatrix} -4.3 & 0 & 0 \\ 0 & -4.3 & 0 \\ 0 & 0 & -1.93 \end{pmatrix} \text{eV}$$

As we can see, the diagonal components of the defect dipole tensor of Ga_{In} are negative. This is caused by the smaller effective ionic radius of gallium (0.062 nm) compared to the case of indium (0.081 nm). [246] If we would assume 1% volumetric strain close to the core, the excess energy is about 0.1 eV. This is pretty much in line with the directly calculated values.

One further consequence of Ga_{In} in $CuInSe_2$ prefering the negatively strained region of the glide β-core, is that they would occur close to the ending of the inserted half-plane. It is in this region of the core where the "wrong" bonds b_1 and b_2 are located, which define the core electrical activity as we found out in Chapter 5. Due to this proximity, it is expected that gallium segregation would significantly alter the strength (length) of the relevant wrong bonds located in this core and as a consequence, modify its electrical properties. In Table 4 we

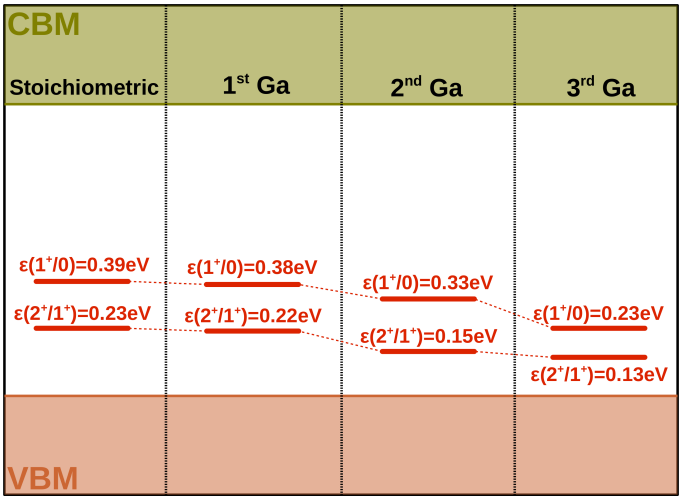

Figure 45.: Charge transition levels, $\epsilon(q/q')$, associated with the stoichiometric and gallium decorated glide β-core in CISe.

report the length of the relevant "wrong" bonds as gallium segregation occurs. We find that both, b_1 and b_2, increase their length due to this segregation and are therefore weakened during the process. These findings suggest that gallium atoms could indeed have a rather strong effect on the electrical activity of the glide β-core in $CuInSe_2$.

In order to support this last conjecture, we study the effect of such segregation on the position of the $\epsilon(q/q')$ transition level induced by this core. The obtained results are presented in Fig. 45 where we notice that both $\epsilon(2^+/1^+)$ and $\epsilon(1^+/0)$ move towards the valence band and become deeper as gallium segregation occurs. Being donor levels, this finding means that $\epsilon(q/q')$ induced by this core are passivated by gallium segregation. This confirms what we implied in our structural analysis: as a consequence of "wrong" bond weakening, the electrical properties of the glide β-core in $CuInSe_2$ are strongly and possitively affected by the presence of gallium atoms. Thus, addressing our initial question, the β-

	Stochiometric	1^{st}Ga	2^{nd}Ga	3^{rd}Ga
ΔE (eV)	-	-0.13	-0.12	-0.1
b_1 (Å)	2.45	2.46	2.46	2.49
b_2 (Å)	3.45	3.57	3.6	3.68

TABLE 4.: ΔE's for up to three Ga_{In} in their preferred segregation sites when close to the glide β-core in $CuInSe_2$ and lenght of the b_1 and b_2 "wrong" bonds present in this core.

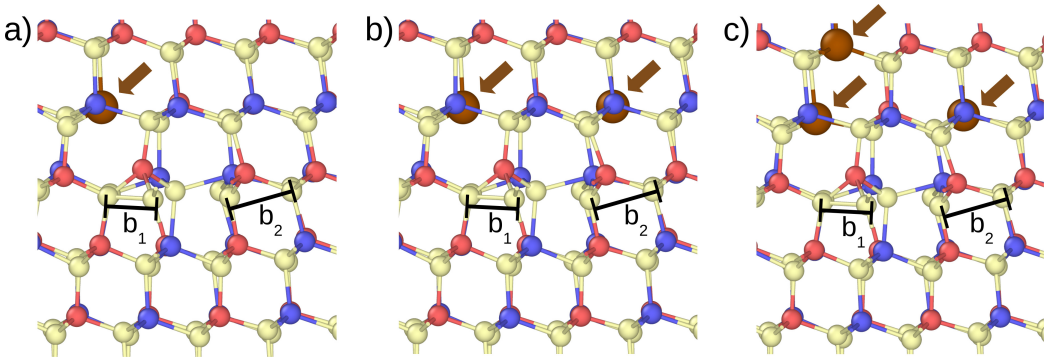

Figure 46.: Relaxed structures of the (a)-(c) sodium decorated glide β-core in $CuInSe_2$. Segregated sodium atoms in their preferred positions are shown in brown and pointed out by means of brown arrows. Color coding for the other atomic species is equal to the one used in Figure 42. Relevant "wrong" bonds as reported in Section 5.2, are also marked.

cores in CIGSe are expected to have milder recombination effects compared to the situation in $CuInSe_2$.

6.4 SODIUM SEGREGATION

As mentioned before, we study the segregation of Ga_{In} only in the surroundings of the glide β-core in $CuInSe_2$, but in the case of Na_{Cu} case, we focus on all active dislocation cores in $CuInSe_2$ and $CuGaSe_2$. In order to allow a straightforward comparison between the effects of both species, we will put special attention to the sodium segregation close to the glide β-core in $CuInSe_2$. As we will see, conclusions reached are common to all other electrically active cores for which Na_{Cu} segregation was considered.

Our analysis starts by assessing the segregation tendency of Na_{Cu} by means of the strategy presented in Section 6.2. Relaxed structures and atomic sites where the Na_{Cu} would prefer to be located when segregating close to the glide β-core in $CuInSe_2$ are shown in Figure 46. The ΔE for the configurations presented in the figure are -0.57 eV, -0.35 eV and -0.29 eV for the cases of one, two and three segregated gallium atoms, respectively (see Table 5). We notice also that, contrary to what was proposed in the model of Dietrich *et al.* [13] and to what we found for gallium, the prefered positions of Na_{Cu} in this core are all located whithin the positively strained region (as shown in Figure 42). Furthermore, ΔE in the case of sites in the positively strained region are invariably negative. On the other hand, we found that ΔE for sites in the negatively strained region are consistently positive. As can be seen in Figure 47, this segregation pattern is also seen in the case of the other electrically active cores in $CuInSe_2$ and $CuGaSe_2$.

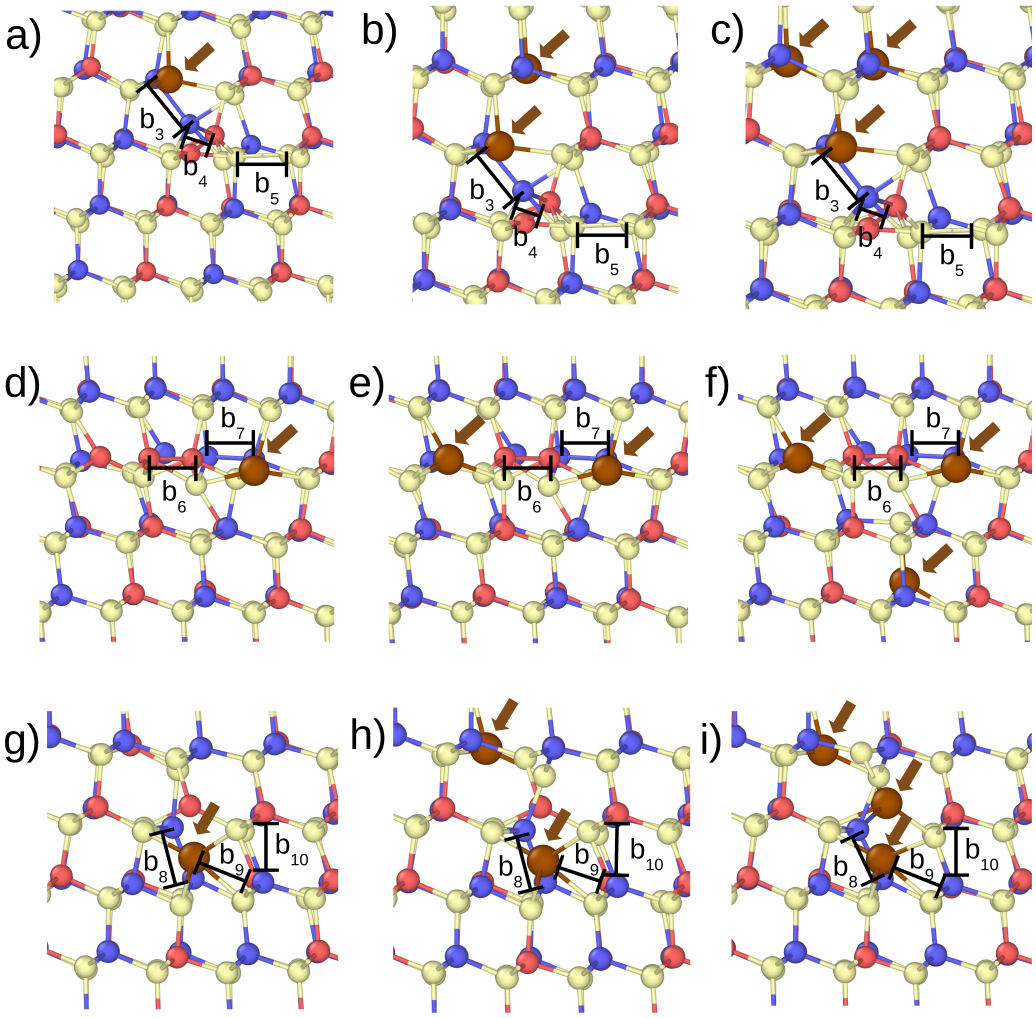

Figure 47.: Relaxed structures of the sodium decorated (a)-(c) shuffle α-core in $CuInSe_2$, (d)-(f) glide α-core in $CuGaSe_2$ and (g)-(i) shuffle α-core in $CuGaSe_2$. Segregated sodium atoms in their preferred positions are shown in brown and pointed out by means of brown arrows. Color coding for the other atomic species is equal to the one used in Figure 42. Relevant "wrong" bonds as reported in Section 5.2, are also marked.

Being also neutral one would expect that, as we found in the case of Ga_{In}, the driving force for the segregation of Na_{Cu} would be its elastic interaction with the strain field induced by the dislocation cores. As explained in Section 6.2 and applied in Section 6.3, this hypothesis can be tested by means of the $\mathbf{G}[Na^0_{Cu}]$. The elastic dipole tensor obtained for this defect in $CuInSe_2$ is:

$$\mathbf{G}[Na^0_{Cu}] = \begin{pmatrix} 8.62 & 0 & 0 \\ 0 & 8.62 & 0 \\ 0 & 0 & 11.85 \end{pmatrix} \text{eV}$$

And in the case of Na_{Cu} in $CuGaSe_2$, it is:

$$\mathbf{G}[Na^0_{Cu}] = \begin{pmatrix} 7.6 & 0 & 0 \\ 0 & 7.6 & 0 \\ 0 & 0 & 6.08 \end{pmatrix} \text{eV}$$

These results imply that Na_{Cu} prefers to segregate into positively strained regions, confirming that its segregation is strain driven segregation and correctly describe the segregation pattern predicted from our direct calculations. The reason why the $G_{\eta\zeta}$'s for this defect are positive is the larger effective ionic radius of sodium compared with its copper counterpart (0.1 nm for the former and 0.077 nm for the later). [246] We notice that the magnitude of the components $G_{\eta\zeta}$'s obtained for the case of Ga_{In} are smaller than the ones found for Na_{Cu}. This feature is caused by the larger difference in ion sizes between sodium and indium than the one there is between gallium and indium.

Since the Na_{Cu}'s prefer the positively strained region of the electrically active cores in $CuInSe_2$ and $CuGaSe_2$, sodium segregation would occur far from the ending of the inserted half-plane. As mentioned before, it is in this region of the core where the "wrong" bonds, which define the core electrical activity, are located. Consequently, sodium segregation would be expected not to significantly alter the strength (length) of the relevant "wrong" bonds. Thus, it would not modify the electrical properties of this core. These observations regarding the effect of sodium segregation on the strenght of the wrong bonds are common to all four active cores in $CuInSe_2$ and $CuGaSe_2$. This holds even in the case of the shuffle α-core in $CuGaSe_2$, for which the first segregating sodium atom segregates at the termination of the inserted half-plane as can be seen in Figure 47(g). In Tables 5, 6, 7 and 8 we explicitly report the length of the relevant "wrong" bonds as sodium segregation occurs into the electrically active dislocation cores in $CuInSe_2$ and $CuGaSe_2$. We found that contrary to the case of Ga_{In}, the relevant "wrong" bonds in the cores are unchanged by this segregation process. For example, in the specific case of the glide β-core in $CuInSe_2$, we found that both b_1 and b_2, the relevant "wrong" bonds in this core, are unchanged by the segregation process. Even when three sodium atoms are inside the core, the change in the bonds amount to 0.4% and 3% for the b_1 and b_2 "wrong" bonds, respectively. These findings suggest that sodium atoms could have a rather weak effect on the electrical properties of the active cores in $CuInSe_2$ and $CuGaSe_2$.

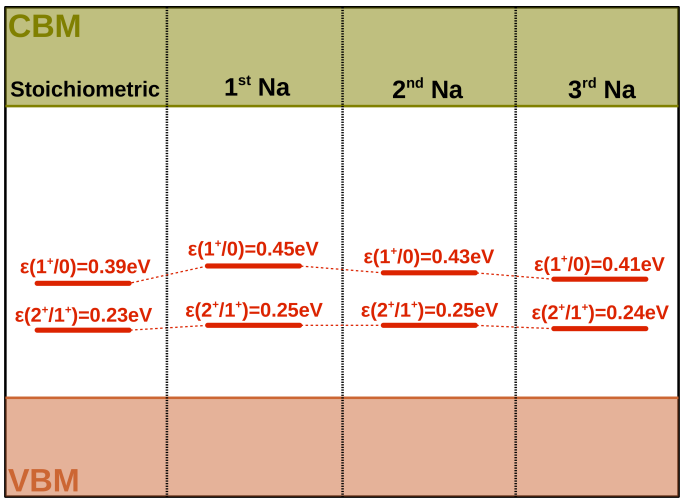

Figure 48.: Charge transition levels, $\epsilon(q/q')$, associated with the stoichiometric and sodium decorated glide β-core in $CuInSe_2$.

To confirm whether this is true, we use once more the LDA/LDA+U method presented in Section 3.4.2 to study how the position of the $\epsilon(q/q')$ change as sodium segregation occurs. At this point, a short discussion for the individual cores under study is valuable. For the glide β-core in $CuInSe_2$, shown in detail in Figure 48, we notice that both $\epsilon(2^+/1^+)$ and $\epsilon(1^+/0)$ are essentially unaffected by the sodium segregation (the maximum change in their position amounts to less than 6% of the experimental bang gap of $CuInSe_2$). In the specific case of the shuffle α-core in $CuInSe_2$, its strongest "wrong" bond as reported in Table 6, b_3, is unaffected by the segregation process. Consequently, inline with was what stated before, this core is also not expected to be passivated by the presence of sodium. Proof of this is provided in Figure 49(a). As we can see there, the two deepest and more relevant levels do not move due to the presence of the Na_{Cu}'s. Interestingly, the level $\epsilon(3^-/4^-)$ disappears into the conduction band as soon as the segregation starts. This is caused by the weakening of the "wrong" bond b_4 as reported in Table 6.

	Stochiometric	1^{st}Na	2^{nd}Na	3^{rd}Na
ΔE (eV)	-	-0.57	-0.35	-0.29
b_1 (Å)	2.45	2.47	2.46	2.46
b_2 (Å)	3.45	3.45	3.51	3.55

Table 5.: ΔE for up to three Na_{In} in their preferred segregation sites when close to the glide β-core in $CuInSe_2$ and length of the b_1 and b_2 "wrong" bonds present in this core.

	Stochiometric	1st Na	2nd Na	3rd Na
ΔE (eV)	-	-0.73	-0.49	-0.44
b_3 (Å)	2.82	2.83	2.83	2.79
b_4 (Å)	3.01	3.15	3.12	3.09
b_5 (Å)	3.22	3.23	3.24	3.23

Table 6.: ΔE's for up to three Na_{Cu} in their preferred segregation sites when close to the shuffle α-core in $CuInSe_2$ and lenght of the b_3, b_4 and b_5 "wrong" bonds present in this core.

	Stochiometric	1st Na	2nd Na	3rd Na
ΔE (eV)	-	-0.59	-0.79	-0.53
b_6 (Å)	2.35	2.45	2.48	2.49
b_7 (Å)	2.38	2.39	2.39	2.39

Table 7.: ΔE's for up to three Na_{Cu} in their preferred segregation sites when close to the glide α-core in $CuGaSe_2$ and lenght of the b_6 and b_7 "wrong" bonds present in this core.

Let us now focus on the electrically active cores in $CuGaSe_2$. For the glide α-core we found that both "wrong" bonds, b_6 and b_7, are unaffected as the Na_{Cu} accumulates in the surroundings of the core as detailed in Table 7. When analyzing the position of the charge transition levels induced by this core as the sodium segregation occurs, Figure 49(b), we can see that although the $\epsilon(0/2^-)$ level moves slightly, its deep nature is not modified. Finally, for the shuffle α-core in $CuGaSe_2$ we found that two "wrong" bonds, b_9 and b_{10} in Figures 47(g)-(i), observed in its stoichiometric configuration no longer exist when sodium segregation occurs. In the case of b_9, its disapearance is caused by the Na_{Cu} which segregates at the termination of the inserted half-plane. This last feature is in contrast to what was found for the other cores, where all Na_{Cu} segregated into the positively strained regions. Although unexpected to prefer such position, its effect on the electrical properties of the core remains limited as it will be shown shortly. It is puzzling that the ΔE calculated for the first Na_{Cu}, which segregates at the termination of the inserted half-plane, is the largest found in this study. Such strong effect is caused by the fact that, as mentioned before, this Na_{Cu} breaks the b_9 wrong bond observed in the stoichiometric configuration. Nevertheless, as reported in Table 8, the strongest "wrong" bond, b_8, is unaffected by the segregation process. Consequently, as we can see in Figure 49(c), the deepest and more relevant charge transition level do not move due to the presence of the

	Stochiometric	1^{st}Na	2^{nd}Na	3^{rd}Na
ΔE (eV)	-	-1.08	-0.635	-0.583
b_8 (Å)	2.47	2.48	2.46	2.47
b_9 (Å)	2.50	-	-	-
b_{10} (Å)	2.57	3.37	3.37	3.53

Table 8.: ΔE's for up to three Na_{Cu} in their preferred segregation sites when close to the shuffle α-core in $CuGaSe_2$ and lenght of the b_8, b_9 and b_{10} "wrong" bonds present in the stoichiometric version of this core.

Na_{Cu}'s. Nonetheless, the $\epsilon(2^-/3^-)$ level disappears into the conduction band as soon as the segregation starts. Such behavior is caused by the break of both b_9 and b_{10} which takes place as the Na_{Cu}'s segregate into this core.

6.5 SUMMARY

In conclusion, we investigated the effect of gallium and sodium segregation on the structure and the electronic properties of the electrically active cores in $CuInSe_2$ and $CuGaSe_2$. In the case of gallium, we studied the interaction of Ga_{In} with the glide β-core in $CuInSe_2$. Since this structure is electrically active in $CuInSe_2$ but inactive in $CuGaSe_2$, our density functional theory based study sheds light on the properties of this line defect in the technologically relevant Cu(In,Ga)Se_2. We found that Ga_{In} segregation occurs into the negatively strained region close to the core. Furthermore, we conclude that such process is strain driven, which explains the asymmetry of the segregation. We also show that the presence of Ga_{In} close to the core under study, weakens the "wrong" bonds within the core. Finally, we calculated the charge transition levels of the glide β-core in $CuInSe_2$ with one, two and three Ga_{In} and found out that they become shallower as the presence of gallium increases. These results prove the beneficial effect of gallium segregation passivating electrically active β-cores in $CuInSe_2$ and allow us to conclude that such core type, either glide or shuffle, would be inactive in Cu(In,Ga)Se_2. Furthermore, in the same way as dislocation induced deep defects states can be generated solely due to strain [228], our findings provide evidence that electrically active dislocations can be passivated by segregation of electrically inactive species.

In the case of sodium, we studied its interaction with all electrically active cores in both $CuInSe_2$ ands $CuGaSe_2$. We found that sodium do segregates into the positively strained region close to these cores. Analogous to gallium segregation, our elastic dipole results show that such process is strain driven. Regarding the effects of sodium on the properties of the active cores, we showed that the

relevant "wrong" bonds present in these cores are not affected by the presence of Na_{Cu}. As a consequence, sodium segregation is not expected to be a passivating agent of dislocations in $CuInSe_2$ and $CuGaSe_2$. To prove this hypothesis, we calculated the charge transition levels of the dislocation cores decorated with up to three Na_{Cu} and found out that their position within the band gap is stable as the segregation occurs. These results rule out the experimentally observed sodium segregation close to dislocation cores in Cu(In,Ga)Se_2, as solution to the puzzle of the apparent harmless nature of dislocations in Cu(In,Ga)Se_2.

Nevertheless, the results we presented in this chapter and in Chapter 5 provide evidence that depending on the termination of the inserted half-plane, the stoichiometric or sodium decorated 60°-mixed dislocation cores in Cu(In,Ga)Se_2 are either electrically active (α-cores) or inactive (β-cores). In other words, the termination of the inserted half-plane defines whether they accumulate charge or not. Therefore, our findings are in agreement with was reported by Dietrich *et al.* [13], where it was pointed out that not all dislocations they studied exhibited potential wells.

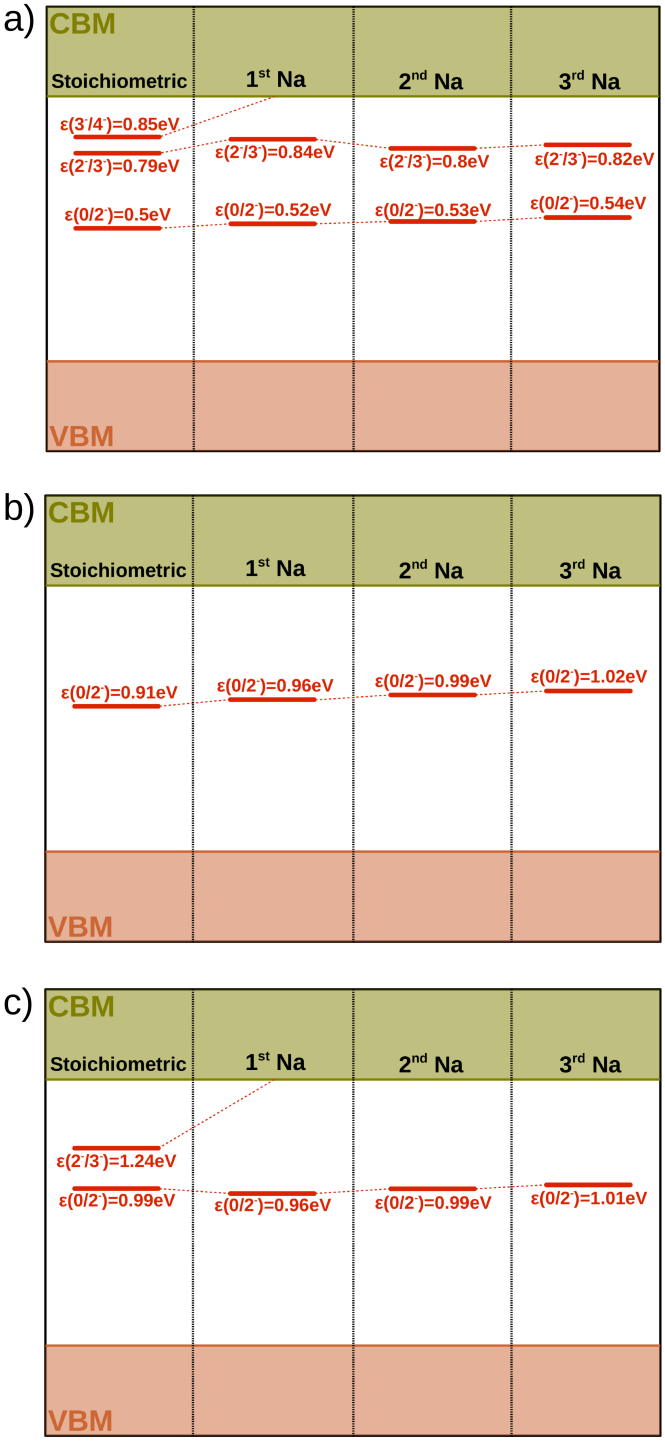

Figure 49.: Charge transition levels, $\epsilon(q/q')$, associated with the stoichiometric and sodium decorated (a) shuffle α-core in $CuInSe_2$, (b) glide α-core in $CuGaSe_2$ and (b) shuffle α-core in $CuGaSe_2$.

Part IV

CONCLUSION

SUMMARY

In the present thesis we carried out the first complete theoretical study of the structural and electronic properties of Frank loops and perfect dislocations in $CuInSe_2$ and $CuGaSe_2$. We aimed at solving the puzzle of $Cu(In,Ga)Se_2$-based solar cells which exhibit decent efficiencies and at the same time have a very high dislocation density. Furthermore, based on our study of Frank partials, we shed some light on the physical mechanism behind the beneficial effect of the Cu-rich stage of the three stage co-evaporation process. Our key findings are summarized below:

- It was found that stoichiometric Frank partials induce defect states and are expected to be electrically active. This is so despite the fact that α- and β-cores are fully coordinated structures. It is found that defect states are strain induced.

- Frank partials prefer to be decorated and favor a configuration with excess in copper in their cores. Such copper excess is expected to be higher in the α-core because inside that structure the Cu_{In}^{0} antisites have a negative formation energy and therefore may form spontaneously. On the other hand, β-cores exhibit slight Cu excess associated with the presence of both Cu_{In} and Cu interstitials, which have low positive formation energies inside that core.

- Besides chemical changes inside the cores, Frank partials induce the formation of copper clouds in their surroundings. Our simulations provide evidence that such clouds are formed by accumulation of Cu_{In}^{-2} antisites.

- Since the cores of Frank partials are fully coordinated, no electrostatic interaction with point defects is expected. Using a linear elasticity-based approach, namely the elastic dipole tensor, we were able to reproduce the experimentally observed atomic rearrangements in the surroundings of the Frank partials. This finding proves that strain is the driving force for the formation of the copper clouds.

- The Cu_{In} antisite, which accumulates inside the cores and in the copper clouds, is widely acknowledged as the most harmful trap in $Cu(In,Ga)Se_2$. Therefore, the decorated Frank partials are expected to be highly detrimental, if present in a functioning device. Since the Cu-rich stage in the three-stage co-evaporation growth process is known to induce a reduction

in planar defects, its beneficial effect could be, at least partially, accounted for if this stage is able to eliminate the Frank loops.

- Perfect screw dislocations are found to be electrically inactive in $CuInSe_2$ and $CuGaSe_2$. On the other hand, most of the perfect 60°-mixed dislocations in these materials exhibit deep levels in the gap. By means of a Bader charge analysis we found out that all α-cores are active and induce deep acceptor levels. Regarding the β-cores, only the glide configuration in $CuInSe_2$ exhibits deep donor levels.

- Based on the atomic orbital theory, we proved that deep defect states induced by the 60°-mixed dislocation cores are caused by the presence of cation-cation or anion-anion "wrong" bonds observed in the relaxed cores.

- Since all α-cores are active in both $CuInSe_2$ and $CuGaSe_2$, we can conclude they would also be active in the $Cu(In,Ga)Se_2$ semiconductor alloy. However, since only one β-core is electrically active, such conclusion is not straightforward in their case. Our strategy was to analyze the effect of gallium atoms segregating into the electrically active β-core. We found out that gallium segregation passivates this core, i.e we can conclude that β-cores are inactive in $Cu(In,Ga)Se_2$.

- We found evidence that sodium prefers to segregate into the dislocation cores in both $CuInSe_2$ and $CuGaSe_2$. Furthermore, we proved that such segregation is strain driven. However, contrary to what have been suggested in literature, sodium does not have influence on the electrical properties of the 60°-mixed dislocations in $CuInSe_2$ and $CuGaSe_2$. Specifically, a recent model assumed that sodium atoms would segregate into the termination of the inserted half-plane of these dislocations. However, the strain that drives the interaction prevents sodium segregation into that position inside the cores.

- Our results provide evidence that depending on the termination of the inserted half-plane, the stoichiometric or sodium decorated 60°-mixed dislocation cores in $Cu(In,Ga)Se_2$ are either electrically active (α-cores) or inactive (β-cores). In other words, the termination of the inserted half-plane defines whether they accumulate charge or not. Therefore, our findings are in agreement with was reported by Dietrich *et al.* [13], where it was pointed out that not all dislocations they studied exhibited potential wells.

OUTLOOK

Science is a human endeavor characterized by a permanent state of doubt. This means that in a healthy scientific effort, once questions are answered new ones arise. The research presented in this thesis is not exempt of such dynamic and thus we point out some issues which could serve as the basis of future studies.

In Chapter 4 we succesfully studied the structural and electronic properties of Frank partials. Based on their sessile nature one can conclude that the dislocation loops they bound are growth accidents. However, conclusions on that matter cannot be drawn easily for the perfect dislocations we studied in Chapters 5 and 6. In order to answer such a question and check whether dislocation presence in Cu(In,Ga)Se_2 is associated with gallium gradients as proposed by Dietrich *et al.* [11, 12], we would have to perform accurate simulations of the growth process of Cu(In,Ga)Se_2 thin-films. Unfortunately, the size of the systems needed in those calculations makes it unfeasible to use DFT. Nevertheless, results presented in Chapters 5 and 6 can be used to fit an interatomic potential which would open the possibility of reliable simulations of Cu(In,Ga)Se_2 thin-film growth to be carried out, in the spirit of what has been done for CdTe [247–252].

Regarding the electronic properties of perfect dislocations, in Chapters 5 and 6 of this thesis we proved stoichiometric β-cores in Cu(In,Ga)Se_2 are electrically inactive. On the other hand, stoichiometric and sodium decorated α-cores are expected to be harmful. If the latter would be the preferred configuration, our results would be clearly in contrast with the experimental observations of high dislocation densities existing in Cu(In,Ga)Se_2-based devices with decent effiencies. However, since we cannot separate the energy of a given dislocation dipole into the energy contributions of the α- and β-core contained in the supercell, we cannot conclude from our results which core type is the preferred one. To overcome this issue it would be necessary to simulate individual dislocations, which is imposible using the supercell approach. One way to circunvent this problem would be to use clusters or flexible boundary conditions [164]. Furthermore, if the interatomic potential mentioned in the previous paragraph would be available, it would be possible to apply the strategy used by Kweon *et al.* [253] to study perfect dislocations in CdTe. In there, the authors simulated a large supercell containing a periodic arrangement of perfect dislocations by means of molecular dynamics. Afterwards, a section of this structure containing a single dislocation is extracted and used as input for further cluster-based DFT calculations. Despite allowing one to study single dislocations, both the cluster and flexible boundary conditions approaches have the drawbacks. The former does not allow for a full development of the core field unless extremely large systems are studied and in

the latter one encounters difficulties when trying to separate the excess energy between the dislocation and the external boundary conditions [164].

As we pointed out throughout this thesis, the answer to the puzzle of high dislocation densities in devices Cu(In,Ga)Se_2-based devices with decent efficiencies could arise from the passivation of the electrically active cores caused by point defects segregation. In the case of perfect dislocations, we intentionally focused on the segregation of neutral species and did not addressed the case of charged intrinsic point defects, despite the fundamental role they play in the properties of Cu(In,Ga)Se_2-based devices. The reason for this lies in the fact that both point defects and perfect α-cores in this material prefer to be charged (in contrast to the neutral Frank partials studied in Chapter 4). Therefore, they would compete for the extra holes or electrons introduced in the supercell used to study their interaction. Since there is no way to force the system to distribute the charges in the correct fashion, such calculations would not be able to deliver unambiguous results for definite charge states. For example, let us assume that a supercell containing a shuffle α-core in $CuInSe_2$ and a V_{Cu} is charged with three electrons. The vacancy is a shallow acceptor and prefers to be charged with one extra electron for all values of the E_F. In this case the remaining two electrons would be accomodated in the dislocation core and we would have a sensible distribution of the extra charge carriers. However, this dislocation can also accomodate all three electrons. In such case we would study the interaction between a neutral copper vacancy, which is non-existent in this material, and a charged dislocation which results in the simulation of a meaningless scenario. This issue could be investigated by means of an independent and elaborated calculation of both the elastic and the electrostatic interaction between the point and linear defects of interest. Naturally, a realistic calculations should be fed by an accurate model of the charge distribution of both defect types.

Part V

APPENDIX

A

SOLAR CELLS: PRINCIPLES AND LIMITATIONS

A.1 INTRODUCTION

Semiconductor solar cells are solid-state devices with the ability to transform light into electricity by means of a quantum process, namely the photovoltaic effect [17, 18, 29, 30]. Therefore, even in the case of the conceptually simplest device, to fully account for their properties we require concepts of solid state physics, quantum mechanics and statistical physics. In this appendix, we present a brief introduction to the working principle of semiconductor solar cells along with the physical origin of their efficiency limits.

By no means this short appendix attempts to be a comprehensive treatise on a complex topic like the physics of solar cells. For detailed discussions on the matter we recommend the books of Würfel [17] and Bauer [18] which approach the subject from a thermodynamic point of view and the book by Smets *et al.* [29] which goes from the basic physics up to the design of photovolatic systems. There is also the already classic text from Nelson [30] which approaches the subject using concepts from semiconductor physics. Finally, Boriskina *et al.* [254] reviewed the state of the art in optical energy conversion, including conceptual breakthroughs that go beyond conventional concentrating optics and material design.

A.2 THE WORKING PRINCIPLE AND LIMITS OF A SOLAR CELL

The generation of an electric potential difference at the terminals of a solar cell is caused by the *photovoltaic effect*. As presented by Smets *et al.* [29], the essential physics of this phenomenon can be included in the simple model shown in Figure 50a. In there, among other details, it is possible to see a depiction of the three basic processes in which the *photovoltaic effect* can be divided in, namely:

- **Generation of electron-hole pairs due to the absorption of photons.** When a photon with energy $E_{ph} = h\nu$ is absorbed by a material, it excites an electron from an initial energy level E_i to a final energy level E_f. This is shown in Figure 50a for an ideal semiconductor with flat valence

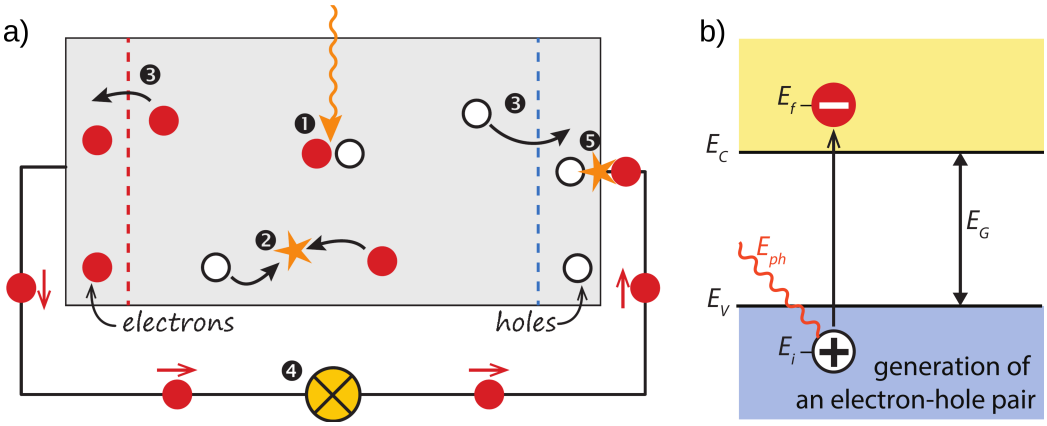

Figure 50.: Model of a solar cell with a depiction of the relevant process behind the *photovoltaic effect* (a) and an schematic of the absorption of a photon in a semiconductor (b). In there E_v, E_c, E_G (equal to $E_c - E_v$) stand for the valence and conduction band edges and the bandgap, respectively. (Adapted from Ref. [255],)

(VB) and conduction (CB) bands. The excited electron going from the VB to the CB leave behind a positively charged hole in the former. This process is denoted as ❶ in Figure 50b.

- **Separation of the photo-generated charge carrier pairs.** If left alone, the electron-hole pair will eventually recombine. This process is denoted as ❷ in Figure 50b, either in a radiative or non-radiative fashion. In Figure 51, it is possible to see the basic recombination mechanisms of the photo-generated electron-hole pairs. When radiative recombination occurs, the excess energy of the recombining pair is emitted in the form of a photon with energy $h\nu$, with h being the Planck's constant and ν being the frequency of the photon. On the other hand, no photon is involved in non-radiative recombinations. One example of this second type of recombination processes is the Auger recombination, where the excess energy is transfered to a third charge carrier, either electron or hole. This excited carrier relaxes into the conduction band edge E_c if it is an electron and into the valence band edge E_v if it is a hole. Such relaxation is called thermalization and phonons with energies $\hbar\omega$ are emitted while it occurs (where $\hbar$ is the reduced Planck's constant and ω is the characteristic frequency of a given phonon mode). Another non-radiative recombination mechanism is the SRH process, which involves defect-induced states in the forbidden gap and the emission of phonons. If any of these radiative or non-radiative

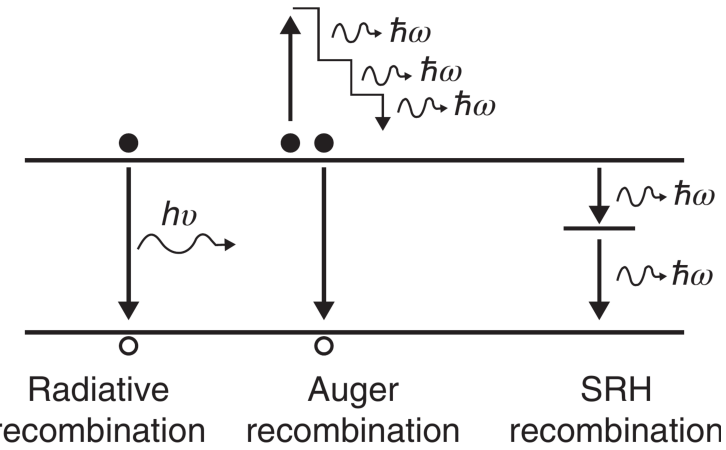

Figure 51.: Schematic of the three basic recombination mechanisms of photogenerated charge-carriers in a semiconductor. (From Ref. [38], *©WILEY-VCH Verlag GmbH & Co. KGaA*, reprint with permission).

recombination mechanisms occur, no electric potential is generated from a given electron-hole pair. Therefore, it is needed to bring the electron-hole pair apart before they recombine. To achive this, the solar cell must contain two *semipermeable membranes*, one permeable only to electrons (dashed vertical red line in Figure 50b) and the other only to holes (dashed vertical blue line in Figure 50b). Once the electrons and holes cross the membranes,which is the process denoted as ❸ in Figure 50b, the charge carriers are effectively separated. Their accumulation on the sides of the solar cell causes the generation of the electric potential at the terminals of the solar cell.

- **Collection of the separated charge carriers.** When connected to an external circuit charge carriers are extracted from the device, which is the process denoted by ❹ in Figure 50b. After passing through the circuit, electron and holes recombine in one terminal of the device as indicated by process ❺ in Figure 50b.

The simplest semiconductor device which can achieve the essential step of separating the electron-hole pairs is the single p-n homojunction. Such structure consists of a p- and an n-type semiconductor put together and it is the elementary building block of most semiconductor electronic devices. Before discussing how this sytems separates the charges, let us take a glance at the behavior of isolated p- and n-type semiconductors as shown in the schematic in Figure 52a. In both cases the charge neutrality condition is satisfied. Therefore, in the case of an n-type semiconductor, the charge of the free electrons is compensated by the positively charged ionized donor atoms. Analogously, in a p-type semiconductor, the ionized acceptor atoms are negatively charged and they compensate for the

charge of the free holes. The band diagrams of isolated p- and n-doped semiconductors are presented in Figure 52b. In there, the band-gap and the Fermi level are denoted as $E_G = E_c - E_v$ and E_F, respectively. Furthermore, the vacuum energy level, *i.e.* the energy of a free stationary electron just outside of the material, is aligned in both diagrams. The position of E_F depends on the dopants nature and concentration.

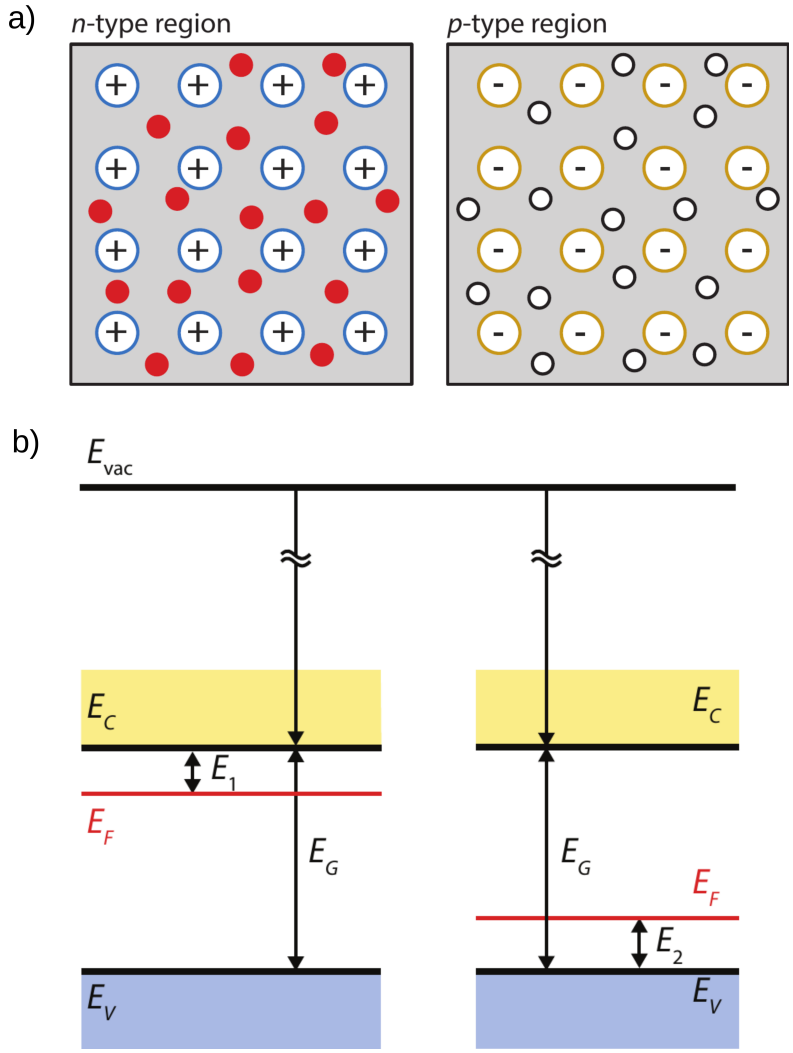

Figure 52.: Schematic of isolated p-type and n-type semiconductors showing the charges associated with free carriers and ionized dopants for each case (a) and the energy diagrams of the same isolated systems (b). In there, E_{vac} stands for the vacuum energy level. (Adapted from Ref. [255], ©2014 *by Arno Smets and Klaus Jäger and Olindo Isabella and Rene van Swaaij and Miro Zeman, available under the terms and conditions of the Creative Commons Attribution 4.0 License* `https://creativecommons.org/licenses/by-nc-sa/4.0/`)

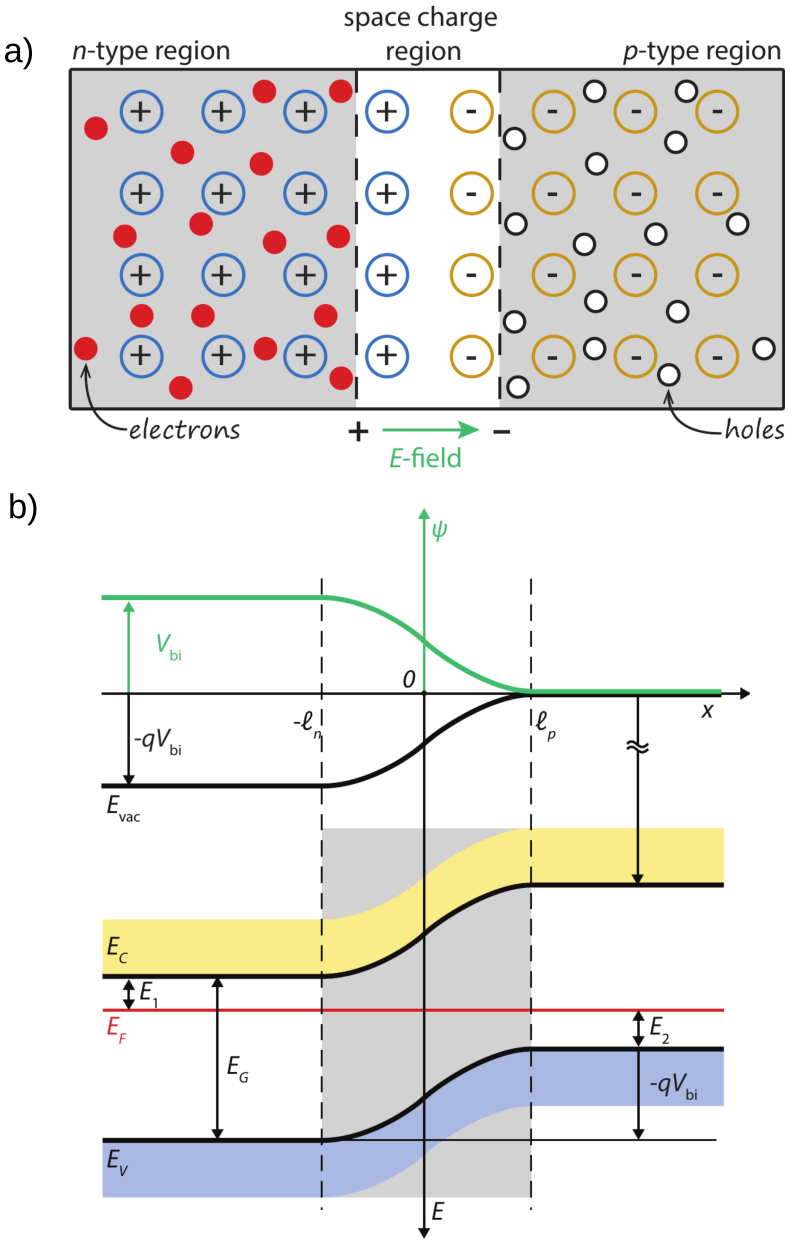

Figure 53.: Schematic of an ideal p-n junction including its *space-charge* region and the field associated with it pointed out by a green arrow (a) and the energy diagrams of the junction (b). In there, V_{bi} stands for the *built-in* potential and q is the elementary charge. (Adapted from Ref. [255], ©2014 *by Arno Smets and Klaus Jäger and Olindo Isabella and Rene van Swaaij and Miro Zeman, available under the terms and conditions of the Creative Commons Attribution 4.0 License* `https://creativecommons.org/licenses/by-nc-sa/4.0/`)

When the actual p-n junction is formed, the picture changes dramatically. The schematic in Figure 53a depicts how a region without free electrons or holes is formed in the surroundings of the interface. Such region is called *space-charge* or depleted region and is created by diffusion of holes from the p-type material to the n-type side of the junction where they recombine, and of electrons from the n-type to the p-type side of the junction where they also recombine. As free carriers in this region diffuse and recombine, uncompensated ionized dopant atoms are left behind (positively charged in the n-type material and negatively charged for the p-type material). Consequently, an electric field is induced within the junction directed from the n-type side of the junction to the p-type side. The presence of this field creates a potential difference across the *space-charge* region: the so-called *built-in* potential V_{bi} (the green curve in Figure 53b). Due to the electric field and potential, holes will experience a force in the direction of the field, driving them into the p-type semiconductor, while electrons will be forced to move in the opposite direction. Therefore, such field caused by the rearrangement of charges effectively separates the electron-hole pairs. This is the working principle of a solar cell.

Further details can be learned from the band diagram of the p-n junction in equilibrium as shown in Figure 53b. In contrast to the case of the isolated p- and an n-type semiconductor, E_F is constant across the p-n junction. This alignment of the Fermi energy means that there is an offset in the band edges, E_v and E_c, outside the space-charge region, in the so-called *quasi-neutral* region. However, since bands must be continuous across the junction, they get bended as can be seen in Figure 53b. The offset between a given band edge in the p-type and its counterpart in the n-type semiconductor is equal to $-eV_{bi}$ (with e being the elementary charge). From this point of view, the separation of charges is caused by a change in the electric potential energy. A positively charged hole would move to the highest available state in the VB while an electron would go to the lowest available point in the CB. This is the reason why it is said that in a band diagram holes float and electrons sink.

The energy conversion efficiency of a such homojunction was first studied by Shockley and Queisser [19]. In its simplest form, their detailed balance analysis based study was based on the following assumptions:

(a) All photons with energies $E_{ph} \geq E_G$ are absorbed. On the other hand, the probability of absorption for photon with energies $E_{ph} < E_G$ is zero.

(b) One electron-hole pair generated per absorbed photon.

(c) All photogenerated charge carriers relax to the band edges by giving away the excess energy $E_{ph} - E_G$ to the lattice in the form of phonons. This process is called thermalization.

(d) When in short circuit, all electron-hole pairs are collected.

(e) Radiative recombination is the only energy loss beyond the non-absorbed photons in (a) and the thermalization in (c).

(f) The sample is illuminated with unconcentrated light.

For the derivation of the maximum conversion efficiency possible for a p-n homojunction we follow the ideas presented by Alharbi and Kais [256]. For a device that satisfies all the assumptions of the Shockley-Queisser model, the photo-generated current $J_{Gen}(E_G)$ is given by

$$J_{Gen}(E_G) = e \int_{E_G}^{\infty} \gamma(E_{ph}) \phi(E_{ph}) dE_{ph}, \tag{A.1}$$

where $\gamma(E_{ph})$ is the *multiplication factor* for a given photon energy E_{ph} (frequently referred to as *quantum efficiency*) and $\phi(E_{ph})$ is the radiation flux that reaches the solar cell. Although assumption (b) of the Shockley-Queisser approach means that $\gamma(E_{ph})$ is equal to 1, we will retain it in our equations to keep the derivation general. Let us now focus on the current $J_{Rec}(E_G, V, T)$ associated with the radiative recombination which, being a spontaneous emission, is governed by the generalized blackbody radiation

$$J_{Rec}(E_G, V, T) = e \int_{E_G}^{\infty} \phi_{bb}(E_{ph}, T) \exp\left(\frac{eV}{kT}\right) dE_{ph}, \tag{A.2}$$

where $\phi_{bb}(E_{ph}, T)$ is the blackbody spectrum at temperature T, the temperature of the device, and V is the photo-generated voltage at the terminals of the cell. The net current $J(E_G, V, T)$ is what remains after the recombination current is substracted from the photo-generated current as

$$J(E_G, V, T) = J_{Gen}(E_G) - J_{Rec}(E_G, V, T). \tag{A.3}$$

Now we are in a position to evaluate the conversion efficiency $\eta(V)$ of a single p-n homojunction, which is nothing else than the ratio between the output power P_{out} and the input power P_{in}:

$$\eta(V) = \frac{P_{out}}{P_{in}} = \frac{V_m J_m}{P_{in}}, \tag{A.4}$$

where the subscript m denote the voltage and current for which the maximum power is reached and the input power P_{in} is given by

$$P_{in} = e \int_{0}^{\infty} E \phi(E_{ph}) dE_{ph}. \tag{A.5}$$

For a given E_G and T, the maximum possible conversion efficiency can be calculated by variating V. In order to fully understand the Shockley-Queisser limit, we focus now on the three efficiency loss sources in this model. The first efficiency loss source L_{unabs} is related to the unabsorbed photons with $E_{ph} < E_G$ and is given by

$$L_{unabs} = \frac{e}{P_{in}} \int_0^{E_G} E\phi(E_{ph}) dE. \tag{A.6}$$

The second efficiency loss source L_{th} appears when photogenerated charge carriers thermalize to the band edges by giving away the excess energy $E_{ph} - E_G$. This efficiency loss that can be expressed as

$$L_{th} = \frac{e}{P_{in}} \int_{E_G}^{\infty} (E - \gamma(E_{ph})E_G)\phi(E_{ph}) dE_{ph}. \tag{A.7}$$

Finally, the third efficiency loss source is recombination and is named L_r. This can be quantified in the following way

$$L_r = \frac{VJ_{Rec}}{P_{in}} + \frac{e}{P_{in}} \int_{E_G}^{\infty} (E_G - V)\phi(E_{ph}) dE_{ph}, \tag{A.8}$$

where the first term is the direct loss due to radiative recombination as discussed before and the second term accounts for a further thermalization due to the difference between E_G and the photo-generated voltage. Such voltage drop is caused by the electrical resistance of the path through which the photo-generated carriers arrive to the external circuit, including the resistance of the junction and the effect of leakage currents.

Based on this analysis, Alharbi and Kais [256] calculated the maximum conversion efficiency $\eta_{max}(V)$ along with the quantification of losses for a single p-n homojunction with respect to E_G. In Figure 54 results for room temperature ($T = 300$K) and no carrier multiplication ($\gamma(E_{ph}) = 1$) are shown. The radiation flux $\phi(E_{ph})$ used in such calculation is the flux associated with the AM1.5G global standard spectrum. The maximum conversion efficiency attainable under such conditions is equal to 33.3% for a semiconductor with a bandgap of 1.14eV, which is close to the bandgap of silicon. Fortunately, for E_G values between 0.91eV to 1.57eV maximum efficiencies above 30% are possible. Thus, material alternatives to fabricate solar cells are not restrained to a single E_G. One of these options is the Cu(In,Ga)Se_2 semiconductor alloy, which is at the heart of this thesis and is currently used in the solar cells with highest efficiencies among thin-film technologies [1].

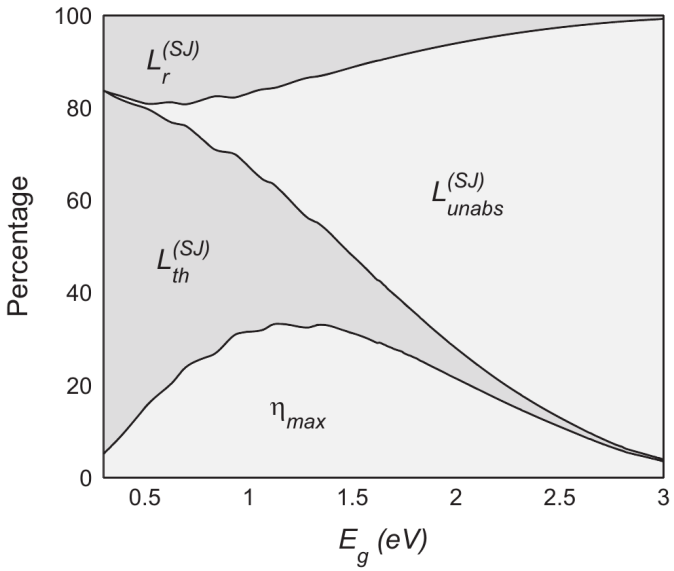

Figure 54.: Maximum conversion efficiency, $\eta_{max}(V)$, along with quantification of losses for a single p-n homojunction with respect to E_G at room temperature. Corresponding losses described in the text are also depicted. (Reprinted from Ref. [256], ©2015 *by Fahhad Alharbi and Sabre Kais, available under the terms and conditions of the Creative Commons Attribution 3.0 License* `https://creativecommons.org/licenses/by/3.0/`)

B

CRYSTAL DISLOCATIONS

B.1 INTRODUCTION

In this appendix we give a short introduction to the theory of dislocations in materials, specifically in semiconductors. Far more complete and general introductions to this interesting topic can be found in the classic books by Hirth and Lothe [99] (now in its third edition, authored also by Peter Anderson) and by Hull and Bacon [100]. Furthermore, excellent treatises of the properties of dislocations in semiconductors are the books by Holt and Yacobi [202] and by Matare [212]. The latter being focused on the electronic properties of these defects.

B.2 SHORT INTRODUCTION TO THE THEORY OF DISLOCATIONS

Dislocations are one-dimensional defects which define many properties and control several processes in crystalline materials, e.g. plastic deformation, creep, fatigue, ductility and brittleness [99, 100, 202]. Furthermore, they are able to modify electrical [202, 257–264] and magnetic [265–268] properties of the crystal in which they are inmersed in. Interestingly, before being detected in experiments or associated to any macroscopic phenomena, dislocations appeared as an abstract mathematical concept. This breakthrough started with the contribution by Weingarten [269], who proved that in the absence of external forces, equilibrium configurations of elastic bodies could still have nonzero internal stress. Based on his work, Volterra [270] studied the mathematical properties of deformations produced by cutting and shifting matter in a solid and continuous body, which he called "distorsioni" (the english name "dislocation" was coined by Love in his 1927 book on elasticity [271]). Decades had to pass until the observations of Ewing and Rosenhain [272], who showed that the plastic deformation in metals originated from the formation of slip bands, were connected with the existence of dislocations. Such hypothesis was proposed independently by Taylor [273, 274], Polanyi [275] and Orowan [276] in 1934 and allowed them to solve the discrepancy between the experimental and theoretical values of the applied shear stress needed to plastically deform crystals. Later on, dislocations were

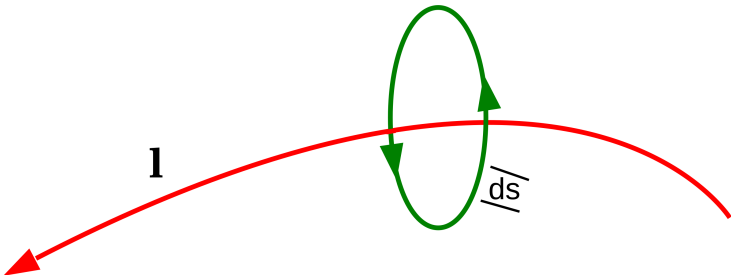

Figure 55.: *Burgers circuit*. In here, **l** is the line direction and d**s** is the differental of the integration path.

also postulated as the explanation to why crystal growth was observed under nearly equilibrium conditions [277]. Such evidence was in conflict with the theoretical predictions made by Volmer [278], which indicated that supersaturations of about 1.5 were needed for layer growth of perfect crystals to occur. It was Frank [279] in 1949 who solved this issue by suggesting that the propagation of ledges, associated with the point of emergence of a dislocation at a surface, would reduce the supersaturation needed for the growth to take place. Surprisingly, all this puzzle-solving success happened before dislocations were directly seen. Experimental confirmation of their existence was only possible in the late 1950s by means of TEM measurements [280]. Today, the relevance of dislocations as key players in materials science is settled. Furthermore, interest on them is expected to grow due recent studies which challenge the previously accepted conception of dislocation being only (detrimental) defects. For example, they have been proposed as native nanostructures [281, 282], one-dimensional doping that modifies ionic conductivity [283–285] and as magnetic nanowires [286, 287], among many other new results.

As pointed out before, this appendix introduces the basics of dislocations and serves as reference material useful to understand the contents of this thesis. Let us start by saying that dislocations are characterized by a pair of vectors: the line direction **l** and the Burgers vector **b**. The latter gives a measure of topological miss-connection of the defective crystal structure and it is an intrinsic property of the dislocation (it can be understood as the dislocation's topological charge) [165]. These formal definitions are easier to grasp by means of the *Burgers circuit*, shown in Figure 55. In there, the displacement field $\mathbf{w}(\mathbf{r})$, is integrated along a closed path **s** and the Burgers vector is calculated as

$$\mathbf{b} = \oint \frac{\partial \mathbf{w}}{\partial s} ds. \tag{B.1}$$

The displacement field, as indicated by its name, describes the displacement of an infinitesimal volume element of the material from its position in an otherwise perfect crystal. Therefore, if the path **s** encircles a portion of a perfect crystal, the

result of the integration would be zero. On the other hand, if the path **s** encircles a dislocation, as depicted in Figure 55, the integration would be a non-zero value, which is the Burgers vector of the dislocation.

This description is valid in continuum mechanics. However, we are focused on the description of dislocations at the atomic scale where **b** cannot take any value, i.e. it is restricted by the the symmetry of the crystal structure in which the dislocation is inmersed in. Following the discussion by Bulatov and Cai [165], in such case the *Burgers circuit* consists of a sequence of steps between neighbouring atoms and we have the following general expression for the Burgers vector

$$\mathbf{b} = \sum_{i=1}^{N} \Delta \mathbf{w}_i, \tag{B.2}$$

where the sum goes over all N steps constituting the path or circuit surrounding the dislocation, and the vectors $\Delta \mathbf{w}_i$ are given by

$$\Delta \mathbf{w}_i := \mathbf{r}_i - (\mathbf{r}_{i-1} + \mathbf{v}_i). \tag{B.3}$$

In Equation B.3, $\mathbf{r}_i$ is the vector pointing to the i-th atomic site in the circuit and $\mathbf{v}_i$ are the individual steps that would constitute the circuit in a perfect crystal. Thus, the vectors $\Delta \mathbf{w}_i$ are the differences between the relative positions of the atoms in the distorted lattice with respect to their positions if they would be in a perfect crystal.

After these definitions, it is possible to understand the previously mentioned concept of the Burgers vector as the dislocation's topological charge: the translation of a given *Burgers circuit* along the direction of the dislocation it encircles, does not affect the value of the Burgers vector. Therefore, the Burgers vector is conserved along a dislocation. Such finding implies that a dislocation cannot end within an otherwise perfect crystal, i.e. they combine with other dislocations or end at a defective region of the lattice (surface, interface, grain boundary, etc).

B.2.1 *Types of dislocations*

The length and direction of the calculated Burgers vector defines the type of the dislocation. Regarding a length based classification, the symmetry of the lattice contrains the magnitude of **b**. If the *Burgers circuit* encircles a single dislocation and the resulting Burgers vector is equal to a lattice translation vector, the dislocation is called *perfect*. If the Burgers vector is equal to a fraction of a lattice translation vector, the dislocation is called *partial*. In the case of a direction based classification, there are three cases:

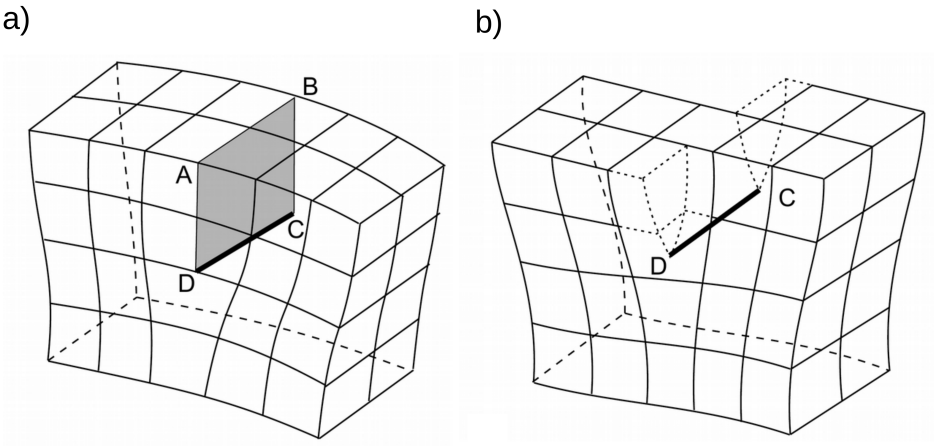

Figure 56.: Edge dislocation (a) and screw dislocation (b) in a simple cubic lattice. The inserted half-plane associated with the presence of an edge dislocation is highlighted by the shaded region in the figure. (Adapted and reprinted from Ref. [100] with permission of Elsevier)

- **Edge dislocation**. An example of this dislocation type is shown in Figure 56a. In such case the Burgers vector is perpendicular to the line direction:

$$\mathbf{b}_{edge} \cdot \mathbf{l} = 0. \tag{B.4}$$

  Topologically, such dislocation involves an inserted half-plane as highlighted by the shaded region in Figure 56.

- **Screw dislocation**. As shown in Figure 56b, this dislocation type involves shearing part of the crystal in the direction of the dislocation, while keeping the other part of the crystal fixed. For this dislocation type the Burgers vector is parallel to the line direction:

$$\mathbf{b}_{screw} \times \mathbf{l} = 0. \tag{B.5}$$

- **Mixed dislocation**. In this case the angle θ between $\mathbf{b}$ and $\mathbf{l}$ is neither $0°$ nor $90°$. Therefore, such dislocations result from a superposition of edge and screw components.

B.2.2 *Dislocation motion*

Although in this thesis we do not study the movement of dislocations in $Cu(In,Ga)Se_2$, its discussion is needed in order to understand the simulation procedure we present in Section 3.4.1. As mentioned before, a first breakthrough for dislocation theory came when it provided a solution to the discrepancy between the experimental and theoretical values of the applied shear stress needed

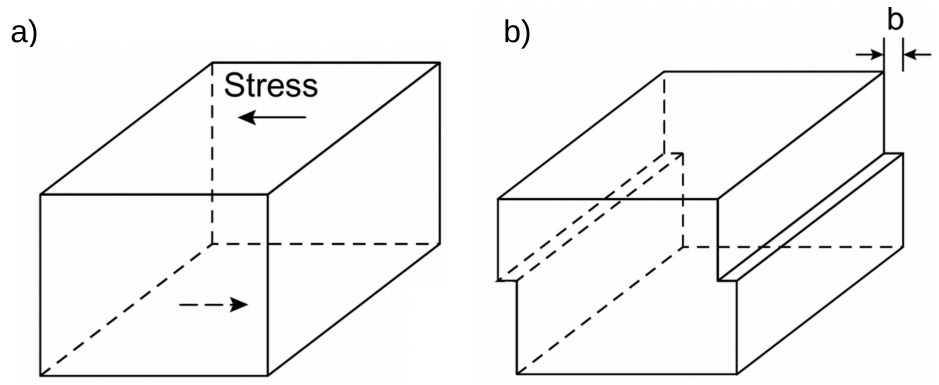

Figure 57.: Perfect (a) and sheared (b) cubic crystal. For the latter, the upper half of it displaced by **b** with respect to the lower half. The coordinate system and corresponding lengths, L, of the structure are also shown. (Adapted and reprinted from Ref. [100] with permission of Elsevier)

to plastically deform crystals. In fact, dislocation motion plays a central role in this issue. Let us imagine we shear a perfect crystal, Figure 57a, by displacing the whole upper half of it with respect to the lower half until a state like the one shown in Figure 57b is reached. In that case atomic rearrangements would occur over an entire plane and would imply the rupture of all atomic bonds crossing this plane.

It should be noticed that the same final sheared structure can be obtained due to the motion of an edge dislocation, as it is shown in Figure 58. However, in such case only small and local distortions are needed for the gradual displacement of the dislocation from its initial to its final position. For example, from Figure 58a to 58b, the dislocation moved to the right and its half-inserted plane changed from plane x to plane y due to small shifts in the position of atoms 1, 2 and 3. Evidently, such process costs much less energy than atomic rearrangements over a complete plane. This mechanism reconciles the experimental and theoretical values for the applied shear stress needed to plastically deform crystals. By a repetition of these small atomic rearregements, the dislocation reaches the end of the crystal section shown in the figure, leaving behind an structure which is equal to the one obtained by shearing the upper half part as a whole.

As it is evidenced in Figure 58, the dislocation motion occurs due to an applied stress acting on the dislocation. This is summarized in the Peach-Koehler formula,

$$\mathbf{F} = (\sigma \cdot \mathbf{b}) \times \xi, \tag{B.6}$$

where **F** is the force experienced by the dislocation with Burgers vector **b** when inmersed in the stress σ, regardless the origin of the stress. In Equation B.6, ξ is the unit vector locally tangential to the dislocation direction.

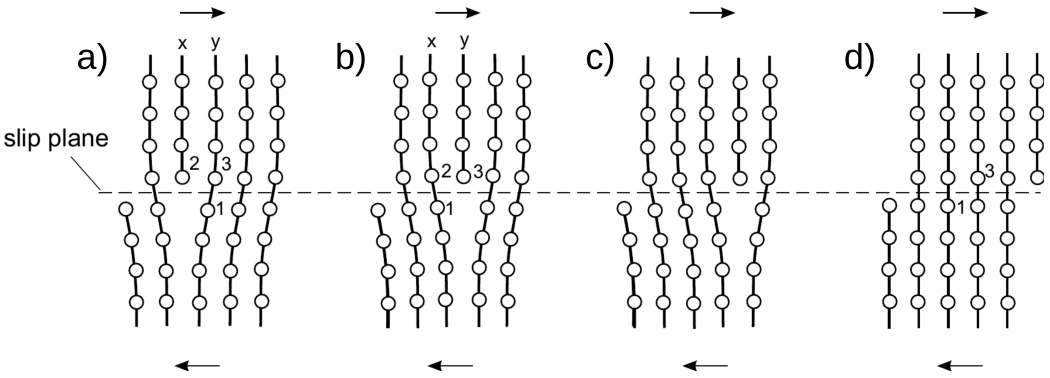

Figure 58.: Movement of an edge dislocation. Arrows indicate the direction of the applied shear stress that causes the movement. (Adapted and reprinted from Ref. [100] with permission of Elsevier)

Another way to understand dislocation motion, as presented in Figure 58, is that as the dislocation moves, it induces a plastic strain $\mathbf{u}^p$ into the crystal. This strain is proportional to the area swept by the dislocation and its components are given by

$$\mathrm{u}^p_{\eta\zeta} = \frac{(b_\eta a_\zeta + b_\zeta a_\eta)\Delta A}{2\Omega}, \tag{B.7}$$

where the b_η are the components of $\mathbf{b}$ and the a's are the components of the vector $\mathbf{A}$ which is perpendicular to the plane of the area ΔA swept by the dislocation as it moves.

Until now we have talked about dislocation motion as a single process and concepts introduced up to this point are general. However, there are two basic types of dislocation motion:

- **Dislocation glide**. This motion process occurs in the glide plane of the dislocation, hence the name. The glide plane is defined as the plane which simultaneously contains $\mathbf{b}$ and $\mathbf{l}$. In the case of an edge dislocation, this process does not imply a change in the total number of atoms in the crystal. For that reason it is often called *conservative motion*. A relevant process associated with glide process is *slip*, the most common indication of plastic deformation of crystals, which is caused by the glide of many dislocations on the same *slip plane*. This orientation of this plane depends on the symmetry of the crystal and are usually the planes with highest density of atoms. Since $\mathbf{b}$ and $\mathbf{l}$ are parallel in the case of screw dislocations, their glide plane is not uniquely defined and they can glide in any direction in the crystal.

- **Dislocation climb**. This process can only occur for dislocation with an edge character. It occurs when the dislocation moves perpendicular to the

plane defined by its **b** and **l**. As the dislocation moves in this fashion, its inserted half-plane either shrinks or expands by means of atomic diffusion. Since the number of atom sites change during climb, this process is often called *non-conservative motion*.

B.2.3 *Dislocation dissociation*

Following the discussion by Hull and Bacon [100], the elastic energy per unit length of a dislocation is relatively insensitive to the character of the dislocation and can be approximated by

$$E_{el} = \kappa S \mathbf{b}^2, \tag{B.8}$$

where $\kappa \sim 0.5 - 1.0$ and S is the shear modulus of the material. It can happen that due to energetic reasons, it would be preferred that a dislocation with a large Burgers vector $\mathbf{b}_1$ dissociates into two dislocations with smaller Burgers vectors $\mathbf{b}_2$ and $\mathbf{b}_3$. Such process would occur only if the condition

$$\|\mathbf{b}_1\|^2 > \|\mathbf{b}_2\|^2 + \|\mathbf{b}_3\|^2, \tag{B.9}$$

is fullfilled. Naturally, the dissociation is constrained by the conservation of the Burgers vector, i.e $\mathbf{b}_1 = \mathbf{b}_2 + \mathbf{b}_3$. This means that if a perfect dislocation with Burgers vector equal to a lattice translation vector of the crystal dissociates following these rules, the resulting dislocations with $\mathbf{b}_2$ and $\mathbf{b}_3$ would be partial dislocations. The general principles of dislocation motion described before for perfect dislocations apply also for partial ones. However, as can be inferred from Figures 57 and 58, when partials move they leave behind an imperfect crystal containing an stacking fault. Therefore, a stacking fault will exist between the partials resulting from a dissociation. Furthermore, if a stacking fault terminates within a crystal, the boundary between the fault and the perfect crystal is a partial dislocation.

ERKLÄRUNG ZUR DISSERTATION

Hiermit versichere ich, die vorliegende Dissertation selbständig mit Hilfe der angegebenen Quellen und Hilfsmittel angefertigt zu haben. Alle Stellen, die aus Quellen entnommen wurden, sowie alle Daten, die aus Kollaborationen stammen, sind als solche kenntlich gemacht. Diese Arbeit hat in gleicher oder ähnlicher Form noch keiner Prüfungsbehörde vorgelegen, ein Promotionsversuch wurde von mir bisher nicht unternommen.

Darmstadt, den 04. June 2018

(Daniel Antonio Barragan-Yani)

ACKNOWLEDGMENTS

During the last four years I have had by my side amazing people which made this thesis possible. Without their advice, critique, help and support it would have been unlikely to prevail in this struggle and for that I am grateful.

I would like to thank Prof. Dr. Karsten Albe for giving me the opportunity to pursue this research in his group. From my side there is only lasting gratitude for his mentoring and his interest on my development as a scientist. Moreover, I am thankful for his keen insight and constructive criticism which have been an uninterrupted source of personal and professional growth.

Next, I would like to express my gratitute to Priv. Doz. Dr. Daniel Abou-Ras. Besides coordinating the virtual institute of the Helmholtz association within which my research has taken place, he has always provided an excellent environment for scientific discussions. Without any doubt his thoughtful advice and continuous support were essential to succesfully finish my doctorate.

Being part of the virtual institute has also given me the opportunity to enjoy a nice collaborative working environment with other doctoral students. Specially, I would like to acknowledge the cooperation and support from Ekin, Helena and Sibylle. Despite working on different fields, we have managed to carry out fruitful research in a process which altoghether has been a great learning experience. It is my personal perception, that by helping each other to overcome our difficulties, we have indeed improved ourselves.

Another reason to be grateful has been the great atmosphere in the MM group. Gabriele and Renate are greatly responsible for this, and I thank them for their support and for isolating me as much as possible from the administrative issues that arised during the last four years. Furthermore, I consider myself fortunate because, along with new knowledge and a huge number of new doubts in my mind, my doctorate has given me the chance to meet Connie, Kai, Jochen, Leonie, Markus and Omar. Thank you guys for your friendship.

Financial support by the Helmholtz Virtual Institute HVI-520 "Microstructure Control for Thin-Film Solar Cells" is gratefully acknowledged. Furthermore, I am thankful for the computing time granted by the John von Neumann Institute for Computing (NIC), provided on the supercomputer JURECA at Jülich Supercomputing Centre (JSC), and the computing time granted by the TU Darmstadt on the Lichtenberg High-Performance Computer.

A nivel personal, quiero dar gracias a Dios por la vida y salud que me ha dado. De igual manera, agradezco de todo corazón el apoyo y amistad que Alfonso, Angela, Mercedes, Zeeshan y Jhon nos han brindado a mi y a mi familia. Sin duda, tenerlos a nuestro lado ha hecho las cosas mas fáciles. A mis amigos Pedro,

Carlos, Javi, Alvaro, Jagger, Erik y Miguel que a pesar de la distancia siempre han estado presentes. Le doy gracias a mi amado hermano Juan David por su amistad y por nuestras conversaciones, que siempre han sido una válvula de escape para la presión acumulada durante el día a día. A mi tío Nacho y mi tía Nena, cuyo amor y enseñanzas siguen siendo una luz perenne que ilumina mi camino. A mi papá y mamá, mis héroes, gracias por amarme, por todo lo que han hecho por mi y por su apoyo incondicional. Su sacrificio y dedicación son la base de lo que soy y cada logro mío es también de ustedes.

Finalmente, gracias a mis amados Santiago y Andrea por su paciencia y por estar en mi vida. Su sola presencia me reconforta en los días mas oscuros y su amor me da fuerza para continuar. Ellos han hecho tantos sacrificios como yo durante mi doctorado y esta tesis también les pertenece.

Curiculum Vitae

Personal data

Name	Daniel Antonio Barragan-Yani
Email	barragan@mm.tu-darmstadt.de
Date of birth	13. November 1985 Barranquilla, Colombia

Education

01/2014–05/2018	**Doctoral studies in Materials Science.** Thesis: *First-principles study of dislocations in Cu(In,Ga)Se_2 solar cell absorbers* Materials Modeling Division (Prof. Dr. K. Albe), Technische Universität Darmstadt, Germany
10/2011–12/2013	**M.Sc. in Computational Science.** Institut für Theoretische Physik (Prof. Dr. Roser Valenti) Goethe Universität Frankfurt, Germany
07/2009–	**M.Sc. in Applied Physics.** Department of Physics (Dr. Erick Tuiran) Universidad del Norte, Barranquilla, Colombia
02/2003–02/2008	**B.Sc. in Electronic Engineering.** Universidad del Norte, Barranquilla, Colombia

Research Experience

10/2008–Present	**Scientific staff member** (Wissenschaftlicher Mitarbeiter) Materials Modeling Division (Prof. K. Albe), Technische Universität Darmstadt, Germany
01/2008–02/2009	**Young innovator researcher - COLCIENCIAS**, Department of Electronic and Electrical Engineering Telecommunications Group (Prof. Diego Gomez), Universidad del Norte, Barranquilla, Colombia

07/2007–06/2008 **Research assistant**,
Department of Electronic and Electrical Engineering
Telecommunications Group (Prof. Alexander Morante),
Universidad del Norte, Barranquilla, Colombia

Peer-reviewed articles based on the present dissertation

A1 D. Barragan-Yani and K. Albe, *Influence of Na and Ga on the electrical properties of perfect 60° dislocations in Cu(In,Ga)Se_2 thin-film photovoltaic absorbers*, J. Appl. Phys. **123**, 165705 (2018).

A2 D. Barragan-Yani and K. Albe, *Atomic and electronic structure of perfect dislocations in the solar absorber materials $CuInSe_2$ and $CuGaSe_2$ studied by first-principles calculations*, Phys. Rev. B 95, 115203 (2017).

A3 E. Simsek Sanli, D. Barragan-Yani, Q. Ramasse, K. Albe, R. Mainz, D. Abou-Ras, A. Weber, H.-J. Kleebe and P. A. van Aken, *Point defect segregation and its role in the detrimental nature of Frank partials in $Cu(In,Ga)Se_2$ thin-film absorbers*, Phys. Rev. B 95, 195209 (2017).

A4 D. Abou-Ras, S. Schmidt, N. Schäfer, J. Kavalakkatt, T. Rissom, T. Unold, R. Mainz, A. Weber, T. Kirchartz, E. Simsek Sanli, P. A. van Aken, Q. Ramasse, H.-J. Kleebe, D. Azulay, I. Balberg, O. Millo, O. Cojocaru-Miredin, D. Barragan-Yani, K. Albe, J. Haarstrich and C. Ronning, *Compositional and electrical properties of line and planar defects in $Cu(In,Ga)Se_2$ thin films for solar cells - a review*, Phys. Status Solidi 10, No. 5, 363-375 (2016).

Other peer-reviewed articles

A5 H. Stange, S. Brunken, D. Greiner, M. D. Heinemann, D. Barragan-Yani, L. A. Wägele, S. Schmidt, J.-P. Bäcker, C. Kaufmann, M. Klaus, R. Scheer, C. Genzel, and R. Mainz, *Stacking fault reduction during annealing in Cu-poor $CuInSe_2$ thin film solar cell absorbers analyzed by in-situ XRD and grain growth modeling*, submitted to Phys. Rev. Applied.

A6 S. Bergmann, K. Albe, E. Flegel, D. Barragan-Yani and B. Wagner, *Anisotropic solid-liquid interface kinetics in silicon: an atomistically informed phase-field model*, Modelling Simul. Mater. Sci. Eng. 25 065015 (2017).

A7 V. Mendoza-Estrada, A. Gonzalez-Garcia, D. Barragan-Yani, W. lopez-Perez, J. Rivera-Julio and R. Gonzalez-Hernandez, *Ferromagnetic orderings in $Co_xCu_yZn_{1-(x+y)}O$ by GGA and GGA+U formalisms within density functional theory*, Computational Materials Science 126, 344-350 (2017).

A8 A. Gonzalez-Garcia, W. lopez-Perez, D. Barragan-Yani and R. Gonzalez-Hernandez, *A comparative DFT and DFT+U study on magnetism in Nickel-doped wurtzite AlN*, J. Supercond. Nov. Mag. 28, 3185-3192 (2015).

A9 R. Gonzalez-Hernandez, A. Gonzalez-Garcia, D. Barragan-Yani and W. lopez-Perez, *A comparative DFT study of the structural and electronic properties of nonpolar GaN surfaces*, Applied Surface Science 314, 794-799 (2014).

A10 Y. Donoso, G. Jimenez, D. Barragan, A. Ortiz, D. Pinedo, *Optimization of the design of digital filters using evolutionary algorithms*, SPECTS proceedings (2010).

Oral and poster presentations at international conferences

C1 D. Barragan-Yani and K. Albe, *Strain effects on point defect properties in $CuInSe_2$ and $CuGaSe_2$: an elastic dipole tensor based study* (Oral presentation), 29th International Conference on Defects in Semiconductors, Matsue, Japan, 2017.

C2 D. Barragan-Yani and K. Albe, *Point defect segregation around dislocations in $Cu(In,Ga)Se_2$: vital or fatal?* (Oral presentation), E-MRS spring meeting, Strasbourg, France, 2017.

C3 D. Barragan-Yani, J. Pohl and K. Albe, *A Lattice Monte Carlo growth model for silicon including (111) stacking faults and twin boundaries* (Oral presentation), 19th European Conference on Mathematics for Industry, Santiago de Compostela, Spain, 2016.

C4 D. Barragan-Yani and K. Albe, *Electronic and Structural Properties of Dislocations in the Solar Absorber Materials $CuInSe_2$ and $CuGaSe_2$* (Oral presentation), MRS spring meeting, Phoenix, USA, 2016.

C5 D. Barragan-Yani and K. Albe, *Ab-initio study of perfect dislocations in $CuInSe_2$ and $CuGaSe_2$* (Poster presentation), E-MRS spring meeting, Lille, France, 2015.

Darmstadt, June 2018

BIBLIOGRAPHY

[1] P. Jackson, R. Wuerz, D. Hariskos, E. Lotter, W. Witte, and M. Powalla, physica status solidi (RRL) - Rapid Research Letters **10**, 583 (2016).

[2] S. Siebentritt, Solar Energy Materials and Solar Cells **95**, 1471 (2011), special Issue : Thin film and nanostructured solar cells.

[3] S. B. Zhang, S.-H. Wei, A. Zunger, and H. Katayama-Yoshida, Physical Review B **57**, 9642 (1998).

[4] S.-H. Wei, S. B. Zhang, and A. Zunger, Journal of Applied Physics **85**, 7214 (1999).

[5] J. Pohl and K. Albe, Physical Review B **87**, 245203 (2013).

[6] C. Persson and A. Zunger, Physical Review Letters **91**, 266401 (2003).

[7] Y. Yan *et al.*, Journal of Applied Physics **117**, 112807 (2015).

[8] W.-J. Yin, Y. Wu, R. Noufi, M. Al-Jassim, and Y. Yan, Applied Physics Letters **102**, 193905 (2013).

[9] D. Abou-Ras *et al.*, physica status solidi (RRL) - Rapid Research Letters **10**, 363 (2016).

[10] S. Siebentritt, Current Opinion in Green and Sustainable Chemistry **4**, 1 (2017), 4 Novel materials for energy production and storage 2017.

[11] J. Dietrich, D. Abou-Ras, T. Rissom, T. Unold, H. W. Schock, and C. Boit, in *2011 37th IEEE Photovoltaic Specialists Conference* (IEEE, Seattle, 2011), pp. 000343–000347.

[12] J. Dietrich, D. Abou-Ras, T. Rissom, T. Unold, H. W. Schock, and C. Boit, IEEE Journal of Photovoltaics **2**, 364 (2012).

[13] J. Dietrich, D. Abou-Ras, S. S. Schmidt, T. Rissom, T. Unold, O. Cojocaru-Mirédin, T. Niermann, M. Lehmann, C. T. Koch, and C. Boit, Journal of Applied Physics **115**, 103507 (2014).

[14] FCCC, *Paris agreement - Status of Ratification* (FCCC, New York, Status on September 2017).

[15] Nature Materials **16**, 691 (2017), editorial.

[16] A. Kleidon, *Thermodynamic Foundations of the Earth System* (Cambridge University Press, Oxford, 2016).

[17] P. Wuerfel, *Physics of Solar Cells: From Basic Principles to Advanced Concepts* (Wiley-VCH Verlag GmbH & Co., Weinheim, 2016).

[18] G. Bauer, *Photovoltaic Solar Energy Conversion* (Springer-Verlag, Berlin-Heidelberg, 2015).

[19] W. Shockley and H. J. Queisser, Journal of Applied Physics **32**, 510 (1961).

[20] H. W. Schock and U. Rau, Physica B: Condensed Matter **308**, 1081 (2001), international Conference on Defects in Semiconductors.

[21] T. M. Augustin McEvoy and L. Castaner, *Practical Handbook of Photovoltaics: Fundamentals and Applications* (Academic Press, Waltham, 2012).

[22] M. A. Green, Y. Hishikawa, E. D. Dunlop, D. H. Levi, J. Hohl-Ebinger, and A. W. Ho-Baillie, Progress in Photovoltaics: Research and Applications **26**, 3 .

[23] R. Scheer and H.-W. Schock, *Chalcogenide Photovoltaics* (Wiley-VCH Verlag & Co., Weinheim, 2011).

[24] S. Kodigala, $Cu(In, Ga)Se_2$ *Based Thin-Film Solar Cells* (Academic Press, Waltham, 2010).

[25] J. Neugebauer and T. Hickel, Wiley Interdisciplinary Reviews: Computational Molecular Science **3**, 438 (2013).

[26] R. O. Jones, Reviews of Modern Physics **87**, 897 (2015).

[27] C. Freysoldt, B. Grabowski, T. Hickel, J. Neugebauer, G. Kresse, A. Janotti, and C. G. Van de Walle, Reviews of Modern Physics **86**, 253 (2014).

[28] J. Dietrich, D. Abou-Ras, T. Rissom, T. Unold, H. W. Schock, and C. Boit, IEEE Journal of Photovoltaics **2**, 364 (2012).

[29] A. Smets, K. Jäger, O. Isabella, R. van Swaaij, and M. Zeman, *Solar Energy: The Physics and Engineering of Photovoltaic Conversion Technologies and Systems* (UIT cambridge Ltd, Cambridge, 2016).

[30] J. Nelson, *The Physics of Solar Cells* (Imperial College Press, London, 2003).

[31] G. Conibeer and A. Willoughby, *Solar Cell Materials: Developing Technologies* (John Wiley & Sons, Ltd, Chichester, 2014).

[32] D. C. Reynolds, G. Leies, L. L. Antes, and R. E. Marburger, Physical Review **96**, 533 (1954).

[33] K. W. Böer, Physical Review B **13**, 5373 (1976).

[34] J. S. H. M. Kasper, P. Migliorato and S. Wagner, Heterojunction Photovoltaic Devices Employing I-III-VI Compounds, 1976.

[35] D. Abou-Ras *et al.*, Thin Solid Films **633**, 2 (2017), e-MRS 2016 Spring Meeting, Symposium V, Thin-Film Chalcogenide Photovoltaic Materials.

[36] S. Wagner, J. L. Shay, P. Migliorato, and H. M. Kasper, Applied Physics Letters **25**, 434 (1974).

[37] J. L. Shay, S. Wagner, and H. M. Kasper, Applied Physics Letters **27**, 89 (1975).

[38] D. Abou-Ras, T. Kirchartz, and U. Rau, *Advanced Characterization Techniques for Thin Film Solar Cells* (Wiley-VCH Verlag GmbH & Co., Weinheim, 2016).

[39] E. S. Mungan, X. Wang, and M. A. Alam, in *2012 IEEE 38th Photovoltaic Specialists Conference (PVSC) PART 2* (IEEE, Austin, 2012), pp. 1–6.

[40] P. Salomé, H. Rodriguez-Alvarez, and S. Sadewasser, Solar Energy Materials and Solar Cells **143**, 9 (2015).

[41] S. Siebentritt, M. Igalson, C. Persson, and S. Lany, Progress in Photovoltaics: Research and Applications **18**, 390 (2010).

[42] S. Nishiwaki and N. T. W. T. Kohara, Naoki, Japanese Journal of Applied Physics **37**, L71 (1998).

[43] D. Abou-Ras, G. Kostorz, D. Bremaud, and M. K Thin Solid Films **480**, 433 (2005), eMRS 2004.

[44] L. Weinhardt, C. Heske, E. Umbach, T. P. Niesen, S. Visbeck, and F. Karg, Applied Physics Letters **84**, 3175 (2004).

[45] A. Klein, Journal of Physics: Condensed Matter **27**, 134201 (2015).

[46] A. M. Gabor, J. R. Tuttle, D. S. Albin, M. A. Contreras, R. Noufi, and A. M. Hermann, Applied Physics Letters **65**, 198 (1994).

[47] R. A. Mickelsen and W. S. Chen, Applied Physics Letters **36**, 371 (1980).

[48] R. Caballero, V. Izquierdo-Roca, X. Fontané, C. Kaufmann, J. Álvarez-García, A. Eicke, L. Calvo-Barrio, A. Pérez-Rodríguez, H. Schock, and J. Morante, Acta Materialia **58**, 3468 (2010).

[49] R. Caballero, C. A. Kaufmann, V. Efimova, T. Rissom, V. Hoffmann, and H. W. Schock, Progress in Photovoltaics: Research and Applications **21**, 30 (2013).

[50] R. Mainz *et al.*, Energy Environmental Science **9**, 1818 (2016).

[51] S. Niki, M. Contreras, I. Repins, M. Powalla, K. Kushiya, S. Ishizuka, and K. Matsubara, Progress in Photovoltaics: Research and Applications **18**, 453 (2010).

[52] J. Li, Nature Materials **14**, 656 EP (2015).

[53] G. Dhanaraj, K. Byrappa, V. Prasad, and M. Dudley, *Springer Handbook of Crystal Growth*, *Springer Handbook of Crystal Growth* (Springer-Verlag GmbH, Berlin-Heidelberg, 2010).

[54] C. Claeys and E. Simoen, *Extended Defects in Germanium: Fundamental and Technological Aspects*, *Springer Series in Materials Science* (Springer-Verlag GmbH, Berlin-Heidelberg, 2008).

[55] J. Godet, L. Pizzagalli, S. Brochard, and P. Beauchamp, Physical Review B **70**, 054109 (2004).

[56] J. Godet, S. Brochard, L. Pizzagalli, P. Beauchamp, and J. M. Soler, Physical Review B **73**, 092105 (2006).

[57] J. Godet, P. Hirel, S. Brochard, and L. Pizzagalli, physica status solidi (a) **206**, 1885 (2009).

[58] Z. Li and R. C. Picu, Journal of Applied Physics **108**, 033522 (2010).

[59] J. Rabier, L. Pizzagalli, and J. Demenet, in *Chapter 93 Dislocations in Silicon at High Stress*, Vol. 16 of *Dislocations in Solids*, edited by J. Hirth and L. Kubin (Elsevier, New York, 2010), pp. 47 – 108.

[60] W. Witte *et al.*, Progress in Photovoltaics: Research and Applications **23**, 717 (2015), pIP-13-225.R2.

[61] N. I. Medvedeva, E. V. Shalaeva, M. V. Kuznetsov, and M. V. Yakushev, Physical Review B **73**, 035207 (2006).

[62] A. Luque and S. Hegedus, *Handbook of Photovoltaic Science and Engineering* (John Wiley & Sons Ltd, Chichester, 2003).

[63] Y. Hagiwara, T. Nakada, and A. Kunioka, Solar Energy Materials and Solar Cells **67**, 267 (2001), pVSEC 11 - PART III.

[64] S. Siebentritt, Solar Energy **77**, 767 (2004).

[65] D. Hariskos, S. Spiering, and M. Powalla, Thin Solid Films **480**, 99 (2005), eMRS 2004.

[66] U. Rau and H. Schock, Applied Physics A **69**, 131 (1999).

[67] L. Gütay, C. Lienau, and G. H. Bauer, Applied Physics Letters **97**, 052110 (2010).

[68] M. Müller, D. Abou-Ras, T. Rissom, F. Bertram, and J. Christen, Journal of Applied Physics **115**, 023514 (2014).

[69] U. Rau and J. H. Werner, Applied Physics Letters **84**, 3735 (2004).

[70] U. Rau, K. Taretto, and S. Siebentritt, Applied Physics A **96**, 221 (2008).

[71] I. Repins, M. A. Contreras, B. Egaas, C. DeHart, J. Scharf, C. L. Perkins, B. To, and R. Noufi, Progress in Photovoltaics: Research and Applications **16**, 235 (2008).

[72] P. Jackson, D. Hariskos, E. Lotter, S. Paetel, R. Wuerz, R. Menner, W. Wischmann, and M. Powalla, Progress in Photovoltaics: Research and Applications **19**, 894 (2011).

[73] M. Burgelman *et al.*, Progress in Photovoltaics: Research and Applications **5**, 121 (1997).

[74] A. Rockett, AIP Conference Proceedings **462**, 132 (1999).

[75] D. Abou-Ras, Habilitation monograph, Technische Universität Berlin, 2015.

[76] E. Korhonen, K. Kuitunen, F. Tuomisto, A. Urbaniak, M. Igalson, J. Larsen, L. Gütay, S. Siebentritt, and Y. Tomm, Physical Review B **86**, 064102 (2012).

[77] C. Stephan, S. Schorr, M. Tovar, and H.-W. Schock, Applied Physics Letters **98**, 091906 (2011).

[78] C. Stephan, T. Scherb, C. A. Kaufmann, S. Schorr, and H.-W. Schock, Applied Physics Letters **101**, 101907 (2012).

[79] L. E. Oikkonen, M. G. Ganchenkova, A. P. Seitsonen, and R. M. Nieminen, Journal of Physics: Condensed Matter **26**, 345501 (2014).

[80] J. Bekaert, R. Saniz, B. Partoens, and D. Lamoen, Physical Chemistry Chemical Physics **16**, 22299 (2014).

[81] J. T. Heath, J. D. Cohen, W. N. Shafarman, D. X. Liao, and A. A. Rockett, Applied Physics Letters **80**, 4540 (2002).

[82] T. Sakurai, H. Uehigashi, M. Islam, T. Miyazaki, S. Ishizuka, K. Sakurai, A. Yamada, K. Matsubara, S. Niki, and K. Akimoto, Thin Solid Films **517**, 2403 (2009), thin Film Chalogenide Photovoltaic Materials (EMRS, Symposium L).

[83] J. K. Larsen, K. Burger, L. Gütay, and S. Siebentritt, in *2011 37th IEEE Photovoltaic Specialists Conference* (IEEE, Seattle, 2011).

[84] S. Siebentritt, L. Gütay, D. Regesch, Y. Aida, and V. Depredurand, Solar Energy Materials and Solar Cells **119**, 18 (2013).

[85] Y. Yan, K. Jones, C. Jiang, X. Wu, R. Noufi, and M. Al-Jassim, Physica B: Condensed Matter **401**, 25 (2007).

[86] B. Yin and C.-G. Lou, Rare Metals **34**, 510 (2015).

[87] M. Gloeckler, J. R. Sites, and W. K. Metzger, Journal of Applied Physics **98**, 113704 (2005).

[88] K. Taretto, U. Rau, and J. Werner, Thin Solid Films **480**, 8 (2005), eMRS 2004.

[89] D. Abou-Ras, S. Schorr, and H. W. Schock, Journal of Applied Crystallography **40**, 841 (2007).

[90] D. Abou-Ras, B. Schaffer, M. Schaffer, S. S. Schmidt, R. Caballero, and T. Unold, Physical Review Letters **108**, 075502 (2012).

[91] H. Yamaguchi, H. Hiramatsu, H. Hosono, and T. Mizoguchi, Applied Physics Letters **104**, 153904 (2014).

[92] H. Mirhosseini, J. Kiss, and C. Felser, Physical Review Applied **4**, 064005 (2015).

[93] C. Persson and A. Zunger, Applied Physics Letters **87**, 211904 (2005).

[94] M. Hafemeister, S. Siebentritt, J. Albert, M. C. Lux-Steiner, and S. Sadewasser, Physical Review Letters **104**, 196602 (2010).

[95] J. Kavalakkatt, D. Abou-Ras, J. Haarstrich, C. Ronning, M. Nichterwitz, R. Caballero, T. Rissom, T. Unold, R. Scheer, and H. W. Schock, Journal of Applied Physics **115**, 014504 (2014).

[96] D. Abou-Ras *et al.*, Thin Solid Films **517**, 2545 (2009), thin Film Chalogenide Photovoltaic Materials (EMRS, Symposium L).

[97] J. Dietrich, Phd. thesis, Technische Universität Berlin, 2013.

[98] J. Hornstra, Journal of Physics and Chemistry of Solids **5**, 129 (1958).

[99] P. Anderson, J. Hirth, and J. Lothe, *Theory of Dislocations* (Cambridge University Press, Cambridge, 2017).

[100] D. Hull and D. J. Bacon, *Introduction to Dislocations* (Butterworth-Heinemann form Elsevier Ltd., Oxford, 2011).

[101] X. Zhou, D. K. Ward, B. M. Wong, F. P. Doty, and J. A. Zimmerman, The Journal of Physical Chemistry C **116**, 17563 (2012), pMID: 22962626.

[102] C.-Z. Wang, J. Li, K.-M. Ho, and S. Yip, Applied Physics Letters **89**, 051910 (2006).

[103] M. Pasemann and P. Klimanek, Kristall und Technik **8**, 1141 (1973).

[104] M. Pasemann, P. Klimanek, and H. Oettel, physica status solidi (a) **22**, K1 (1974).

[105] L. E. Murr and S. L. Lerner, Journal of Materials Science **12**, 1349 (1977).

[106] J.-J. Couderc and C. Hennig-Michaeli, Physics and Chemistry of Minerals **13**, 393 (1986).

[107] J.-J. Couderc and C. Hennig-Michaeli, Philosophical Magazine A **57**, 301 (1988).

[108] C. J. Kiely, R. C. Pond, G. Kenshole, and A. Rockett, Philosophical Magazine A **63**, 1249 (1991).

[109] M. Reiche and M. Kittler, Crystals **6**, (2016).

[110] K. Kumakura, T. Makimoto, N. Kobayashi, T. Hashizume, T. Fukui, and H. Hasegawa, Applied Physics Letters **86**, 052105 (2005).

[111] J. H. You, J.-Q. Lu, and H. T. Johnson, Journal of Applied Physics **99**, 033706 (2006).

[112] E. Simsek Sanli, D. Barragan-Yani, Q. M. Ramasse, K. Albe, R. Mainz, D. Abou-Ras, A. Weber, H.-J. Kleebe, and P. A. van Aken, Physical Review B **95**, 195209 (2017).

[113] J. Hinks and S. Donnelly, Philosophical Magazine **91**, 517 (2011).

[114] L. Gütay, D. Regesch, J. K. Larsen, Y. Aida, V. Depredurand, and S. Siebentritt, Applied Physics Letters **99**, 151912 (2011).

[115] H. Stange *et al.*, Applied Physics Letters **107**, 152103 (2015).

[116] W. Kohn, *Nobel Lectures in Chemistry 1996 - 2000: Electronic Structure of Matter - Wave Functions and Density Functionals* (World Scientific, Singapore, 2003).

[117] P. E. Blöchl, Theory and Practice of Density-Functional Theory, 2011.

[118] P. Hohenberg and W. Kohn, Physical Review **136**, B864 (1964).

[119] R. Martin, *Electronic Structure: Basic Theory and Practical Methods* (Cambridge University Press, Cambridge, 2004).

[120] J. Kohanoff, *Electronic Structure Calculations for Solids and Molecules: Theory and Computational Methods* (Cambridge University Press, Cambridge, 2006).

[121] E. Engel and R. Dreizler, *Density Functional Theory: An Advanced Course*, *Theoretical and Mathematical Physics* (Springer-Verlag GmbH, Berlin-Heidelberg, 2011).

[122] R. O. Jones and O. Gunnarsson, Reviews of Modern Physics **61**, 689 (1989).

[123] R. O. Jones, Reviews of Modern Physics **87**, 897 (2015).

[124] A. J. Cohen, P. Mori-Sánchez, and W. Yang, Chemical Reviews **112**, 289 (2012), pMID: 22191548.

[125] M. Born and R. Oppenheimer, Annalen der Physik **389**, 457 (1927).

[126] V. Fock, Zeitschrift für Physik **61**, 126 (1930).

[127] J. C. Slater, Physical Review **35**, 210 (1930).

[128] W. Kohn and L. J. Sham, Physical Review **140**, A1133 (1965).

[129] C. Fiolhais, F. Nogueira, and M. Marques, *A Primer in Density Functional Theory*, *Lecture Notes in Physics* (Springer-Verlag GmbH, Berlin-Heidelberg, 2003).

[130] G. Kresse and J. Furthmüller, Physical Review B **54**, 11169 (1996).

[131] G. Kresse and J. Furthm Computational Materials Science **6**, 15 (1996).

[132] X. Gonze *et al.*, Computational Materials Science **25**, 478 (2002).

[133] P. A. M. Dirac, Mathematical Proceedings of the Cambridge Philosophical Society **26**, 376 (1930).

[134] R. A. Coldwell-Horsfall and A. A. Maradudin, Journal of Mathematical Physics **1**, 395 (1960).

[135] M. Gell-Mann and K. A. Brueckner, Physical Review **106**, 364 (1957).

[136] L. Onsager, L. Mittag, and M. J. Stephen, Annalen der Physik **473**, 71 (1966).

[137] D. M. Ceperley and B. J. Alder, Physical Review Letters **45**, 566 (1980).

[138] J. P. Perdew and Y. Wang, Physical Review B **45**, 13244 (1992).

[139] J. P. Perdew and A. Zunger, Physical Review B **23**, 5048 (1981).

[140] K. Terakura, T. Oguchi, A. R. Williams, and J. Kübler, Physical Review B **30**, 4734 (1984).

[141] F. Herman, J. P. Van Dyke, and I. B. Ortenburger, Physical Review Letters **22**, 807 (1969).

[142] J. P. Perdew and W. Yue, Physical Review B **33**, 8800 (1986).

[143] J. P. Perdew and Y. Wang, Physical Review B **45**, 13244 (1992).

[144] A. D. Becke, Physical Review A **38**, 3098 (1988).

[145] J. P. Perdew, K. Burke, and M. Ernzerhof, Physical Review Letters **77**, 3865 (1996).

[146] V. I. Anisimov, J. Zaanen, and O. K. Andersen, Physical Review B **44**, 943 (1991).

[147] J. Hubbard, Proceedings of the Royal Society of London A: Mathematical, Physical and Engineering Sciences **285**, 542 (1965).

[148] D. Baeriswyl, D. Campbell, J. Carmelo, F. Guinea, and E. Louis, *The Hubbard Model: Its Physics and Mathematical Physics*, *Nato Science Series B:* (Springer US, New York, 2013).

[149] V. I. Anisimov, F. Aryasetiawan, and A. I. Lichtenstein, Journal of Physics: Condensed Matter **9**, 767 (1997).

[150] J. P. Perdew, M. Ernzerhof, and K. Burke, The Journal of Chemical Physics **105**, 9982 (1996).

[151] M. Ernzerhof and G. E. Scuseria, The Journal of Chemical Physics **110**, 5029 (1999).

[152] J. Heyd, G. E. Scuseria, and M. Ernzerhof, The Journal of Chemical Physics **118**, 8207 (2003).

[153] J. Heyd, G. E. Scuseria, and M. Ernzerhof, The Journal of Chemical Physics **124**, 219906 (2006).

[154] N. Ashcroft and N. Mermin, *Solid State Physics*, *HRW international editions* (Holt, Rinehart and Winston, Boston, 1976).

[155] M. C. Payne, M. P. Teter, D. C. Allan, T. A. Arias, and J. D. Joannopoulos, Reviews of Modern Physics **64**, 1045 (1992).

[156] C. Rostgaard, The Projector Augmented-wave Method, 2009.

[157] P. E. Blöchl, Physical Review B **50**, 17953 (1994).

[158] H. Hellmann, *Einführung in die Quantumchemie* (Franz Deuticke, Leipzig, 1937).

[159] R. P. Feynman, Physical Review **56**, 340 (1939).

[160] O. H. Nielsen and R. M. Martin, Physical Review B **32**, 3780 (1985).

[161] D. Drabold and S. Estreicher, *Theory of Defects in Semiconductors*, *Oxford classic texts in the physical sciences* (Springer, Berlin-Heidelberg, 2007).

[162] A. Alkauskas, P. Deak, J. Neugebauer, A. Pasquarello, and C. Van de Walle, *Advanced Calculations for Defects in Materials: Electronic Structure Methods* (Wiley, Weinheim, 2011).

[163] A. Alkauskas, M. D. McCluskey, and C. G. V. de Walle, Journal of Applied Physics **119**, 181101 (2016).

[164] D. Rodney, L. Ventelon, E. Clouet, L. Pizzagalli, and F. Willaime, Acta Materialia **124**, 633 (2017).

[165] V. Bulatov and W. Cai, *Computer Simulations of Dislocations* (Oxford University Press, Oxford, 2006).

[166] S. Lany and A. Zunger, Modelling and Simulation in Materials Science and Engineering **17**, 084002 (2009).

[167] G. Makov, R. Shah, and M. C. Payne, Physical Review B **53**, 15513 (1996).

[168] M. J. Puska, S. Pöykkö, M. Pesola, and R. M. Nieminen, Physical Review B **58**, 1318 (1998).

[169] R. P. Messmer and G. D. Watkins, Physical Review Letters **25**, 656 (1970).

[170] G. A. Baraff and M. Schlüter, Physical Review B **19**, 4965 (1979).

[171] P. Deak, physica status solidi (b) **217**, 9 (2000).

[172] M. Stoneham, *Theories of Defects in Solids*, *Oxford Classic Texts in the Physical Sciences* (Oxford University Press, Oxford, 2001).

[173] S. B. Zhang and J. E. Northrup, Physical Review Letters **67**, 2339 (1991).

[174] S. E. Taylor and F. Bruneval, Physical Review B **84**, 075155 (2011).

[175] S. Lany and A. Zunger, Physical Review B **78**, 235104 (2008).

[176] H.-P. Komsa, T. T. Rantala, and A. Pasquarello, Physical Review B **86**, 045112 (2012).

[177] Y. Kumagai and F. Oba, Physical Review B **89**, 195205 (2014).

[178] G. Makov and M. C. Payne, Physical Review B **51**, 4014 (1995).

[179] C. Freysoldt, J. Neugebauer, and C. G. Van de Walle, Physical Review Letters **102**, 016402 (2009).

[180] C. Freysoldt, J. Neugebauer, and C. G. Van de Walle, physica status solidi (b) **248**, 1067 (2011).

[181] P. P. Ewald, Annalen der Physik **369**, 253 (1921).

[182] I. Dabo, B. Kozinsky, N. E. Singh-Miller, and N. Marzari, Physical Review B **77**, 115139 (2008).

[183] M. Lannoo and J. Bourgoin, *Point Defects in Semiconductors: Theoretical aspects*, *Springer Series in Solid-State Sciences* (Springer-Verlag, Berlin-Heidelberg, 1981).

[184] J. Bourgoin and M. Lannoo, *Point defects in semiconductors: Experimental aspects*, *Springer series in solid-state sciences* (Springer-Verlag, Berlin-Heidelberg, 1983).

[185] P. Rinke, A. Janotti, M. Scheffler, and C. G. Van de Walle, Physical Review Letters **102**, 026402 (2009).

[186] P. Rinke, A. Schleife, E. Kioupakis, A. Janotti, C. Rödl, F. Bechstedt, M. Scheffler, and C. G. Van de Walle, Physical Review Letters **108**, 126404 (2012).

[187] R. LeSar, *Introduction to Computational Materials Science: Fundamentals to Applications* (Cambridge University Press, Cambridge, 2013).

[188] E. Kröner, *Kontinuumstheorie der Versetzungen und Eigenspannungen*, *Ergebnisse der Angewandten Mathematik* (Springer, Berlin-Heidelberg, 1958).

[189] J. Hardy, Journal of Physics and Chemistry of Solids **29**, 2009 (1968).

[190] G. Leibfried and N. Breuer, *Point Defects in Metals I: Introduction to the Theory*, *Springer Tracts in Modern Physics* (PUBLISHER, Berlin-Heidelberg, 2006).

[191] M. J. Gillan, Philosophical Magazine A **48**, 903 (1983).

[192] A. M. Stoneham, Journal of Physics C: Solid State Physics **16**, L925 (1983).

[193] M. J. Gillan, Journal of Physics C: Solid State Physics **17**, 1473 (1984).

[194] M. P. Puls, Philosophical Magazine A **51**, 893 (1985).

[195] M. Leslie and N. J. Gillan, Journal of Physics C: Solid State Physics **18**, 973 (1985).

[196] D. A. Freedman, D. Roundy, and T. A. Arias, Physical Review B **80**, 064108 (2009).

[197] F. Bruneval and J.-P. Crocombette, Physical Review B **86**, 140103 (2012).

[198] A. Goyal, K. Mathew, R. G. Hennig, A. Chernatynskiy, C. R. Stank, S. T. Murphy, D. A. Andersson, S. R. Phillpot, and B. P. Uberuaga, The conundrum of relaxation volumes in first-principles calculations of charge defects, 2017.

[199] F. Bruneval, C. Varvenne, J.-P. Crocombette, and E. Clouet, Physical Review B **91**, 024107 (2015).

[200] W. Cai, V. V. Bulatob, J. Chang, J. Li, and S. Yip, Philosophical Magazine **83**, 539 (2003).

[201] D. Barragan-Yani and K. Albe, Physical Review B **95**, 115203 (2017).

[202] D. B. Holt and B. G. Yacobi, *Extended Defects in Semiconductors* (Cambridge University Press, Cambridge, 2007).

[203] R. Bader, *Atoms in Molecules: A Quantum Theory*, *International Ser. of Monogr. on Chem* (Clarendon Press, Oxford, 1994).

[204] C. Persson and S. Mirbt, Brazilian Journal of Physics **36**, 286 (2006).

[205] C. Persson, Y.-J. Zhao, S. Lany, and A. Zunger, Physical Review B **72**, 035211 (2005).

[206] S. Lany and A. Zunger, Physical Review B **72**, 035215 (2005).

[207] T. R. Paudel and W. R. L. Lambrecht, Physical Review B **77**, 205202 (2008).

[208] A. Janotti and C. G. Van de Walle, Physical Review B **76**, 165202 (2007).

[209] J. D. Gale, Journal of the Chemical Society, Faraday Transactions **93**, 629 (1997).

[210] J. D. Gale and A. L. Rohl, Molecular Simulation **29**, 291 (2003).

[211] J. Weertman and J. Weertman, *Elementary dislocation theory*, *Macmillan series in materials science* (Macmillan, London, 1964).

[212] H. Matare, *Defect Engineering in Semiconductors* (John Wiley & Sons Inc., New York, 1971).

[213] K. Takarabe, K. Kawai, K. Wakamura, S. Minomura, and N. Yamamoto, Journal of Crystal Growth **99**, 766 (1990).

[214] H. Neumann, physica status solidi (a) **96**, K121 (1986).

[215] T. Tinoco, A. Polian, D. Gómez, and J. P. Itié, physica status solidi (b) **198**, 433 (1996).

[216] H. W. Spiess, U. Haeberlen, G. Brandt, A. Räuber, and J. Schneider, physica status solidi (b) **62**, 183 (1974).

[217] A. Kraft, G. Kühn, and W. Möller, Zeitschrift für anorganische und allgemeine Chemie **504**, 155 (1983).

[218] A. Stukowski, Modelling and Simulation in Materials Science and Engineering **18**, 015012 (2010).

[219] K. Momma and F. Izumi, Journal of Applied Crystallography **44**, 1272 (2011).

[220] S. Nishiwaki, T. Satoh, S. Hayashi, Y. Hashimoto, T. Negami, and T. Wada, Journal of Materials Research **14**, 4514 (1999).

[221] H. Rodriguez-Alvarez, N. Barreau, C. Kaufmann, A. Weber, M. Klaus, T. Painchaud, H.-W. Schock, and R. Mainz, Acta Materialia **61**, 4347 (2013).

[222] L. A. Giannuzzi, J. L. Drown, S. R. Brown, R. B. Irwin, and F. A. Stevie, Microscopy Research and Technique **41**, 285 (1998).

[223] M. H. F. Overwijk, F. C. van den Heuvel, and C. W. T. Bulle-Lieuwma, Journal of Vacuum Science & Technology B: Microelectronics and Nanometer Structures Processing, Measurement, and Phenomena **11**, 2021 (1993).

[224] R. Egerton, *Electron Energy-Loss Spectroscopy in the Electron Microscope* (Springer US, New York, 2012).

[225] O. Krivanek, G. Corbin, N. Dellby, B. Elston, R. Keyse, M. Murfitt, C. Own, Z. Szilagyi, and J. Woodruff, Ultramicroscopy **108**, 179 (2008).

[226] H. Föll and B. O. Kolbesen, Applied Physics **8**, 319 (1975).

[227] M. H Ultramicroscopy **74**, 131 (1998).

[228] L. Lymperakis, J. Neugebauer, M. Albrecht, T. Remmele, and H. P. Strunk, Physical Review Letters **93**, 196401 (2004).

[229] S. M. Lee, M. A. Belkhir, X. Y. Zhu, Y. H. Lee, Y. G. Hwang, and T. Frauenheim, Physical Review B **61**, 16033 (2000).

[230] D. Barragan-Yani and K. Albe, Journal of Applied Physics **123**, 165705 (2018).

[231] A. Chirila *et al.*, Nature Materials **12**, 1107 EP (2013).

[232] Y. Sun, S. Lin, W. Li, S. Cheng, Y. Zhang, Y. Liu, and W. Liu, Engineering **3**, 452 (2017).

[233] L. E. Oikkonen, M. G. Ganchenkova, A. P. Seitsonen, and R. M. Nieminen, Journal of Applied Physics **114**, 083503 (2013).

[234] E. S. Mungan, X. Wang, and M. A. Alam, IEEE Journal of Photovoltaics **3**, 451 (2013).

[235] P.-P. Choi, O. Cojocaru-Mirédin, R. Wuerz, and D. Raabe, Journal of Applied Physics **110**, 124513 (2011).

[236] R. V. Forest, E. Eser, B. E. McCandless, J. G. Chen, and R. W. Birkmire, Journal of Applied Physics **117**, 115102 (2015).

[237] L. Kronik, D. Cahen, and H. W. Schock, Advanced Materials **10**, 31 (1998).

[238] O. Cojocaru-Mirédin, P. Choi, R. Wuerz, and D. Raabe, Ultramicroscopy **111**, 552 (2011), special Issue: 52nd International Field Emission Symposium.

[239] A. Laemmle, R. Wuerz, T. Schwarz, O. Cojocaru-Mirédin, P.-P. Choi, and M. Powalla, Journal of Applied Physics **115**, 154501 (2014).

[240] F. Couzinie-Devy, E. Cadel, N. Barreau, L. Arzel, and P. Pareige, Scripta Materialia **104**, 83 (2015).

[241] D. J. Schroeder and A. A. Rockett, Journal of Applied Physics **82**, 4982 (1997).

[242] X. Sun, F. Jiang, and J. Feng, Computational Materials Science **47**, 31 (2009).

[243] E. Ghorbani, J. Kiss, H. Mirhosseini, G. Roma, M. Schmidt, J. Windeln, T. D. KÃijhne, and C. Felser, The Journal of Physical Chemistry C **119**, 25197 (2015).

[244] S. Schuler, S. Siebentritt, S. Nishiwaki, N. Rega, J. Beckmann, S. Brehme, and M. C. Lux-Steiner, Physical Review B **69**, 045210 (2004).

[245] Z.-K. Yuan, S. Chen, Y. Xie, J.-S. Park, H. Xiang, X.-G. Gong, and S.-H. Wei, Advanced Energy Materials **6**, 1601191 (2016), 1601191.

[246] R. D. Shannon, Acta Crystallographica Section A **32**, 751 (1976).

[247] D. K. Ward, X. W. Zhou, B. M. Wong, F. P. Doty, and J. A. Zimmerman, Physical Review B **85**, 115206 (2012).

[248] X. W. Zhou, D. K. Ward, B. M. Wong, and F. P. Doty, Physical Review Letters **108**, 245503 (2012).

[249] J. J. Chavez, D. K. Ward, B. M. Wong, F. P. Doty, J. L. Cruz-Campa, G. N. Nielson, V. P. Gupta, D. Zubia, J. McClure, and X. W. Zhou, Physical Review B **85**, 245316 (2012).

[250] X. W. Zhou *et al.*, Physical Review B **85**, 245302 (2012).

[251] X. W. Zhou, D. K. Ward, F. P. Doty, J. A. Zimmerman, B. M. Wong, J. L. Cruz-Campa, G. N. Nielson, J. J. Chavez, D. Zubia, and J. C. McClure, Progress in Photovoltaics: Research and Applications **23**, 1837 (2015), pip.2628.

[252] M. Yu and S. D. Kenny, Journal of Physics: Condensed Matter **28**, 105002 (2016).

[253] K. E. Kweon, D. Åberg, and V. Lordi, Physical Review B **93**, 174109 (2016).

[254] S. V. Boriskina *et al.*, Journal of Optics **18**, 073004 (2016).

[255] A. Smets, K. Jäger, O. Isabella, R. van Swaaij, and M. Zeman, *Solar Energy: Fundamentals, Technology and Systems* (Delft University of Tecnology, Delft, 2014).

[256] F. H. Alharbi and S. Kais, Renewable and Sustainable Energy Reviews **43**, 1073 (2015).

[257] R. Broudy, Advances in Physics **12**, 135 (1963).

[258] T. Figielski, Solid-State Electronics **21**, 1403 (1978).

[259] A. Ourmazd, Contemporary Physics **25**, 251 (1984).

[260] D. C. Look and J. R. Sizelove, Physical Review Letters **82**, 1237 (1999).

[261] V. Lebedev, V. Cimalla, J. Pezoldt, M. Himmerlich, S. Krischok, J. A. Schaefer, O. Ambacher, F. M. Morales, J. G. Lozano, and D. González, Journal of Applied Physics **100**, 094902 (2006).

[262] V. Lebedev, V. Cimalla, T. Baumann, O. Ambacher, F. M. Morales, J. G. Lozano, and D. GonzÃąlez., Journal of Applied Physics **100**, 094903 (2006).

[263] B. Bansal, R. Ghosh, and V. Venkataraman, Journal of Applied Physics **113**, 163705 (2013).

[264] M. Reiche, M. Kittler, H. Uebensee, E. Pippel, A. Haehnel, and S. Birner, Applied Physics A **122**, 389 (2016).

[265] D. Jena, Physical Review B **70**, 245203 (2004).

[266] I. Sugiyama, N. Shibata, Z. Wang, S. Kobayashi, T. Yamamoto, and Y. Ikuhara, Nature Nanotechnology **8**, 266 (2013).

[267] J. S. White *et al.*, Physical Review Letters **111**, 037201 (2013).

[268] A. Finco, P.-J. Hsu, A. Kubetzka, K. von Bergmann, and R. Wiesendanger, Physical Review B **94**, 214402 (2016).

[269] G. Weingarten, Atti della Reale Accademia dei Lincei Serie 5 **10**, 57 (1901).

[270] V. Volterra, Annales scientifiques de l'École Normale Supérieure **24**, 401 (1907).

[271] A. E. H. Love, *A Treatise on the Mathematical Theory of Elasticity*, 4 ed. (Cambridge University Press, Cambridge, 1927).

[272] J. A. Ewing and W. Rosenhain, Proceedings of the Royal Society of London **65**, 85 (1899).

[273] G. I. Taylor, Proceedings of the Royal Society of London A: Mathematical, Physical and Engineering Sciences **145**, 362 (1934).

[274] G. I. Taylor, Proceedings of the Royal Society of London A: Mathematical, Physical and Engineering Sciences **145**, 388 (1934).

[275] M. Polanyi, Zeitschrift für Physik **89**, 660 (1934).

[276] E. Orowan, Zeitschrift für Physik **89**, 634 (1934).

[277] M. Volmer and W. Schultze, Zeitschrift für Physikalische Chemie **156A**, 1 (1931).

[278] M. Volmer, *Kinetik der phasenbildung*, *Die chemische reaktion* (J. W. Edwards, Ann Arbor, Michigan, 1939).

[279] F. C. Frank, Discussions of the Faraday Society **5**, 48 (1949).

[280] P. B. Hirsch, R. W. Horne, and M. J. Whelan, Philosophical Magazine **86**, 4553 (2006).

[281] M. Kittler and M. Reiche, Advanced Engineering Materials **11**, 249 (2009).

[282] M. Reiche, M. Kittler, H. Uebensee, E. Pippel, and S. Hopfe, Advances in nano research **2**, 1 (2014).

[283] K. K. Adepalli, M. Kelsch, R. Merkle, and J. Maier, Advanced Functional Materials **23**, 1798 (2013).

[284] K. K. Adepalli, M. Kelsch, R. Merkle, and J. Maier, Physical Chemistry Chemical Physics **16**, 4942 (2014).

[285] K. K. Adepalli, J. Yang, J. Maier, H. L. Tuller, and B. Yildiz, Advanced Functional Materials **27**, 1700243 (2017), 1700243.

[286] Progress in Materials Science **54**, 770 (2009).

[287] R. Ishikawa, Y. Shimbo, I. Sugiyama, N. R. Lugg, N. Shibata, and Y. Ikuhara, Physical Review B **96**, 024440 (2017).